Wefer, G., Berger, W.H., Richter, C., et al., 1998
Proceedings of the Ocean Drilling Program, Initial Reports, Vol. 175

13. SITE 1085[1]

Shipboard Scientific Party[2]

HOLE 1085A

Position: 29°22.4665′S, 13°59.4064′E

Start hole: 1215 hr, 26 September 1997

End hole: 1815 hr, 29 September 1997

Time on hole: 78.00 hr

Seafloor (drill pipe measurement from rig floor, mbrf): 1724.8

Total depth (drill pipe measurement from rig floor, mbrf): 2328.8

Distance between rig floor and sea level (m): 11.6

Water depth (drill pipe measurement from sea level, m): 1713.2

Penetration (mbsf): 604

Coring totals:
Type: APC
Number: 33
Cored: 305.00 m
Recovered: 293.28 m (96.16%)

Type: XCB
Number: 31
Cored: 299.00 m
Recovered: 301.11 m (100.71%)

Lithology:
Unit I: Subunit IA: nannofossil-foraminifer ooze
Subunit IB: nannofossil ooze
Unit II: clay-rich nannofossil ooze (Core 175-1085A-64X)

HOLE 1085B

Position: 29°22.4657′S, 13°59.3898′E

Start hole: 1815 hr, 29 September 1997

End hole: 2330 hr, 30 September 1997

Time on hole: 29.25 hr

Seafloor (drill pipe measurement from rig floor, mbrf): 1724.6

Total depth (drill pipe measurement from rig floor, mbrf): 2045.8

Distance between rig floor and sea level (m): 11.6

Water depth (drill pipe measurement from sea level, m): 1713.0

Penetration (mbsf): 321.2

Coring totals:
Type: APC
Number: 35
Cored: 321.20 m
Recovered: 326.51 m (101.65%)

Lithology:
Subunit IA: nannofossil-foraminifer ooze
Subunit IB: nannofossil ooze

Principal results: One of the main objectives for drilling at Site 1085 was to help document the path and strength of the Benguela Current system from the Miocene to the Quaternary, as well as the shoreward and seaward migrations of the upwelling center. The upwelling inside the Benguela Coastal Current is fed from the thermocline by South Atlantic Central Water, and its intensity is related to the position and intensity of the Benguela Current system. Filaments of cold, nutrient-rich waters from the coastal upwelling area extend as much as 600 km offshore. Here, cold water mixes with low-productivity oceanic water, forming a zone of intermediate productivity. Site 1085 is located off the side of the Orange River mouth, which has water year-round and delivers additional terrigenous sediments. This effect should be more pronounced during times when the Benguela Current and coastal upwelling were of lower intensity than today, so that sediments from ocean production were less dominant. A close tie-in between pelagic and terrigenous sedimentation is expected to be present within the slope record.

Two holes were cored with the advanced hydraulic piston corer/extended core barrel (APC/XCB) at Site 1085 to a maximum depth of 605.0 meters below seafloor (mbsf), which recovered a relatively continuous hemipelagic sedimentary section spanning the Holocene to middle Mio-cene (0–15 Ma). Hole 1085A was cored with the APC to 305 mbsf and was extended with the XCB to a depth of 605 mbsf. Hole 1085A was logged with a full suite of sensors (seismostratigraphic suite, lithoporosity suite, Formation MicroScanner [FMS] suite, and the geological high-sensitivity magnetic tool [GHMT]) from 601 to 60 mbsf. At Hole 1085B, 35 cores were taken with the APC to 321 mbsf.

Sediments form two lithostratigraphic units dominated by nannofossil ooze. The uppermost unit has been subdivided into two subunits to reflect the decrease in foraminiferal abundances downhole. The underlying unit is a reddish brown, microfaulted, and thinly laminated clay-rich nannofossil ooze. Graded, 2- to 17-cm-thick beds rich in foraminifer tests are present between 30 and 70 mbsf. Below 360 mbsf, pyrite is present as isolated fine sand-sized grains and, below 420 mbsf, as nodules as much as 1 cm in diameter. The deepest core of Hole 1085A is interpreted as a slump block. It consists of a thinly laminated reddish to olive-brown nannofossil ooze. Packages of occasionally graded laminae within this unit are commonly microfaulted, convolutely layered, and folded. The detrital component in sediments from Site 1085 is dominated by clay and trace abundances of silt-sized, subangular mono- and polycrystalline quartz grains. Sedimentation rates range from 15 to 80 m/m.y., with the highest values located within the last 8 m.y.

Physical sediment properties were determined both by high-resolution multisensor track (MST) core logging and index properties measurements. Detailed comparisons between the magnetic susceptibility generated on the MST and color reflectance measured with the Minolta spectrophotometer demonstrated complete recovery of the sedimentary sequence down to 289 meters composite depth (mcd).

A biostratigraphic framework composed of both calcareous nannofossils and foraminifers was established, resulting in a well-constrained age model for Site 1085. Calcareous nannofossils are abundant and well preserved throughout the entire section. Reworking was limited only to the interval between 60 and 100 mbsf. The overall abundance of benthic for-

[1]Wefer, G., Berger, W.H., Richter, C., et al., 1998. *Proc. ODP, Init. Repts.,* 175: College Station, TX (Ocean Drilling Program).

[2]Shipboard Scientific Party is given in the list preceding the Table of Contents.

aminifers was high throughout the studied interval. The planktonic to benthic foraminifer ratio at this site is about ten times higher than at previous sites. Radiolarians are generally rare and show signs of dissolution in almost all samples. Radiolarian assemblages indicate that intermittent upwellings occurred through the last ~3 m.y. The presence of an Antarctic species indicates an occasional influence of cooler waters. Diatoms are rare or absent in most of the section. The interval between 89.17 and 127.45 mbsf (upper Pliocene, 1.8–2.6 Ma) contains a mixed/*Thalassiothrix antarctica*–rich diatom assemblage similar to the one found in upper Pliocene sediments from Site 1084. Dinoflagellate cysts are common in the upper Miocene sediment (6– 10 Ma).

A complete magnetostratigraphy was determined at Site 1085 after alternating-field (AF) demagnetization at 20 mT. All chrons from the Brunhes (C1n) to the earliest part of the Gilbert (~5.5 Ma) were identified, although the quality of the record was not good because of a severe magnetic overprint.

Sediments from Site 1085 contain small amounts of marine organic matter, with total organic carbon (TOC) concentrations fluctuating between 2.8 wt% and nil. Concentrations of calcium carbonate are generally between 85 and 60 wt%, but drop to 35 wt% in sediments deposited during the Miocene carbonate crisis. Interstitial water chemistry is controlled dominantly by the low organic carbon and high carbonate concentrations in the sediment, which result in modest variations in the chemical gradients of many dissolved species. Alkalinity rises to a broad maximum of ~30 mM between 46 and 84 mbsf and subsequently decreases to the bottom of the hole. The deepest alkalinity value of 1.752 mM is by far the lowest (except for near-surface data) observed so far during Leg 175 and most likely reflects consumption via clay mineral formation. Sulfate is not completely consumed until 65 mbsf, which is also deep compared with previous Leg 175 sites. Carbonate and phosphate precipitation reactions throughout the sequence also are inferred from the profiles of dissolved calcium, magnesium, and phosphate.

Hole 1085A was logged with a full suite of sensors to continuously characterize the sedimentary changes through depth and to provide data for core-log integration. The recorded data are affected by poor hole conditions. Enlargements and washout zones were identified in the entire logged interval. Despite the adverse hole conditions, resistivity, sonic velocity, natural gamma-ray, and magnetic susceptibility provide reliable data and show well-expressed changes related to the various proportions of biogenic, clastic, and organic components.

Drilling at Site 1085 recovered a continuous high-resolution record with sedimentation rates of ~50 m/m.y. The carbonate-rich sediments will allow the reconstruction of the position and intensity of the Benguela Current for the last 15 m.y., including the influence of water masses coming from the Indian Ocean and the Subantarctic Region.

BACKGROUND AND OBJECTIVES

Site 1085, in connection with other sites, especially Sites 1082 and 1084, helps document the path and strength of the Benguela Current system from the Miocene to the Quaternary, as well as the shoreward and seaward migrations of the upwelling center. The upwelling inside the Benguela Coastal Current is fed from the thermocline by South Atlantic Central Water, and its intensity is related to the position and intensity of the Benguela Current system. Filaments of cold, nutrient-rich waters from the coastal upwelling area extend well offshore (as much as ~600 km offshore; Lutjeharms and Stockton, 1987; see Fig. 1, “Site 1084” chapter, this volume). Here, the cold water mixes with low-productivity oceanic water and forms a zone of intermediate productivity.

Coastal upwelling within the Benguela Current system varies with the seasonal extremes of summer and winter (Shannon and Nelson, 1996). The seasonal pattern is used to divide the system into a northern Benguela Region (NBR) and a southern Benguela Region (SBR; Dingle, 1995). This is seen in the modern-day planktonic foraminiferal distributions (Giraudeau, 1993) and has been demonstrated using benthic ostracods (Dingle, 1995) and satellite imaging (Lutjeharms and Meeuwis, 1987). The boundary between the NBR and SBR (Lüderitz Boundary) is the site of maximum upwelling intensity at 26°–27°S, which has the coldest and the most persistent upwelling.

Upwelling in the area north of the Lüderitz Boundary (e.g., at the location of Site 1084) is typified by year-round high productivity and enhanced accumulation of phytoplankton (Brown et al., 1991). Wind speeds are of medium intensity, with a wide oceanic mixing domain characterized by filaments (Lutjeharms and Stockton, 1987). The SBR has a highly seasonal upwelling regime, with its maximum in summer, and a restricted mixing domain (Lutjeharms and Meeuwis, 1987; Giraudeau and Rogers, 1994). Sites 1085, 1086, and 1087 are located within the SBR.

Site 1085 is located off the side of the mouth of the Orange River, which discharges into the South Atlantic throughout the year, delivering additional terrigenous sediments. This effect should be more pronounced during times when the Benguela Current and coastal upwelling were of lower intensity than today, so that sediments from ocean production were less dominant. A close tie-in between pelagic and terrigenous sedimentation is expected to be present within the slope record. Clay mineralogical results from Deep Sea Drilling Project Site 362 give indications for a precursor to the modern Benguela Current in the middle Miocene (14 Ma), which was too weak to produce upwelling but reached the Walvis Ridge during glacial periods and transported montmorillonite northward from the Orange River. In interglacial periods of the middle Miocene, the local source of illite (the Namib Desert) overwhelmed the distant montmorillonite supply (Diester-Haass et al., 1990). The more southern Site 1085 will provide an excellent comparison to Site 362, as it is closer to the clay mineral source area. From these older sediments, we expect a picture of the conditions of circulation before strong coastal upwelling arose.

Compared with Site 1084, which is much closer to the centers of upwelling (especially the one strong cell off Lüderitz), we should find relatively low sedimentation rates. A rate of ~5 cm/k.y. was determined (Schulz et. al., 1992) for an 11-m-long core collected from near the same water depth (Geosciences Bremen [GeoB] 1719-7, 28°55.6′S, 14°10.7′E, water depth 1010m) but ~45 km to the north. Because of the proximity of the Agulhas Retroflection (Lutjeharms, 1996) and the Subtropical Convergence Zone, we expect to find indications of warm-water incursions in the fauna and flora of the plankton embedded into assemblages typical for temperate and cool conditions. Also, for this offshore site, we expect a stronger open-ocean influence on sedimentation compared with the more northern sites, with their strong coastal upwelling imprints.

OPERATIONS

Hole 1085A (Proposed Site MCB-A)

The 237-nmi voyage to Site 1085 was accomplished at an average speed of 10.1 kt. The speed of the vessel was adversely affected because of the northward flowing Benguela Current and rough seas. The vessel approached the Global Positioning System coordinates of the site, and a beacon was deployed at 1215 hr on 26 September. Hole 1085A was spudded with the APC at 1653 hr. The seafloor depth was estimated from the recovery of the first core at 1713.2 meters below sea level (mbsl). APC coring advanced without incident to 305.0 mbsf (Cores 175-1085A-1H through 33H), which was considered refusal depth for piston coring, with 96.2% recovery (Table 1; also see expanded core summary table on CD-ROM, back pocket, this vol-

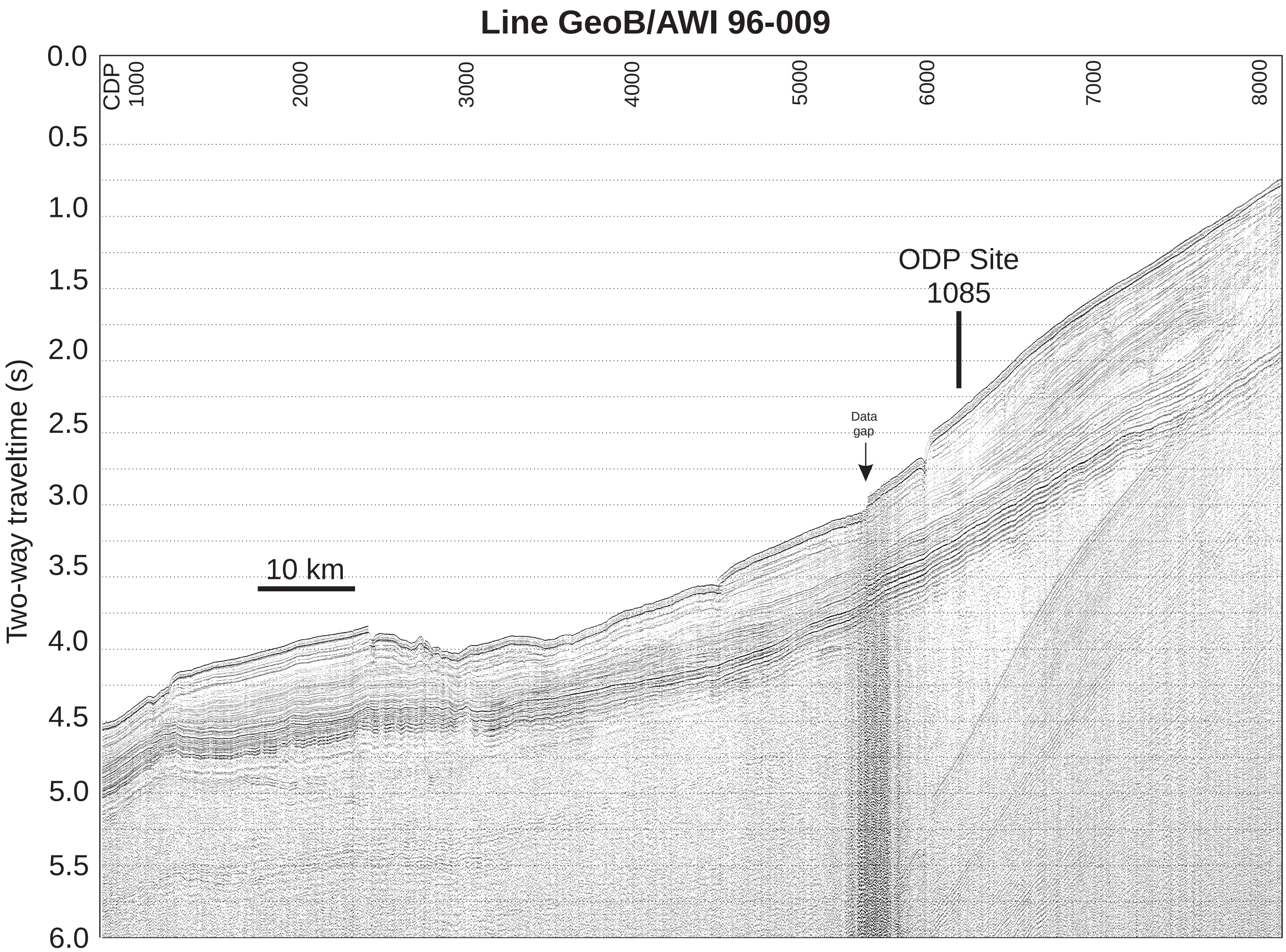

Figure 1. Seismic Line GeoB/AWI 96-009 with Site 1085. Vertical axis is given in TWT. CDP interval is 25 m for a shotpoint spacing of 25 m. Seismic data is 24-fold stacked and not migrated. Site 1085 is located at CDP 6163.

ume). Cores were oriented starting with Core 4H. Adara heat-flow measurements were taken at 41.7 mbsf (5H), 60.7 mbsf (7H), 79.7 mbsf (11H), and 231.7 mbsf (25H). XCB coring advanced to 605.0 mbsf (64X), with 100.7% recovery.

Logging Operations in Hole 1085A

In preparation for logging, an aluminum go-devil was dropped to ensure the opening of the lockable float valve. After the hole was flushed with a high-viscosity mud treatment, the bit was placed at the logging depth of 88.3 mbsf. Hole 1085A was logged with a full suite of sensors. For each run, the pipe was set at 88.3 mbsf and pulled back to 60.0 mbsf during logging. The wireline logging heave compensator was started when the logging tools reached the mudline.

Logging operations began at 0030 hr on 29 September. The first log was conducted with the seismostratigraphic suite (25.8 m long). This suite was made up of the spectral gamma-ray (NGT), long-spacing sonic (LSS), phasor dual-induction (DIT), and Lamont-Doherty high-resolution temperature (TLT) sondes. This tool string was deployed in the pipe at 0110 hr and logged the hole up from 603.2 mbsf. The tool string was recovered at 0510 hr. The second log was with the lithoporosity suite (19.5 m long) and included the hostile environment gamma spectrometry (HNGS), accelerator porosity (APS), lithodensity (LDS), and TLT sondes. The tool string was deployed at 0620 hr, logged the hole up from 600.7 mbsf, and was retrieved at 1020 hr. The third log was made with the FMS suite (12.10 m long) and included the NGT, general purpose inclinometer, and FMS sondes. This tool string was deployed at 1125 hr and logged the hole up from 600.7 mbsf. The tool string was recovered by 1400 hr. The fourth and last log was made with the magnetic susceptibility suite (11.8 m long) and included the NGT, magnetic susceptibility, and nuclear resonance magnetometer sondes. The tool was deployed in the pipe at 1425 hr and logged the hole up from 600.7 mbsf. It was retrieved at 1715 hr on 29 September. The logging equipment was rigged down by 1800 hr. The drill string was then pulled out of the hole with the bit clearing the seafloor at 1815 hr on 29 September, thereby ending operations at Hole 1085A.

Hole 1085B

The vessel was offset 30 m to the west, and Hole 1085B was spudded with the APC at 1915 hr. The recovery of the first core established the seafloor depth at 1713.0 mbsl. APC coring advanced without incident to refusal at 321.2 mbsf (Cores 175-1085A-1H through

Table 1. Coring summary for Site 1085.

Core	Date (Sept 1997)	Time (UTC)	Interval (mbsf)	Length cored (m)	Length recovered (m)	Recovery (%)
175-1085A-						
1H	26	1705	0.0-3.7	3.7	3.67	99.2
2H	26	1745	3.7-13.2	9.5	9.97	104.9
3H	26	1815	13.2-22.7	9.5	10.04	105.7
4H	26	1855	22.7-32.2	9.5	8.91	93.8
5H	26	1945	32.2-41.7	9.5	10.02	105.5
6H	26	2020	41.7-51.2	9.5	7.31	76.9
7H	26	2105	51.2-60.7	9.5	9.88	104.0
8H	26	2145	60.7-70.2	9.5	7.72	81.3
9H	26	2235	70.2-79.7	9.5	9.97	104.9
10H	26	2310	79.7-89.2	9.5	10.02	105.5
11H	26	2345	89.2-98.7	9.5	9.54	100.4
12H	27	0015	98.7-108.2	9.5	9.81	103.3
13H	27	0045	108.2-117.7	9.5	9.67	101.8
14H	27	0120	117.7-127.2	9.5	9.80	103.2
15H	27	0155	127.2-136.7	9.5	9.90	104.2
16H	27	0240	136.7-146.2	9.5	6.96	73.3
17H	27	0315	146.2-155.7	9.5	10.28	108.2
18H	27	0350	155.7-165.2	9.5	9.99	105.2
19H	27	0430	165.2-174.7	9.5	10.14	106.7
20H	27	0500	174.7-184.2	9.5	9.31	98.0
21H	27	0535	184.2-193.7	9.5	9.48	99.8
22H	27	0610	193.7-203.2	9.5	9.94	104.6
23H	27	0640	203.2-212.7	9.5	10.07	106.0
24H	27	0715	212.7-222.2	9.5	9.18	96.6
25H	27	0810	222.2-231.7	9.5	8.94	94.1
26H	27	0845	231.7-241.2	9.5	9.64	101.5
27H	27	0920	241.2-250.7	9.5	9.72	102.3
28H	27	1000	250.7-260.2	9.5	8.74	92.0
29H	27	1035	260.2-269.7	9.5	9.51	100.1
30H	27	1105	269.7-279.2	9.5	0.01	0.1
31H	27	1140	279.2-288.7	9.5	9.77	102.8
32H	27	1220	288.7-298.2	9.5	8.57	90.2
33H	27	1255	298.2-305.0	6.8	6.80	100.0
34X	27	1400	305.0-314.7	9.7	9.69	99.9
35X	27	1440	314.7-324.4	9.7	9.92	102.3
36X	27	1520	324.4-334.0	9.6	9.55	99.5
37X	27	1555	334.0-343.7	9.7	9.91	102.2
38X	27	1630	343.7-353.4	9.7	9.92	102.3
39X	27	1710	353.4-363.0	9.6	9.92	103.3
40X	27	1745	363.0-372.7	9.7	9.66	99.6
41X	27	1815	372.7-382.4	9.7	9.87	101.8
42X	27	1855	382.4-392.1	9.7	9.85	101.5
43X	27	1930	392.1-401.8	9.7	9.99	103.0
44X	27	2010	401.8-411.5	9.7	9.49	97.8
45X	27	2050	411.5-421.1	9.6	8.94	93.1
46X	27	2130	421.1-430.7	9.6	9.57	99.7
47X	27	2210	430.7-440.4	9.7	9.91	102.2
48X	27	2245	440.4-450.0	9.6	9.90	103.1
49X	27	2330	450.0-459.7	9.7	9.86	101.6
50X	28	0030	459.7-468.9	9.2	7.55	82.1
51X	28	0155	468.9-478.5	9.6	9.92	103.3
52X	28	0325	478.5-488.2	9.7	9.82	101.2
53X	28	0505	488.2-497.9	9.7	9.82	101.2
54X	28	0630	497.9-507.6	9.7	9.19	94.7
55X	28	0740	507.6-517.2	9.6	9.88	102.9
56X	28	0900	517.2-526.9	9.7	9.63	99.3
57X	28	1010	526.9-536.6	9.7	9.92	102.3
58X	28	1115	536.6-546.2	9.6	9.86	102.7
59X	28	1245	546.2-555.8	9.6	9.92	103.3
60X	28	1425	555.8-565.5	9.7	9.90	102.1
61X	28	1610	565.5-575.1	9.6	9.94	103.5
62X	28	1810	575.1-584.7	9.6	9.92	103.3
63X	28	1940	584.7-594.4	9.7	9.95	102.6
64X	28	2110	594.4-604.0	9.6	9.94	103.5
Coring totals:				604.0	594.39	98.4
175-1085B-						
1H	29	1925	0.0-7.9	7.9	7.90	100.0
2H	29	2000	7.9-17.4	9.5	9.74	102.5
3H	29	2035	17.4-26.9	9.5	9.66	101.7
4H	29	2110	26.9-36.4	9.5	9.94	104.6
5H	29	2140	36.4-45.9	9.5	9.88	104.0
6H	29	2215	45.9-55.4	9.5	9.95	104.7
7H	29	2250	55.4-64.9	9.5	9.92	104.4
8H	29	2320	64.9-74.4	9.5	8.89	93.6
9H	29	2355	74.4-83.9	9.5	10.05	105.8
10H	30	0025	83.9-93.4	9.5	9.87	103.9
11H	30	0100	93.4-102.9	9.5	9.37	98.6
12H	30	0130	102.9-112.4	9.5	9.98	105.1
13H	30	0205	112.4-121.9	9.5	9.87	103.9
14H	30	0235	121.9-131.4	9.5	10.09	106.2
15H	30	0310	131.4-140.9	9.5	9.76	102.7
16H	30	0345	140.9-150.4	9.5	8.82	92.8
17H	30	0415	150.4-159.9	9.5	9.97	104.9
18H	30	0450	159.9-169.4	9.5	9.47	99.7
19H	30	0525	169.4-178.9	9.5	9.27	97.6
20H	30	0600	178.9-188.4	9.5	9.25	97.4
21H	30	0635	188.4-197.9	9.5	9.73	102.4
22H	30	0705	197.9-207.4	9.5	9.75	102.6
23H	30	0740	207.4-216.9	9.5	9.97	104.9
24H	30	0815	216.9-226.4	9.5	9.51	100.1
25H	30	0845	226.4-235.9	9.5	9.99	105.2
26H	30	0920	235.9-245.4	9.5	9.63	101.4
27H	30	0955	245.4-254.9	9.5	9.82	103.4
28H	30	1025	254.9-260.9	6.0	6.18	103.0
29H	30	1055	260.9-270.4	9.5	10.09	106.2
30H	30	1130	270.4-279.9	9.5	9.58	100.8
31H	30	1240	279.9-289.4	9.5	8.08	85.1
32H	30	1325	289.4-298.9	9.5	9.85	103.7
33H	30	1420	298.9-308.4	9.5	9.80	103.2
34H	30	1500	308.4-315.4	7.0	7.00	100.0
35H	30	1540	315.4-321.2	5.8	5.88	101.4
Coring totals:				321.2	326.51	101.7

Notes: UTC = Universal Time Coordinated. An expanded version of this coring summary table that includes lengths and depths of sections and comments on sampling is included on CD-ROM (back pocket, this volume).

35H), with 101.7% recovery (Table 1). The last two cores did not achieve full piston strokes because of the indurated sediment. Cores were oriented starting with Core 3H. The drill string was retrieved, with the bit clearing the seafloor at 1730 hr. After the beacon, hydrophones, and thrusters were retracted and the drilling equipment was secured, the vessel was under way to the next site at 2330 hr on 30 September.

SITE GEOPHYSICS

Introduction and Strategy

The Mid-Cape Basin study area at 29°S was chosen between the main working areas of the Southern Cape Basin (SCB) at 31°S and the Northern Cape Basin at 25°S on the northern side of the Orange Fan. This area originally was not included in the drilling proposal. In the structural map of Dingle et al. (1987), the area appeared at the southern rim of a slump area. From the survey, it was expected (1) to find a less disturbed upper sedimentary sequence than in the SCB and (2) to collect data between 25° and 31°S to study the temporal and spatial evolution of upwelling systems along the coast by north–south correlation and comparison of seismostratigraphic units. The location was also chosen based on previous Parasound surveys during *Meteor* Cruises M20/2 and M23/1, *Polarstern* Cruise ANT XI/5 and *Sonne* Cruise SO 86, where surface sediments appeared to be mostly undisturbed.

A small survey (Fig. 1) was carried out during *Meteor* Cruise M34/1 (Bleil et al., 1996), which provided an additional location for drilling (MCB-A) near the crossing point between seismic Lines GeoB/AWI 96-009 and 96-011. This location was added to the proposal and received approval for drilling.

Three seismic Lines GeoB/AWI 96-009 to 96-011 with a total length of 350 km were shot (Fig. 2). Both the Hydrosweep swath sounder survey (Bleil et al., 1996) and seismic data from Line GeoB/

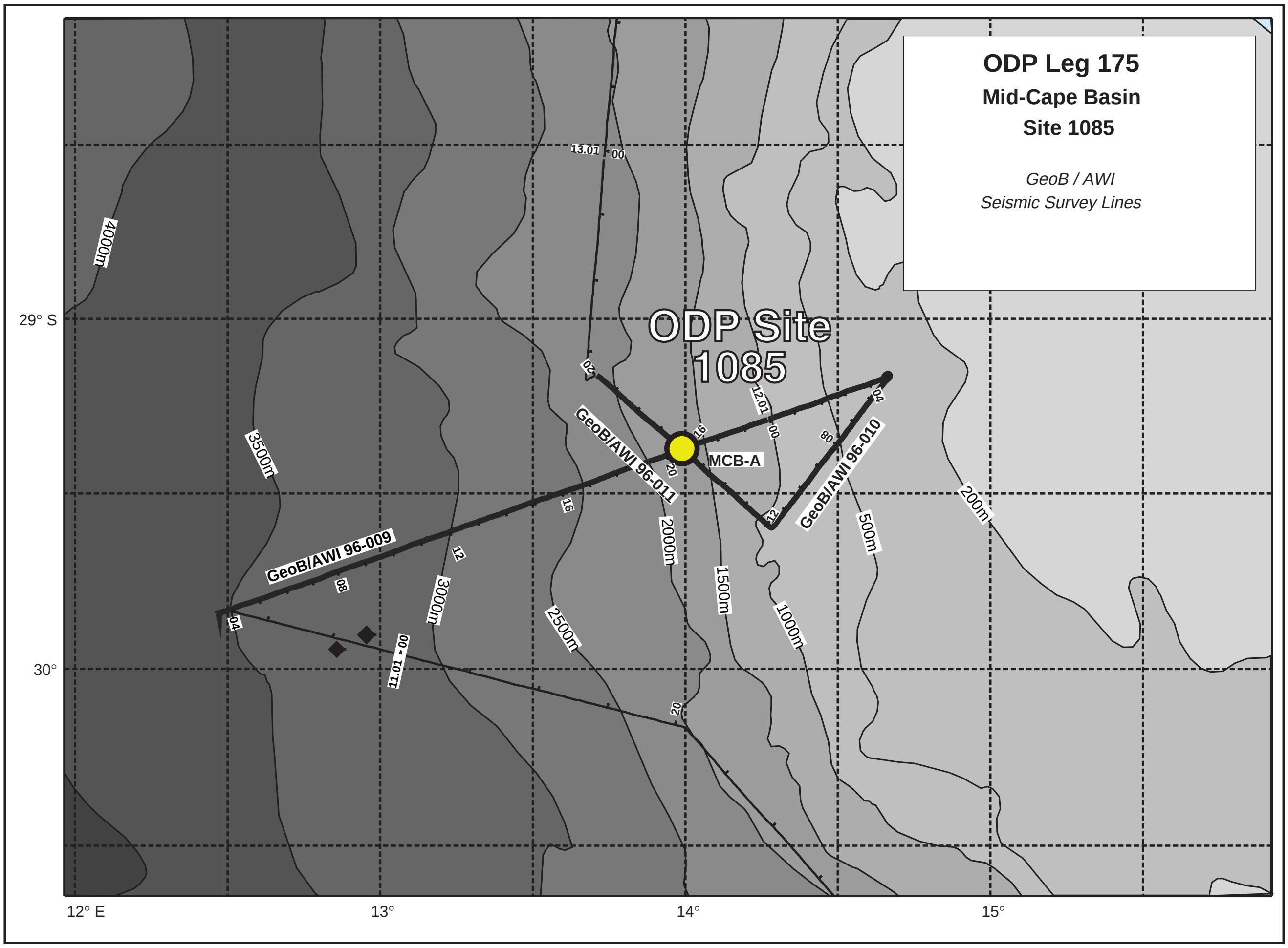

Figure 2. Map of seismic presite survey lines, proposed site locations, and ODP Leg 175 drill Site 1085 in the Mid-Cape Basin. Bathymetry was derived from Gebco Digital Dataset on CD-ROM.

AWI 96-009 (Fig. 1) document several scarps (common depth points [CDPs] 1100, 2300, 4400, and 5800) probably related to slump events where major portions of the surface sediment (as much as 100 m) were removed. The sedimentary sequences seem to be intact only on the upper slope above 2000 m water depth. Data quality was partially affected by bad weather conditions, but the integrity of the sediment column within the drilling range of 600 m could generally be confirmed. These observations are in agreement with the structural information published by Dingle et al. (1987).

Seismostratigraphy

Site 1085 is located in 1713 m water depth on seismic Line GeoB/AWI 96-009 (CDP 6163; Fig. 1). Deposition appears to be pelagic or hemipelagic with only minor lateral and depth variations in layer thickness. In general, the seismic character near the site is similar to the SCB working area, although several differences exist. A prominent feature is a band of high-amplitude reflectors between 800 and 1000 ms sub-bottom two-way traveltime (TWT). In the SCB area (see “Site Geophysics” section, “Site 1086” chapter, this volume) it marks the base of seismic Unit 2, where we assign it to the well-known Reflector D (L) of Cretaceous–Paleocene age (Emery et al., 1975; Bolli, Ryan et al., 1978). The thickness of the sediment package of 1000 ms TWT above Reflector D is slightly higher than the 850 ms TWT in the SCB area, which may be attributed to the absence of hiatuses caused by listric faults. Internal fracturing by small faults is also absent, and lateral variations in reflection strength are minor.

Site 1085

Figure 3 shows a 10-km-long seismic section of Line GeoB/AWI 96-009 across Site 1085. Low seismic amplitudes within the upper 450 ms TWT (seismic Unit 1) indicate a homogenous lithology. Stronger reflectors paralleling the seafloor are probably caused by ghost signals of a deep-lying streamer. Drilling also penetrates the upper part of seismic Unit 2, which is characterized by some higher amplitude reflectors. A gradual increase of seismic energy is observed between 450 and 550 ms TWT. An intercalated unit of 10- to 20-m thickness at 580 ms TWT sub-bottom depth, probably of slump origin, thins out downslope and is associated with a stronger reflector. The unit beneath appears mostly transparent. At its base at 700 ms TWT, reflection amplitudes generally increase.

Figure 4 shows a close-up of the seismic section, plotted against TWT, for a 1-km-long interval near the drill site. Seismic reflectors are compared with the resistivity log (see “Downhole Logging” section, this chapter), which was plotted against the TWT derived from

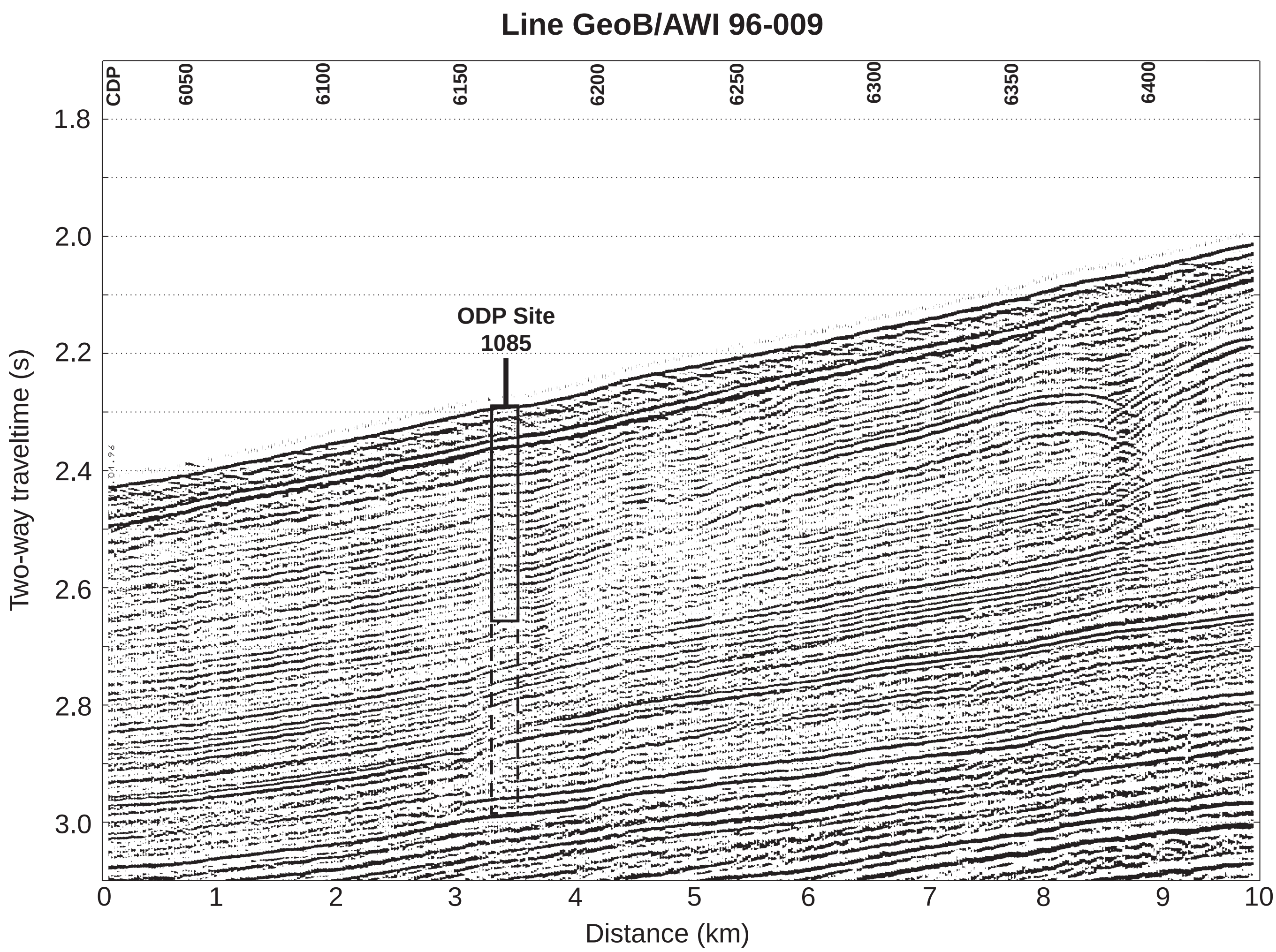

Figure 3. Seismic section of Line GeoB/AWI 96-009 at Site 1085. Vertical axis is given in TWT. CDP interval is 25 m for a shotpoint spacing of 25 m. Site 1085 is located at CDP 6163. The box indicates the approximate penetration of the borehole of 300 m (APC) and 600 m (XCB), respectively.

the sound velocity log. The logging data confirm the homogeneity of the section down to 450 ms TWT. Few changes indicate gradually varying lithology, which may not be sharp enough to be imaged with the seismic data. The increase in seismic energy is associated with a higher scatter in the resistivity log, which appears even more pronounced in the sound velocity log (see "Downhole Logging" section, this chapter). Some selected reflectors can be tentatively attributed to major changes in the resistivity log, but a unique assignment will only be possible based on the calculation of synthetic seismograms. The base of Site 1085 shows a distinct increase in resistivity and density, which marks the top of an interval of stronger reflection amplitudes and probably of more lithified sediments with pronounced changes in physical properties (e.g., carbonate content).

LITHOSTRATIGRAPHY

Description of Lithostratigraphic Units

In contrast to previously drilled sites, sediments from Site 1085 have significantly lower gas concentrations (see "Organic Geochemistry" section, this chapter). As a consequence, the cores show only minor gas expansion cracks, and core disturbance, such as flow-in structures, is rare. Material cored with the extended core barrel below Core 175-1085A-34X at Hole 1085A consists mainly of drilling biscuits ranging in thickness between 2 and 4 cm. Sediments from Site 1085 form two lithostratigraphic units dominated by nannofossil ooze (Fig. 5). Unit I has been subdivided into Subunits IA and IB to reflect the decrease in foraminiferal abundances with depth. Subunit IA extends from Core 175-1085A-1H through 10H at both holes, and Subunit IB is characterized by nannofossil ooze and extends from Cores 175-1085A-11H through 63X. Unit II is a reddish brown, microfaulted and thinly laminated clay-rich nannofossil ooze. Unit II was encountered only in Core 175-1085A-64X.

Unit I

Intervals: 175-1085A-1H through 175-1085A-63X; 175-1085B-1H-bottom
Age: Holocene to middle Miocene
Depth: 1085A: 0–594.4 mbsf; 1085B: 0–321 mbsf

Subunit IA

Intervals: 175-1085A-1H through 175-1085A-10H; 175-1085B-1H through 175-1085B-10H
Age: Holocene to Late Pliocene
Depth: 1085A:0–98 mbsf; 1085B:0–83.9 mbsf

Subunit IA extends from the top of the hole to Core 10H at Holes 1085A and 1085B and is composed of moderately bioturbated,

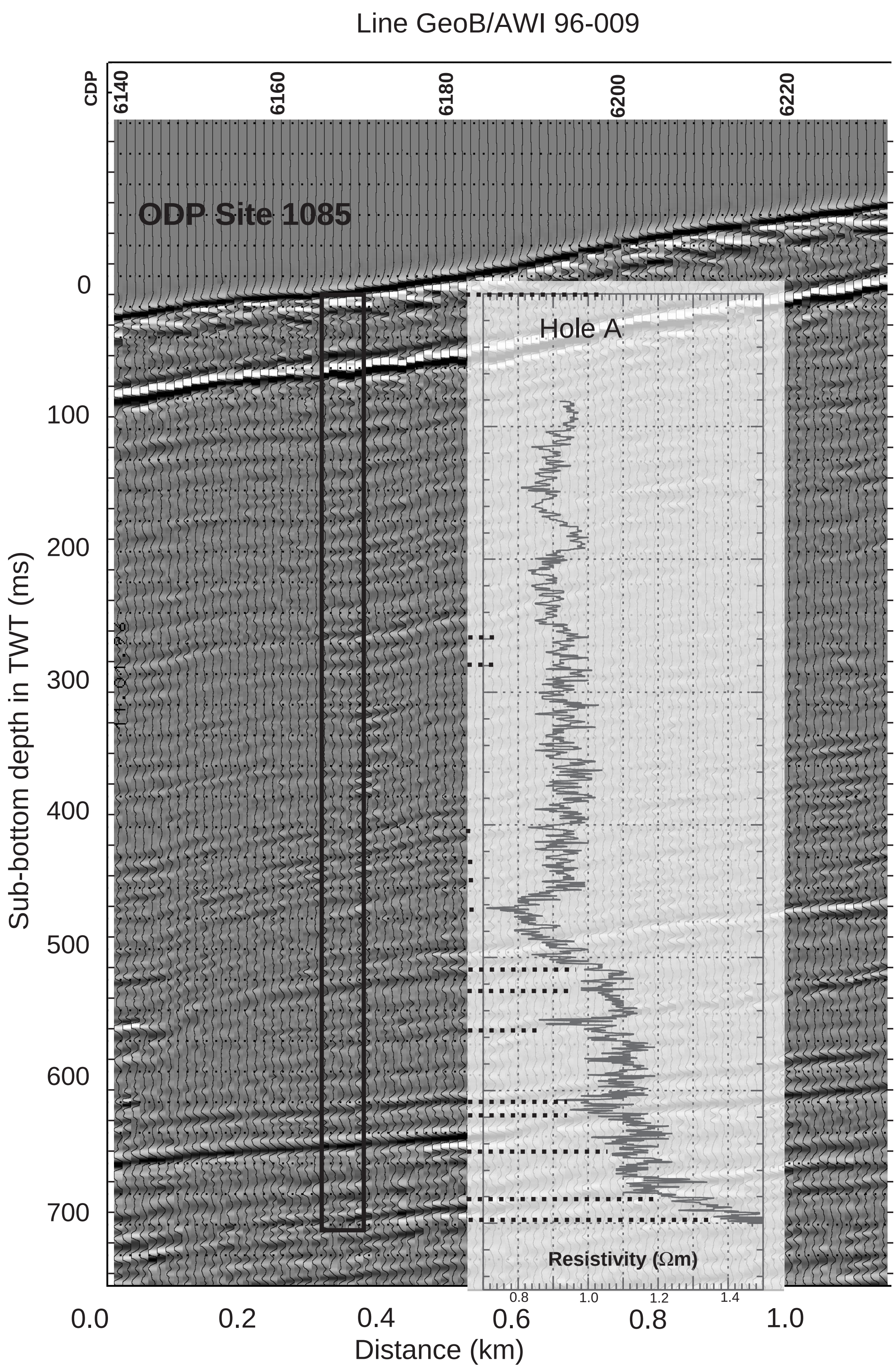

Figure 4. Close-up of Line GeoB/AWI 96-009 near Site 1085. Vertical axis is given in TWT. Amplitudes are grayscaled. For comparison, the resistivity log from downhole logging is shown. Logging depth is transferred to TWT using the logging results. Selected reflectors can be correlated with local extremes in the resistivity log (straight thick dashed lines).

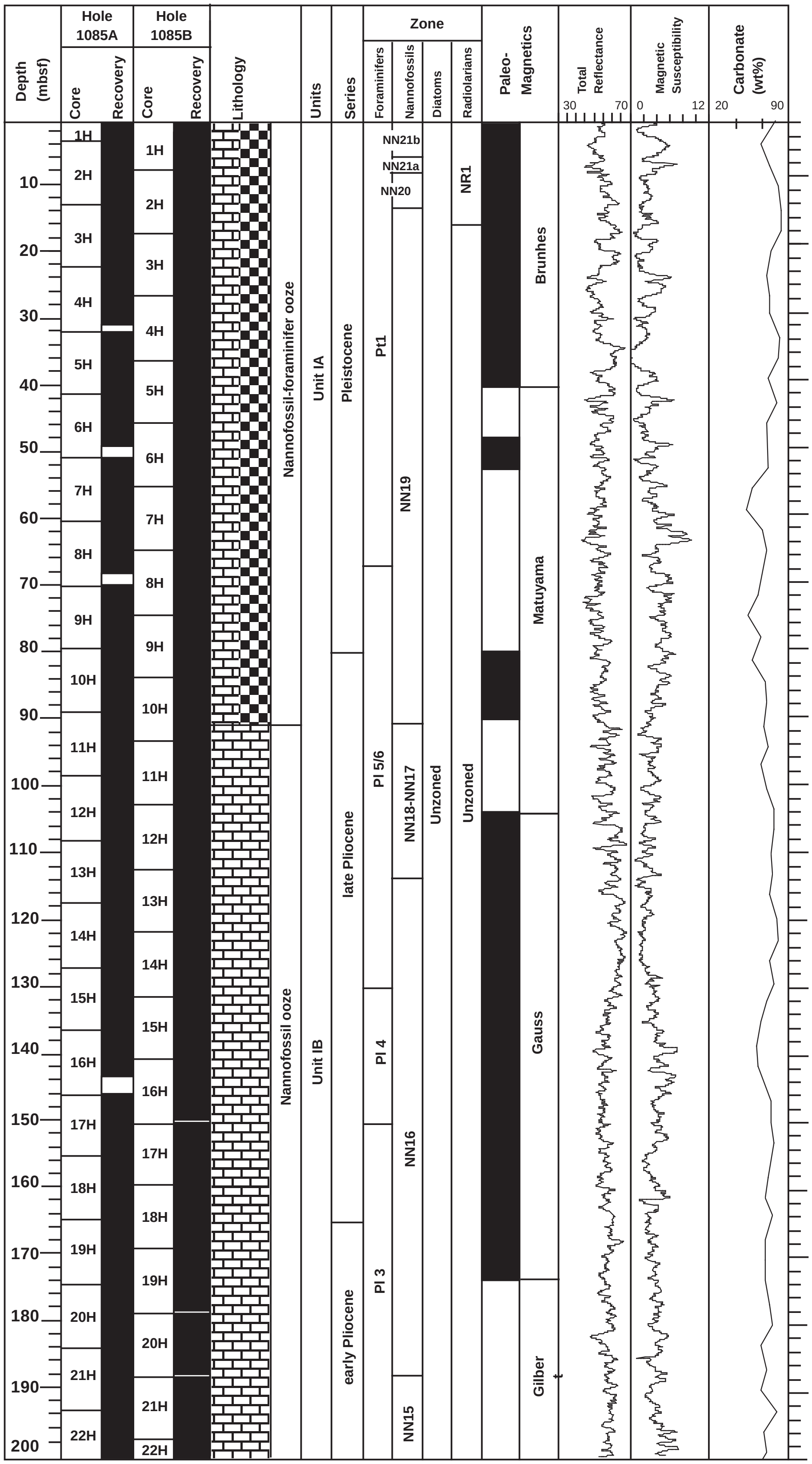

Figure 5. Composite stratigraphic section for Site 1085 showing core recovery in all holes, a simplified summary of lithology, age, total reflectance (400–700 nm), magnetic susceptibility, and calcium carbonate content. (Continued next page).

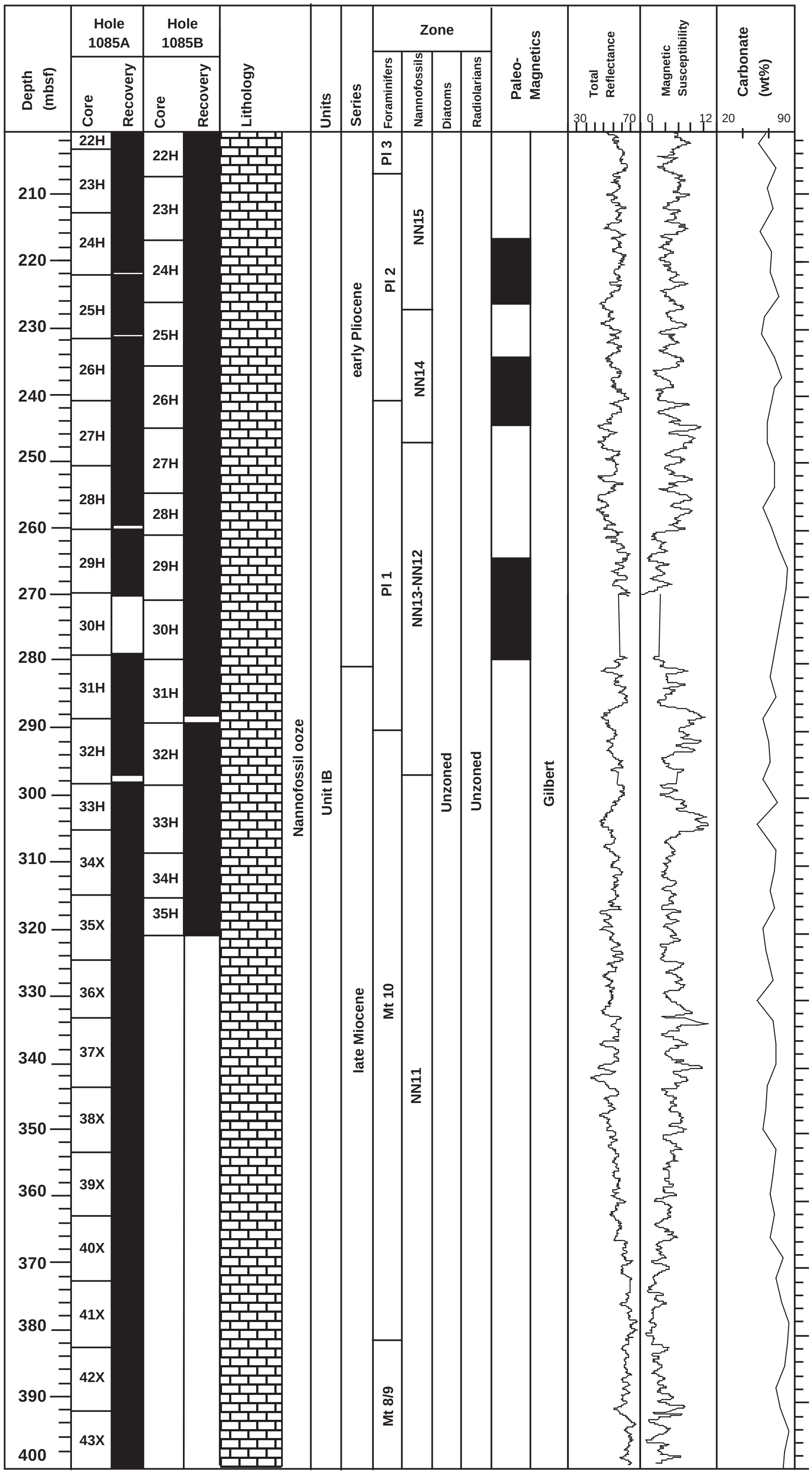

Figure 5 (continued).

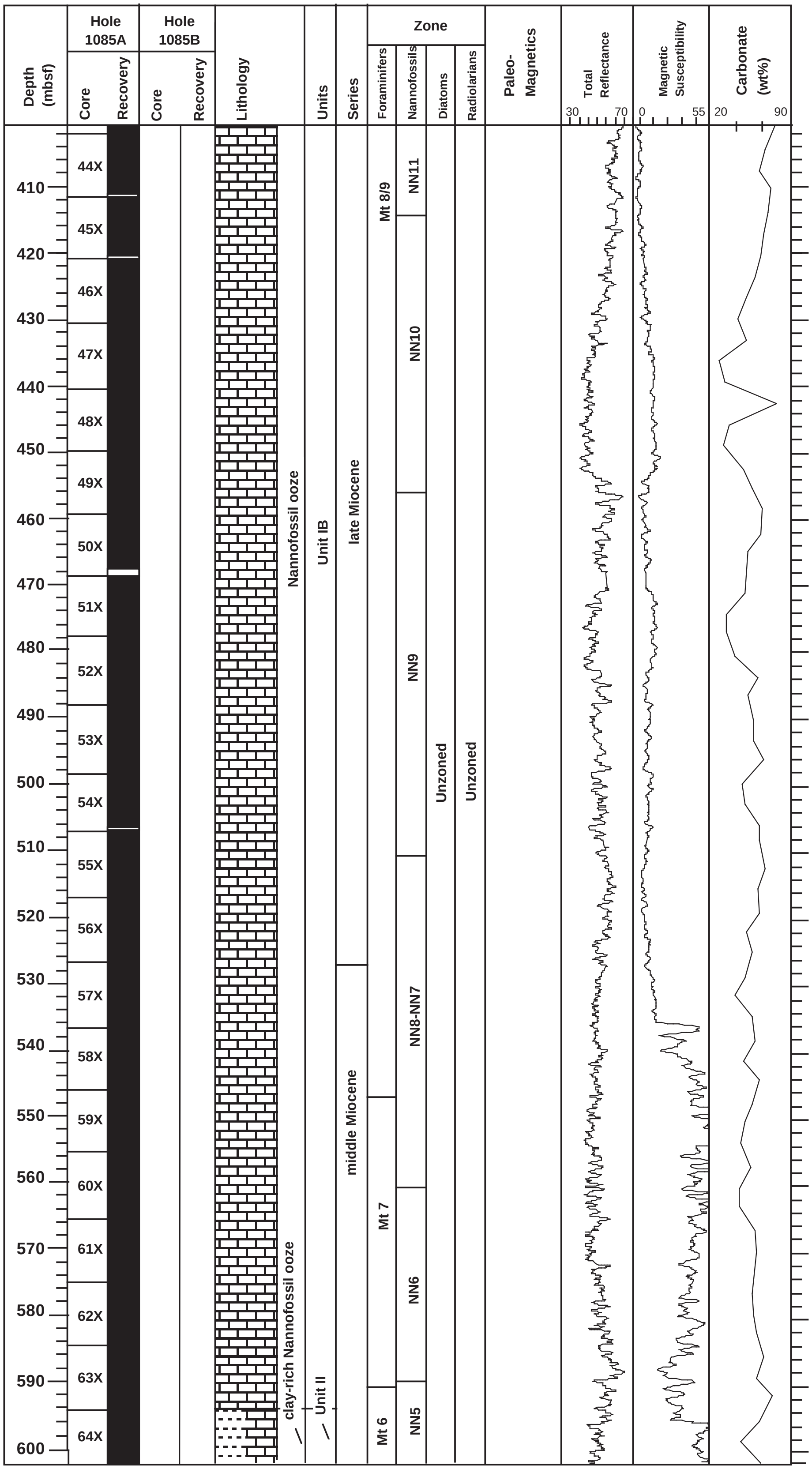

Figure 5 (continued).

greenish gray (10Y 7/2, 10Y 6/2), light greenish gray (5Y 7/2), pale olive (5Y 6/3), and dark greenish gray (10Y 5/2) nannofossil-foraminifer ooze. Individual color intervals range in thickness from 80 to 200 cm and grade into one another over 15 to 20 cm. Burrows are present throughout this subunit and vary in diameter between 0.5 and 2 cm. The infill has generally higher abundance of pyrite. Graded, 2- to 17-cm-thick beds rich in foraminifer tests are present within Cores 175-1085A-4H, 6H, and 8H. The thickest beds have sharp, erosive bases. Bivalve shells and a subrounded pebble of pumice are present within the lower 7 cm of a 17-cm-thick bed in interval 175-1085A-4H-2, 10–27 cm. A general characteristic of Subunit IA is the presence of gray mottles 1–3 mm in diameter. These mottles contain abundant finely disseminated pyrite. Subunit IA is characterized by high concentrations of calcium carbonate, which average 69 wt%.

Subunit IB

Intervals: 175-1085A-11H through 175-1085A-63X; 175-1085B-11H through 175-1085B-35H
Age: late Pliocene to middle Miocene
Depth: 1085A: 89.2–594.4 mbsf; 1085B: 83.9–321.2 mbsf

The dominant lithology of Subunit IB is greenish gray (10Y 7/2 and 10Y 6/2), light greenish gray (5Y 7/2), light gray (10Y 7/1), and pale olive (5Y 6/3) nannofossil ooze. Light greenish gray (10Y 6/2) diatom- and foraminifer-rich and dark greenish gray (10Y 5/2) diatom-bearing nannofossil foraminifer ooze are present in intervals between Cores 10H and 12H at Holes 1085A and 1085B. The appearance of diatoms is coincident with a gradual decrease in foraminiferal abundances. Below Core 175-1085A-23H, sediments either contain only trace or rare abundances of foraminifers, except for few short intervals where foraminifers are frequent. All cores have distinct burrows, which vary in diameter between 2 mm and 1 cm (Fig. 6). Zoophycos traces are common in Core 175-1085A-59X (Fig. 7). Gray and light olive-brown mottles, possibly burrows, contain abundant pyrite and are present throughout most of the cores. Below Core 175-1085A-40X, pyrite is in the form of isolated silt- to fine sand-sized grains. Starting with Core 175-1085A-46X, pyrite is present as nodules as much as 1 cm in diameter. A thinly laminated interval of clay-rich nannofossil ooze occurs between Sections 175-1085A-61X-4 and 61X-6. The contact between Subunit IB and Unit II is sharp and occurs in Core 175-1085A-63X. The nannofossil ooze at the base of Subunit IB is angularly discordant with and overlies the thinly laminated sediment of Unit II. Calcium carbonate contents in Subunit IB average 65 wt% and are slightly lower than those of Subunit IA.

Unit II

Interval: 175-1085A-64X-1 through 175-1085-64X-CC
Age: middle Miocene
Depth: 1085A: 594.4–604 mbsf

The deepest core of Hole 1085A is defined as Unit II, which consists of thinly laminated light gray (5Y 7/1) nannofossil ooze and gray (5Y 5/1) clay-rich nannofossil ooze. The sediments are reddish to olive brown. Laminae have sharp bases, are occasionally graded, and range in thickness from 1 to 5 mm. Packages of laminae within this unit are commonly microfaulted (Fig. 8), convolutely layered, and folded (Fig. 9). This unit is interpreted as a slump block. In Unit II, concentrations of calcium carbonate average 59 wt%, reflecting the slightly more clay-rich nature of these sediments.

Synthesis of Smear-Slide Analyses

The detrital component in sediments from Site 1085 is dominated by clay and trace abundances of silt-sized, subangular mono- and polycrystalline quartz grains. Authigenic minerals are rare or present in trace abundances. Pyrite is present as silt-sized euhedral aggregates or as framboids. The biogenic component in all smear slides consists of abundant to very abundant nannofossils. Foraminifers are abundant in Subunit IA and then decrease gradually from abundant to rare between Cores 175-1085A-11H and 27H. Diatoms are common only in Core 175-1085A-10H and are frequent to rare in Core 175-1085A-11H and 12H. Siliceous spicules are rare between 8.2 and 41 mbsf and between 127 and 142 mbsf at both Holes 1085A and 1085B. Reddish brown, subangular, silt-sized grains with high relief are present in trace amounts in 20-cm-thick intervals in Cores 175-1085A-58X through 64X. These grains may be titanite or rutile. Intervals are spaced 40 to 50 cm apart.

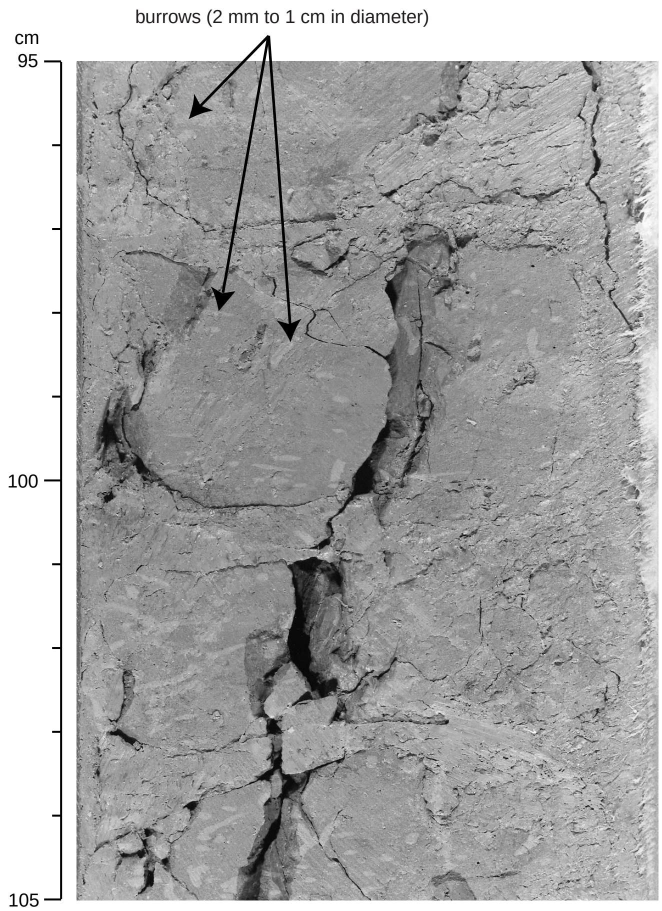

Figure 6. Bioturbated nannofossil ooze in interval 175-1085A-47X-5, 95–105 cm.

Spectrophotometry

Color reflectance data were measured every 2 cm down to Core 175-1085-8H for Hole 1085A, every 4 cm to the bottom of Hole 1085A, and for the entire Hole 1085B. The total reflectance ranges between 40% and 68% (Figs. 10, 11). The high calcium carbonate contents at this site (see “Organic Geochemistry” section, this chapter) suggest that the downcore fluctuations in the total reflectance are controlled primarily by the calcium carbonate content of the sediments. The ratio of the red (650 nm) to blue (450 nm) wavelengths varies between 1 and 2 and shows a gradual decrease for the upper 400 mbsf (Fig. 11). Superimposed on this long-term trend, the red/blue ratio values exhibit high-amplitude variations between 0 and 400 mbsf and low-amplitude variations between 400 and 600 mbsf. These low-amplitude variations are inversely correlated to magnetic susceptibility (Fig. 11). The total reflectance displays well-defined

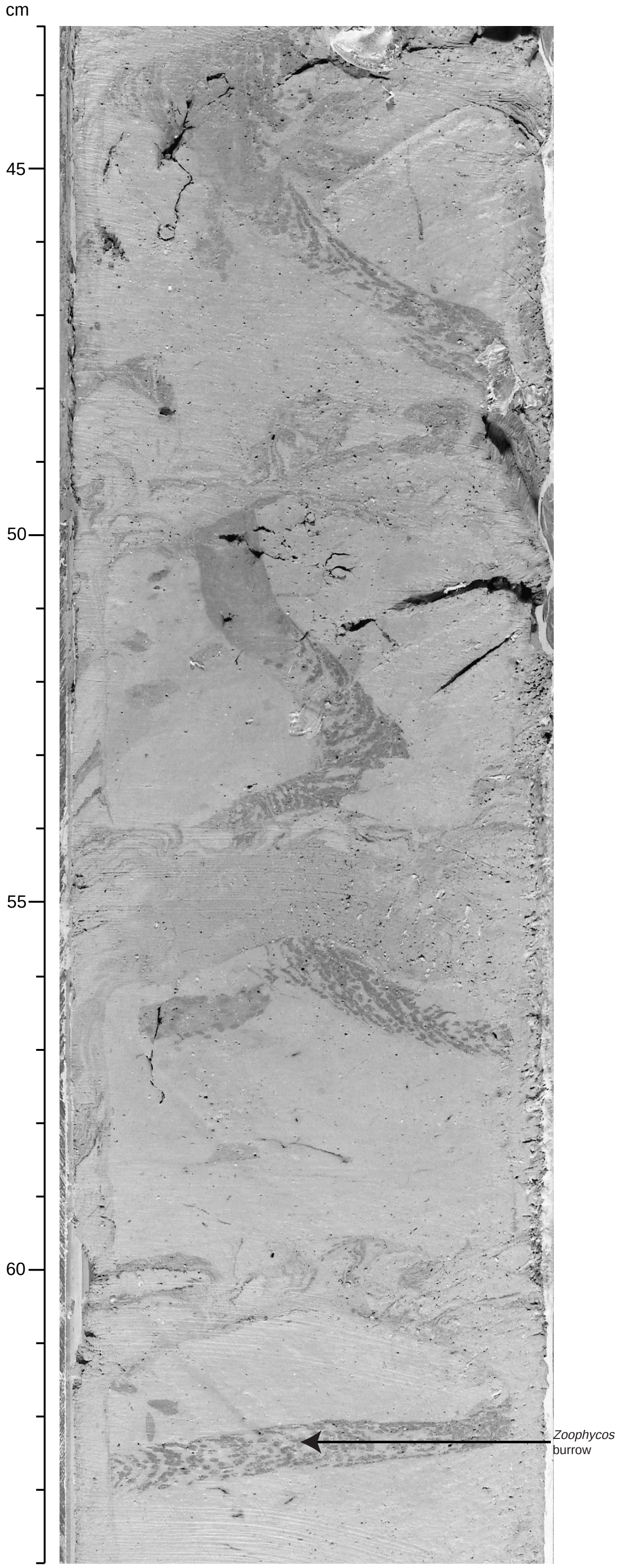

Figure 7. *Zoophycos* burrows in nannofossil ooze of interval 175-1085A-59X-2, 43–64 cm.

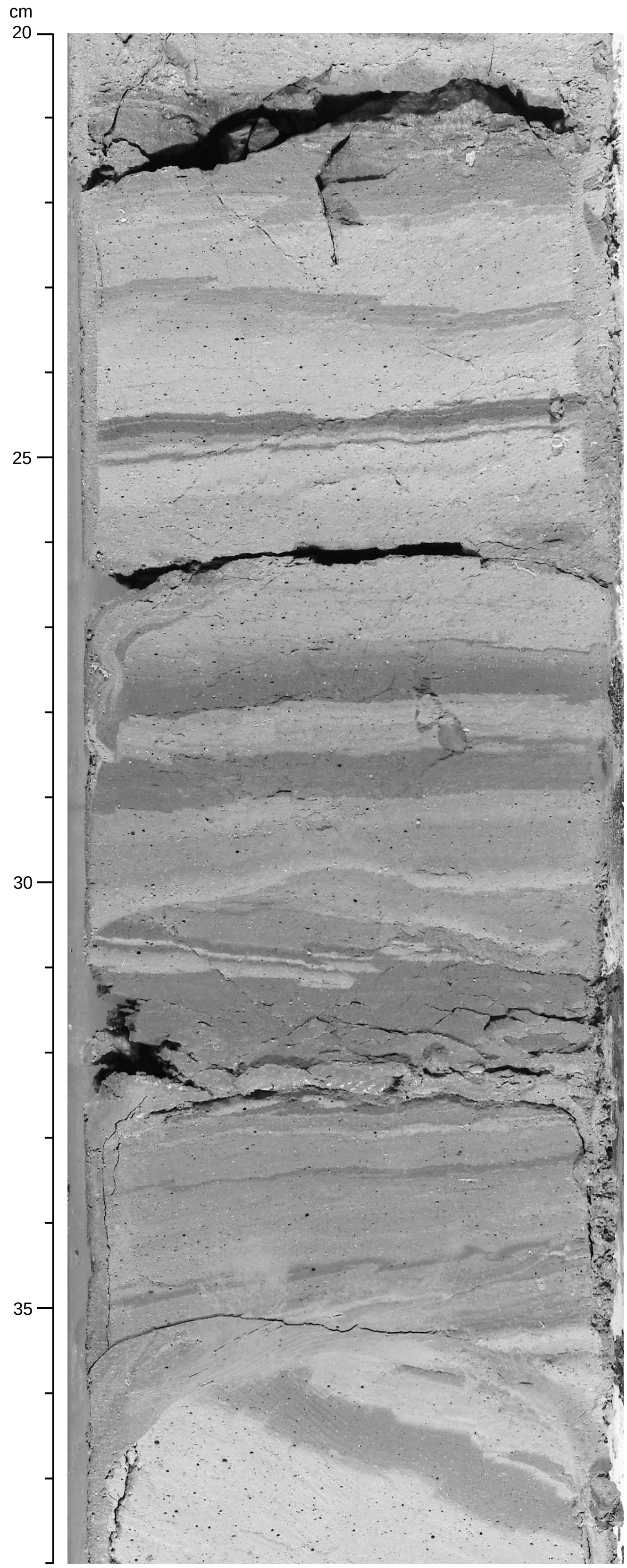

Figure 8. Microfaulting of reddish brown, clay-rich nannofossil ooze in the core catcher of Core 175-1085A-63X.

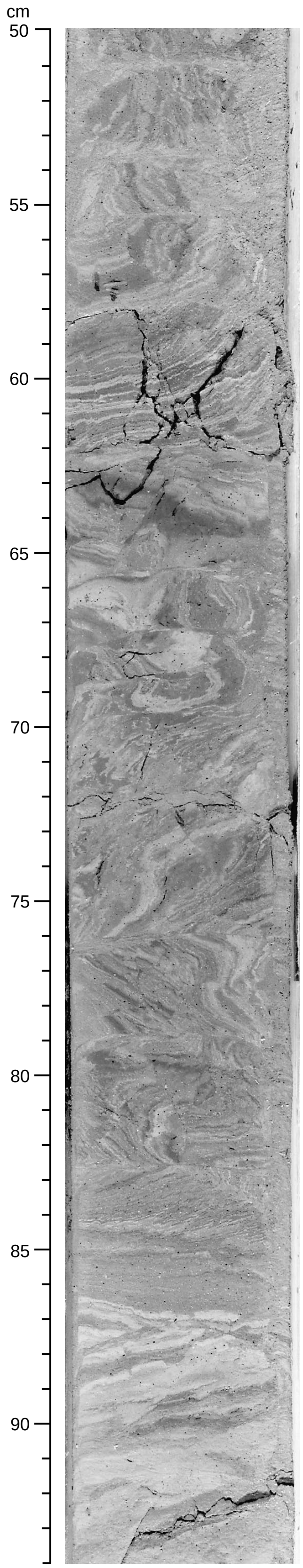

Figure 9. Convoluted bedding reddish brown, clay-rich nannofossil ooze in interval 175-1085A-64X-4, 50–94 cm, at Hole 1085A.

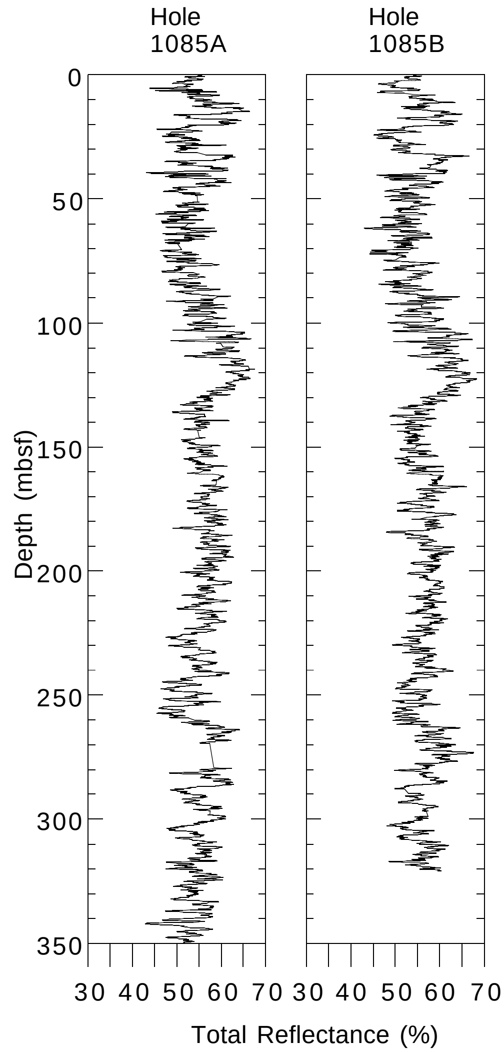

Figure 10. Downcore variations in the total reflectance at Holes 1085A and 1085B for the upper 350 mbsf.

and pronounced peaks in the upper 50 mbsf of Holes 1085A and 1085B. High-amplitude variations in total reflectance are observed for the entire drilled sedimentary succession (Fig. 11). Three pronounced events are recognized: high total reflectance values between 100 and 130 mbsf and between 350 and 430 mbsf, corresponding to high calcium carbonate concentrations ~75 and 80 wt% respectively, and low total reflectance values between 430 and 460 mbsf that are 50% lower in carbonate calcium contents than in the overlying sediments. The first event occurs between 2.7 and 3 Ma (see "Biostratigraphy and Sedimentation Rates" section, this chapter) and could be correlated to similar events observed at Sites 1082 and 1084. The second and third events occur between 6.5 and 9.7 Ma (see "Biostratigraphy and Sedimentation Rates" section, this chapter). Dissolution events indicated by higher relative percentages in the planktonic foraminifer fragments have been described in upper Miocene sediments for Site 360 off Cape Agulhas (Melguen, 1978). The minimum in total reflectance values occurs at 9.5 Ma, where carbonate percentages drop to relatively low values.

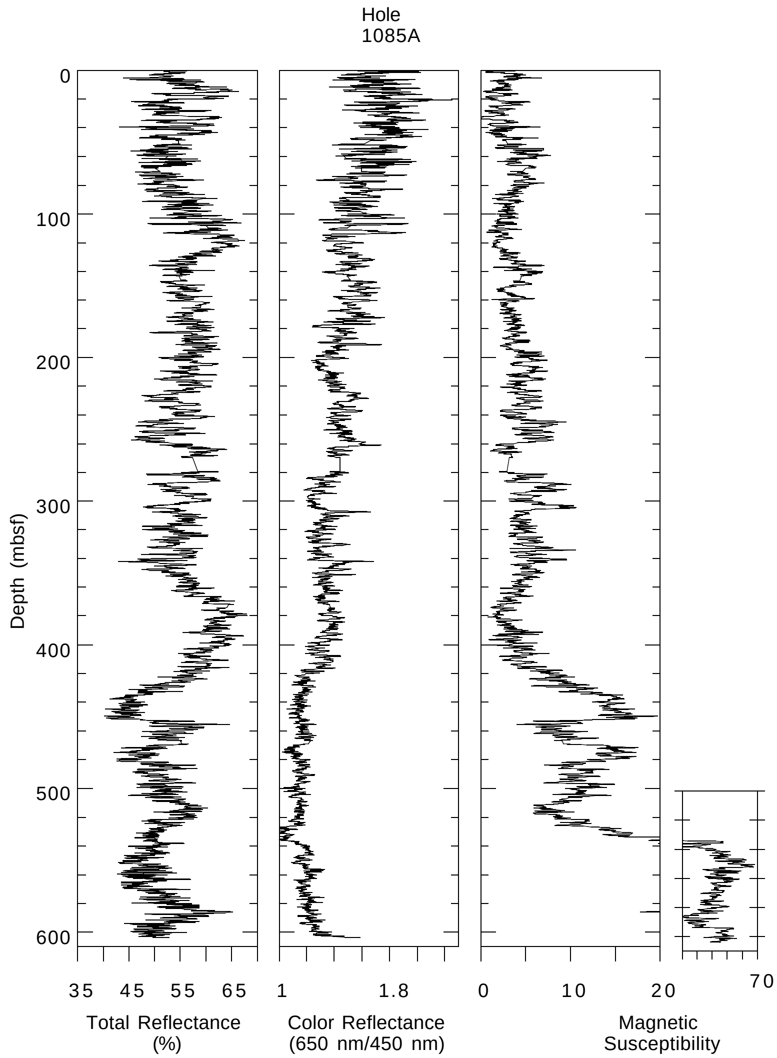

Figure 11. Downcore variations in the total reflectance, color reflectance (650 nm/450 nm), and magnetic susceptibility at Hole 1085A.

BIOSTRATIGRAPHY AND SEDIMENTATION RATES

A continuous hemipelagic sedimentary section reaching the middle Miocene (15 Ma) was recovered from Site 1085. The micropaleontological studies were carried out on core-catcher samples from Hole 1085A. Additional samples from within the cores were examined to improve the biostratigraphic resolution. A high-resolution biostratigraphy was developed using calcareous nannofossils and planktonic foraminifers. Sedimentation rates range from 1.5 to 13 cm/k.y. The lowest sedimentation rates are within the middle Miocene (1.5 cm/k.y.) and the highest are within the Pleistocene (13 cm/k.y.). Two other intervals with high sedimentation rates occur within the early part of the late Pliocene (7 cm/k.y.) and across the Miocene/Pliocene boundary (8 cm/k.y.).

Calcareous Nannofossils

Calcareous nannofossils were studied in core-catcher samples from Hole 1085A. Additional samples from within the top 11 cores (~top 100 mbsf) were examined close to datum events to improve the stratigraphic resolution. Nannofossils are abundant and well preserved throughout the entire section. Reworking (trace; early Pliocene specimen) was limited only to Cores 175-1085A-8H through 11H.

Based on the oldest identified datum, Site 1085 terminated within Zone NN5 (middle Miocene). Of the 25 identified biohorizons, 16 are zonal boundary markers (Table 2). Within the sampling resolution, the sedimentation appears continuous throughout the entire section (Fig. 12). The nannofossil-derived biostratigraphy agrees with the magnetostratigraphy derived from this site (see “Paleomagnetism” section, this chapter).

Zone NN21

Subzones NN21b and NN21a together occupy the top 7.6 mbsf of Hole 1085A. The first occurrence (FO) of the *Emiliania huxleyi* acme, the datum event for the Subzone NN21b/NN21a boundary, was identified within the top part of Core 175-1085A-2H (Samples 1H-CC to 2H-2, 90 cm) at the mean depth of 4.85 mbsf. Zone NN21 terminates between Samples 2H-2, 90 cm, and 2H-4, 90 cm (last occurrence [LO] of the *Gephyrocapsa caribbeanica* acme at 0.26 Ma), at the mean depth of 7.6 mbsf.

Zone NN20

This 0.2-m.y. interval terminates at 14.9 mbsf (between Samples 175-1085A-2H-CC and 3H-2, 1420 cm), which is the mean depth of the LO of the *Pseudoemiliania lacunosa* datum event.

Table 2. Microfossil datums at Hole 1085A.

Fossil group	Event	Age (Ma)	Zone (Base) A	Zone (Base) B	Core, section, interval (cm) Top	Core, section, interval (cm) Bottom	Depth (mbsf) Top	Depth (mbsf) Bottom	Depth (mbsf) Mean
					175-1085A-	175-1085A-			
N	FO *Emiliania huxleyi* acme	0.09	NN21b		1H-CC	2H-2, 90	3.59	6.10	4.85
N	FO *Emiliania huxleyi*	0.26	NN21a	CN15	2H2, 90	2H-4, 90	6.10	9.10	7.60
N	LO *Gephyrocapsa caribbeanica* acme	0.26	NN21a	CN16	2H2, 90	2H-4, 90	6.10	9.10	7.60
N	LO *Pseudoemiliania lacunosa*	0.46	NN20	CN14b	2H-CC	3H-2, 140	13.62	16.10	14.86
R	LO *Axoprunum angelinum*	0.46			2H-CC	3H-CC	13.62	23.19	18.41
N	LO Small *Gephyrocapsa* acme (Weaver, 1993)	0.6			4H-CC	5H-2, 140	31.56	35.10	33.33
N	LO *Reticulofenestra asanoi*	0.83			5H-4, 140	5H-CC	38.10	42.17	40.14
N	LO Small *Gephyrocapsa* acme (Gartner, 1977)	0.96			5H-CC	6H-CC	42.17	48.96	45.57
N	LO *Helicosphaera sellii*	1.25			7H-2, 130	7H-5, 10	54.00	57.30	55.65
N	LO *Calcidiscus macintyrei*	1.67			8H-CC	9H-2, 140	68.37	73.10	70.74
N	LO *Discoaster brouweri*	1.95	NN19	CN13a	10H-CC	11H-3, 10	89.67	92.30	90.99
D	LO *Thalassiosira convexa*	2.19			10H-CC	11H-CC	89.67	98.69	94.18
N	LO *Discoaster surculus*	2.55	NN18-17	CN12d-c	12H-CC	13H-CC	108.49	117.82	113.16
R	FO *Cycladophora davisiana*	2.7			12H-CC	13H-CC	108.49	117.82	113.16
N	LO *Discoaster tamalis*	2.83			13H-CC	14H-CC	117.82	127.45	122.64
N	LO *Reticulofenestra pseudoumbilicus*	3.82	NN16	CN12a	20H-CC	21H-CC	183.96	193.63	188.80
N	LO *Amaurolithus tricorniculatus*	4.5	NN15	CN11	24H-CC	25H-CC	221.90	230.99	226.45
N	FO *Discoaster asymmetricus*	5.02	NN14	CN10d	26H-CC	27H-CC	241.53	250.87	246.20
N	LO *Discoaster quinqueramus*	5.54	NN13-12	CN12c-a	32H-CC	33H-CC	296.87	304.90	300.89
N	LO *Amaurolithus amplificus*	5.9			35X-CC	36X-CC	324.57	333.90	329.24
N	FO *Amaurolithus amplificus*	6.6			39X-CC	40X-CC	363.27	372.61	367.94
N	FO *Discoaster quinqueramus*	8.6	NN11	CN9a	44X-CC	45X-CC	411.24	420.39	415.82
N	LO *Discoaster bollii*	9.1			46X-CC	47X-CC	430.62	440.56	435.59
N	LO *Discoaster hamatus*	9.63	NN10	CN8	48X-CC	49X-CC	450.25	459.81	455.03
N	FO *Discoaster hamatus*	10.7	NN9	CN7	54X-CC	55X-CC	507.04	517.38	512.21
N	LO *Discoaster kugleri*	11.5			58X-CC	59X-CC	546.36	556.07	551.22
N	FO *Discoaster kugleri*	11.8	NN8-7	CN6-5b	59X-CC	60X-CC	556.07	565.60	560.84
N	LO *Sphenolithus heteromorphus*	13.6	NN6	CN5a	62X-CC	63X-CC	584.97	594.60	589.79

Notes: Fossil group: N = calcareous nannofossils; R = radiolarians; and D = diatoms. FO = first occurrence and LO = last occurrence. Zonal codes refer to the calcareous nannofossil standard zonations of (A) Martini (1971) and (B) Okada and Bukry (1980).

Zone NN19

In addition to the zonal boundary events, five biohorizons were identified within this interval. Sedimentation rate estimates within the top part of this interval (Fig. 12B), from the Zone NN20/NN19 boundary (0.46 Ma) to the LO of the Small *Gephyrocapsa* acme (0.6 Ma), are the highest recorded over the entire section (17 cm/k.y.). The nannofossil-based stratigraphy of the early Pleistocene part of Hole 1085A agrees closely with the magnetostratigraphy between 40 and 90 mbsf (Fig. 12A). The base of Zone NN19 (1.95 Ma) was reached between Samples 175-1085A-10H-CC and 11H-3, 10 cm, at the mean depth of 91 mbsf.

Zones NN18–NN17

Zones NN18 and NN17 were combined because the LOs of *Discoaster pentaradiatus* (NN18/NN17 zonal boundary event) and *D. surculus* (NN17/NN16 zonal boundary) were identified within the same sampling interval. A refined biostratigraphy based on a higher resolution sampling will be done on shore to precisely constrain the upper boundary of the short-duration Zone NN17 (from 2.45 to 2.55 Ma). The base of Zone NN17 was identified between Samples 175-1085A-12H-CC and 13H-CC at the mean depth of 113.1 mbsf.

Zone NN16

This 1.27-m.y. interval is constrained within Hole 1085A between 113.1 and 188.8 mbsf. In addition to the zonal boundary events, a biohorizon dated at 2.83 Ma was identified between Samples 175-1085A-13H-CC and 14H-CC (LO of *D. tamalis*). Other useful diagnostic species for this zone are *D. decorus, D. challengeri,* and *D. variabilis.*

Zone NN15

The top of this interval is defined by the LO of *Reticulofenestra pseudoumbilica* (3.82 Ma), a datum event identified between Samples 175-1085A-20H-CC and 21H-CC. The LO of *D. pansus,* found within Core 175-1085A-24H, is a noncalibrated event used to differentiate an upper (CN11b) from a lower (CN11a) subzone within Zone NN15. *Amaurolithus delicatus,* the last representative of the nonbirefringent ceratoliths within the Pliocene, is found as a rare component of the calcareous nannofossil assemblage representative of Zone NN15. The Zone NN15/NN14 boundary is defined by the LO of *A. tricorniculatus* (4.5 Ma), a datum identified at the mean depth of 226.4 mbsf (Samples 24H-CC through 25H-CC).

Zone NN14

The base of this 0.52-m.y. interval was identified between Samples 175-1085A-26H-CC and 27H-CC (FO of *D. asymmetricus*; 5.02 Ma). This interval is marked by the first downhole occurrence of *Sphenolithus* sp.

Zones NN13–NN12

This 0.52-m.y. interval is constrained between the mean depths of 246.2 and 300.8 mbsf. Zone NN13 is combined with Zone NN12 because of the sparse occurrence of *Ceratolithus* spp. throughout this interval. The LO of *D. quinqueramus,* identified between Samples 175-1085A-32H-CC and 33H-CC, defines the NN12/NN11 zonal boundary.

Zone NN11

This 3.06-m.y. interval is defined as the range of *D. quinqueramus.* The range of *A. amplificus* (LO between Samples 175-1085A-35X-CC and 36X-CC; FO between Samples 175-1085A-39X-CC and 40X-CC) was used to refine the age model of this interval.

Zone NN10

The Zone NN11/NN10 boundary was identified at the mean depth of 415.8 mbsf (FO of *D. quinqueramus*; 8.6 Ma). The LO of *D. bollii*

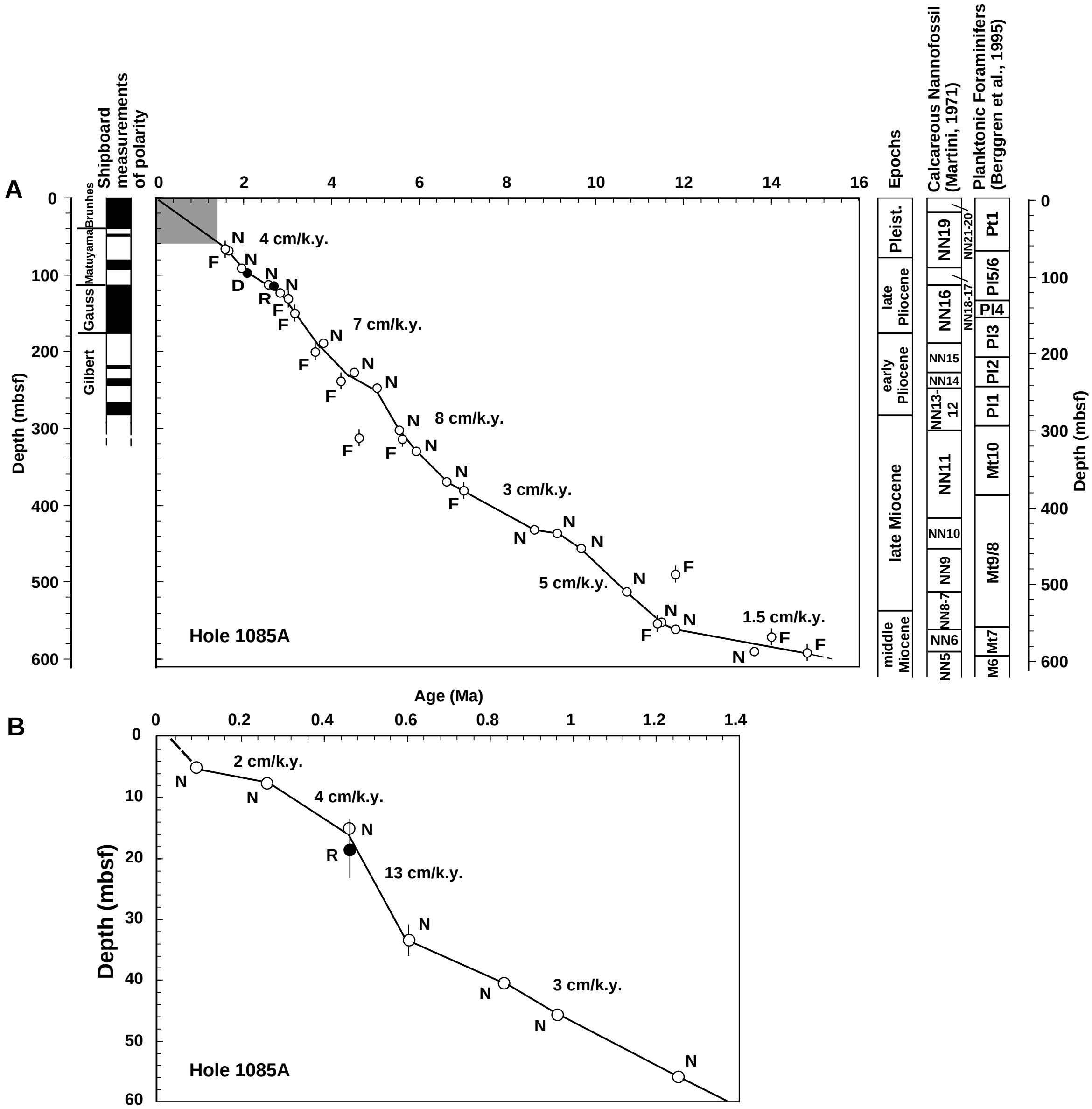

Figure 12. Age-depth plot and sedimentation rates estimated from calcareous microfossil (open circles; F = planktonic foraminifers and N = calcareous nannofossils) and siliceous microfossil (closed circles; D = diatoms and R = radiolarians) datums at Hole 1085A. Data are shown for (**A**) the Miocene and Pliocene of Hole 1085A and (**B**) the last 1.4 m.y. of Hole 1085A.

biohorizon (9.1 Ma; between Samples 175-1085A-46X-CC and 47X-CC) was used to further refine this interval.

Zone NN9

This interval is defined as the range of *D. hamatus.* Its FO event (10.7 Ma) was identified at the mean depth of 512.2 mbsf (between Samples 175-1085A-54X-CC and 55X-CC). *D. calcaris,* a diagnostic species within nannofossil assemblages from Zone NN9, is present throughout this interval.

Zones NN8–NN7

This interval extends from 10.7 to 11.8 Ma and therefore includes the Pliocene/Miocene boundary. The absence of *Catinaster coalitus,* whose FO is used to define the Zone NN8/NN7 boundary (11.3 Ma) from Hole 1085A, forced us to lump Zones NN8 and NN7 together. The LO of *D. kugleri* (11.5 Ma), identified between Samples 175-1085A-58X-CC and 59X-CC, might be used to approximate the Zone NN8/NN7 boundary.

Zone NN6

The base of this interval is defined by the LO of *Sphenolithus heteromorphus.* This biohorizon was identified within a slumped sequence in Core 175-1085A-63X at the mean depth of 589.7 mbsf. Age control for the bottom part of Hole 1085A is therefore based on planktonic foraminiferal datums identified within Cores 175-1085A-62X and 64X. The presence of *S. heteromorphus* within the undisturbed bottom Core 64X, however, indicates that Hole 1085A terminated within Zone NN5.

Planktonic Foraminifers

Site 1085 contains abundant planktonic foraminifers and, unlike previous Leg 175 sites, is not affected significantly by dissolution downcore.

The uppermost assemblage (Sample 175-1085A-1H-CC) is dominated by *Globigerina bulloides, Globorotalia inflata,* and *Neogloboquadrina pachyderma.* Other species that are present include *Globigerina quinqueloba, G. umbilicata, Globigerinella siphonifera, Globigerinoides ruber, G. sacculifer, G. crassaformis, G. hirsuta, G. scitula, G. truncatulinoides, N. dutertrei,* and *Orbulina universa.* The presence of a warm-water species (including one endemic to the Indo-Pacific Ocean, *G. hexagona*) downcore (e.g., Sample 175-1085A-7H-CC) indicates transport of warm Indian Ocean water around the cape by the Agulhas Current.

The zonation was based on the temperate *G. conoidea–G. sphericomiozea* lineage, but the sporadic presence of warmer water fauna increased the number of datums, and good age control was achieved (Table 3). There is generally very good agreement among the datums with calcareous nannofossil biostratigraphy and magnetostratigraphy, despite the large sampling interval (usually every other core catcher). Because of time constraints, the complete assemblage could not be analyzed and, therefore, some of the FOs and LOs could not be precisely defined. The premature FOs and LOs in the age-depth plot (Fig. 12) are attributed to the large sampling interval. For example, the LO of *G. cibaoensis* is in Sample 175-1085A-35X-CC, at the same depth as the FO of *G. sphericomiozea*. *G. sphericomiozea* has a very brief range in the early Pliocene, and its last-appearance datum (LAD) is 5.6 Ma, 1 m.y. earlier than the LAD of *G. cibaoensis.* The true LO of *G. cibaoensis* at Hole 1085A is probably higher, between Samples 175-1085A-32H-CC, which did not contain *G. cibaoensis,* and 35X-CC.

Pleistocene

Pleistocene Zone Pt1 (0–65 mbsf) encompasses Samples 175-1085A-1H-CC through 7H-CC (range of *G. truncatulinoides*).

Upper Pliocene

Zones Pl5 and Pl6 (65–127 mbsf) were not differentiated at Site 1085 because the boundary between the two zones is defined based on (sub)tropical faunas that are not present (e.g., *G. miocenica*).

Zone Pl4 (127–147 mbsf) ranges from the LAD of *D. altispira* (3.09 Ma; Sample 175-1085A-15H-CC) to the LAD of *S. seminulina* (3.12 Ma; Sample 175-1085A-17H-CC). Zone Pl3 (147–203 mbsf) ranges from Sample 17H-CC (LO of *S. seminulina*) through 21H-CC (LO of *G. margaritae*).

Lower Pliocene

The LAD of *G. margaritae* (3.58 Ma) and the LAD of *G. nepenthes* (4.18 Ma) define Zone PL2 (Samples 175-1085A-23H-CC through 29H-CC, 203–287 mbsf). *G. margaritae* is not present in Sample 25H-CC, but there is some evidence for dissolution (pyrite), and the species is very dissolution susceptible. Sample 29H-CC contains a specimen of *G.* cf. *nepenthes* that would render an age assignment to the older Zone Pl1, but the sample also contains *G. sphericomiozea.* The base of Zone Pl1 is approximated by the first-appearance datum (FAD) of *G. sphericomiozea* (Sample 29H-CC, 287 mbsf). Thus, Zones Pl1 and Pl2 are not differentiated.

Miocene

The FAD of *G. sphericomiozea* (Sample 175-1085A-29H-CC) marks the Miocene/Pliocene boundary (5.6 Ma) as the top of Zone Mt10 (287–382 mbsf). The base of Zone Mt10 is defined as the FAD of *G. conomiozea* (7.12 Ma) and occurs in Sample 175-1085A-42X-CC. Zones Mt9 and Mt8 are not differentiated in this study and are bounded by the LAD of *G. mayeri* (top of Zone Mt9; 7.12, Ma) and the FAD of *G. nepenthes* (bottom of Zone Mt8; 11.8 Ma). Zones Mt9 and Mt8 are present in Samples 175-1085A-44X-CC through 56X-CC (382–555 mbsf), although the species are not present in every sample. Zone Mt7 ranges from the FAD of *G. nepenthes* to the LAD of *G. peripheroronda* (14.0 Ma) and is represented only in Sample 175-1085A-62X-CC (555–589 mbsf). The base of the underlying zone, subtropical Zone Mt6, was not reached. The lowermost portion of transitional Zone Mt6 is described by subtropical Zone M6. The top of Zone M6 is defined as the FAD of *G. peripheroacuta.* This species is found in Sample 175-1085A-64X-CC (589–604 mbsf) and constrains the age to 15.1–14.8 Ma. Sample 63X-CC is a slumped interval.

Benthic Foraminifers

The benthic foraminiferal fauna of Site 1085 was studied in selected core-catcher samples from Hole 1085A. The overall abundance of benthic foraminifers was high throughout the studied interval, except for the lowermost core catcher (Sample 175-1085A-64X-CC; 604.29 mbsf), which contained rare to few benthic foraminifers (Table 4). The planktonic to benthic ratio at this site is very high, about ten times higher than at previous sites. Preservation is good throughout Hole 1085A.

The uppermost two samples (Samples 175-1085A-1H-CC [3.59 mbsf] and 3H-CC [23.19 mbsf]) are strongly dominated by *Bulimina aculeata* and *Epistominella exigua* (Table 4; Fig. 13). Farther downcore, the dominating species are *Trifarina angulosa* and *Cassidulina*

Table 3. Planktonic foraminiferal datums at Hole 1085A.

Event	Age (Ma)	Zone	Core, section, interval (cm) Top	Core, section, interval (cm) Bottom	Depth (mbsf) Top	Depth (mbsf) Bottom	Depth (mbsf) Mean
			175-1085A-	175-1085A-			
FO *Globorotalia truncatulinoides*	1.77	Pt1a bottom	7H-CC	8H-CC	61.03	68.37	64.70
LO *Dentoglobigerina altispira*	3.09	Pl4 top	14H-CC	15H-CC	127.45	137.07	132.26
LO *Sphaeroidinellopsis* spp.	3.12	Pl3 top	16H-CC	17H-CC	143.61	156.43	150.02
LO *Globorotalia margaritae*	3.58	Pl2 top	22H-CC	23H-CC	203.59	213.22	208.41
LO *Globigerina nepenthes*	4.18	Pl1b top	26H-CC	27H-CC	241.53	250.87	246.20
LO *Globorotalia cibaoensis*	4.60	Pl1a top	34X-CC	35X-CC	314.64	324.57	319.61
FO *Globorotalia sphericomiozea*	5.60		35X-CC	36X-CC	324.57	333.90	329.24
FO *Globorotalia conomiozea*	6.90	MT10 bottom	40X-CC	41X-CC	372.61	382.52	377.57
LO *Neogloboquadrina mayeri*	11.40	MT8 top	59X-CC	60X-CC	556.07	565.60	560.84
FO *Globorotalia nepenthes*	11.80	MT8 bottom	50X-CC	51X-CC	467.20	~478.00	473.00
LO *Globorotalia peripheroronda*	14.00	MT6 top	61X-CC	62X-CC	565.60	584.94	575.27
FO *Globorotalia peripheroacuta*	14.80	M7 bottom	62X-CC	63X-CC	584.97	594.60	589.79

Note: FO = first occurrence and LO = last occurrence.

Table 4. Relative abundance of benthic foraminiferal species and overall abundance of benthic foraminifers at Hole 1085A.

Core, section, interval	Depth (mbsf)	Abundance	Anomalinoides globulosus	Anomalinoides semicribratus	Astrononion novozealandicum	Astrononion stelligerum	Baggina sp. 1	Bolivina pseudoplicata	Bolivina seminuda	Bolivina subaenarensis	Bolivinopsis cubensis	Bulimina aculeata	Bulimina exilis	Bulimina mexicana	Bulimina truncana	Bulimina tuxpamensis	Cassidulina laevigata	Cassidulina minuta	Cassidulinoides cf. bradyi	Chilostomella ovoidea	Cibicidoides bradyi	Cibicidoides pachyderma
175-1085A-																						
1H-CC	3.59	A			2				+	8		28	+	+	+		2			+	3	5
3H-CC	23.19	A			+	+			4			35	+		+		5					+
5H-CC	42.17	A				+				4			+	1	2		29		+		1	
7H-CC	61.03	A	1									15	+	+			23				+	3
9H-CC	80.12	A							+			+		4			2				+	2
11H-CC	98.69	A						2	+					8					+	+		
13H-CC	117.82	A												3				+				
15H-CC	137.07	A			5									3							+	3
17H-CC	156.43	A												7	+							
19H-CC	175.29	A	+							14			+	4	+		+	+	+			+
21H-CC	193.63	A	9							5				8	1						+	4
23H-CC	213.22	A	3							10				+	12						1	+
25H-CC	230.99	A					5		+	25				2							5	3
27H-CC	250.87	A	+				2			26				5	3						2	1
31H-CC	288.98	A	2				+			8				5	4						3	8
33H-CC	304.90	A								2				1	67						1	3
35X-CC	324.57	A	2							3				4	7						3	6
37X-CC	343.86	A			+					4				7	5			+			+	3
39X-CC	363.27	A	5		2		+	1		5	+			3	9			+			3	7
41X-CC	382.52	A	5		3			+		9				1	10			1	+		1	11
43X-CC	402.04	A			+			+		10					8						4	8
45X-CC	420.39	A								7				3	11						3	26
47X-CC	440.56	C	1							7				6	21						3	13
49X-CC	459.81	A	+							3				2					+		5	3
51X-CC	478.77	A			1					13				2							2	
53X-CC	497.97	A		8						5				2	2						3	6
55X-CC	517.38	A		1						3				4	10							4
57X-CC	536.72	A		8					+	5				10	2						5	16
59X-CC	556.07	A		2		2								2							2	15
61X-CC	575.39	C		3	2					4					3			+	+		2	7
63X-CC	594.60	C		1						5				+		1					1	4
64X-CC	604.29	T		P						P					P	P						P

Core, section, interval	Cibicidoides wuellerstorfi	Dorothia cf. brevis	Eggerella bradyi	Ehrenbergina bradyi	Ehrenbergina trigona	Epistominella exigua	Fissurina spp.	Fursenkoina fusiformis	Fursenkoina sp. 1	Gavelinopsis lobatulus	Globocassidulina subglobosa	Gyroidinoides soldanii	Hoeglundina elegans	Karreriella bradyi	Laticarinina pauperata	Martinottiella communis	Melonis barleeanum	Nonionella turgida	Oolina spp.	Oridorsalis umbonatus
175-1085A-																				
1H-CC	+		+			18	+		+	5	2	+	+				+			4
3H-CC	4					24			7		2	+					+	+	+	+
5H-CC	3		+			5		+	3		2	2	2	+	+					2
7H-CC	2		+			+		+	2			+	1	+			+			2
9H-CC	6					25	+		+	12	+	+	4			+				3
11H-CC	1					3	1			1		+	8						+	4
13H-CC	4					+	2		+	3	+	4	4				3			20
15H-CC	2		5			5	2			2	3	3	25		2	1	4		+	5
17H-CC	3	+					3		+	2		+	5	1	+				+	1
19H-CC	5	+				2						+	3				3			9
21H-CC	4	+	2		3		3			+	3	1	6	1	+		3			3
23H-CC	15		1		4		2		+		3	1	+				+			1
25H-CC	6		2			5	+		+			2	6	1			4			5
27H-CC	2		1			2	+				+	5	8		+	+	6			3
31H-CC	6		2			5	+				4	2	2	+		+	8			3
33H-CC	+		+			2	+				+	+	3				+			2
35X-CC	+	+	1			1	2				16	+	2	+		+	4		+	1
37X-CC	+	+				4	1				13	3	9	+			4			8
39X-CC	2		+		+	3	+				7	3	2	1		+	6			11
41X-CC	1		2			2	3				8	2	1	2		2	1		+	6
43X-CC			+			6	1				5			+			+			5
45X-CC	3		2			2					16				+	+	+			9
47X-CC			+			1	1				4	1	4	2	+	+	4			2
49X-CC	+		2			14	3				7	3					12			5
51X-CC	1					3	2				5	2	3	+		2	18			1
53X-CC			3			7					3	2				2	13			8
55X-CC	5	+	+	+		4	2			+	17	1				+	4		+	4
57X-CC	7		1			9	+				4	2			+	2	1			5
59X-CC	7		+			9					8	2				+	2			12
61X-CC	5					2	2				9	4		+						16
63X-CC	8	+									11				+	+	+			7
64X-CC											P									P

Core, section, interval	Osangularia culter	Plectofrondicularia cf. inaequalis	Plectofrondicularia cf. raricosta	Pleurostomella alternans	Praeglobobulimina/Globobulimina group	Pullenia bulloides	Pullenia subcarinata	Pyrgo spp.	Quadrimorphina allomorphinoides	Rectuvigerina multicostata	Sigmoilinopsis schlumbergeri	Siphotextularia concava	Siphotextularia curta	Siphotextularia rolshauseni	Sphaeroidina bulloides	Stilostomella spp.	Trifarina angulosa	Trifarina bradyi	Triloculina tricarinata	Uvigerina auberiana	Uvigerina hispida	Uvigerina hispidocostata	Uvigerina peregrina	Unidentified	Number of specimens counted
175-1085A-																									
1H-CC					+	+	2	+	+		+		+		3		2					1	2	5	327
3H-CC						+	2	6			+						+		1					3	322
5H-CC		+				3	+	2	2		2					4	22			+		2	+	3	330
7H-CC	+				1	1	1	2	+		1		+		1	6	+			4	1	13	5	6	365
9H-CC	+	+					+	2							2	10				+		2	15	8	312
11H-CC		+		+	+	2	1	1	+		3				+	6				+		+	43	8	270
13H-CC	+			1		10	4	3							+	5				7		3	14	6	191
15H-CC		+		+	+	2	+	4			2	4			+	4				2		5		6	311
17H-CC		+	+	+	+	2		8				4	+	+	20	11				7		15		5	307
19H-CC		1		+	+	4	+	2	2		+	+		+	2	6				4		22	+	7	326
21H-CC	+	+		+		1	+	+			+		+		13	1				10		10		4	354
23H-CC				+	+	+	2	+	+		+	2		+	10	2				19		+		6	369
25H-CC	+	+		2	1	+	+	2	+			+			8	4				+				7	327
27H-CC					+	+	+	5				+		+	+	3	+			3	2	5		8	219
31H-CC						2	2				4				3	1	2			6	2	4		12	264
33H-CC				+	1	+	2	+			1				1	+				3				6	387
35X-CC			+	+	+	4	+	2	+		2		+		2	11				4	6	6		9	396
37X-CC		+			1		3	2		5					2	5				6	+	3		8	158
39X-CC	+	+	+	+	+	1	1	+	+		+			+	+	+	+			3	1	4	+	9	326
41X-CC						+		3			1				3	1				7	1	7		8	196
43X-CC		1				3		2	+		4				4	2				18	+	2		12	330
45X-CC						+		1		2					2	1				8	+	4			194
47X-CC						1	+	+			3				4	2				+	1	4	1	9	296
49X-CC		+		+	+	5	+	2			3				+	3				8				14	173
51X-CC	+					6		3			2			1	1	2				8	+			22	193
53X-CC	2	+				3		2		2					4					6		2		15	127
55X-CC						6	+	+							7	5					+	3		14	257
57X-CC	+			+			2	+							5	2		+		+				10	217
59X-CC	+			+		7	2							+	4	3				+				18	121
61X-CC	2			+		3	3	2							2					2				26	133
63X-CC						3				5	1				7	3		1		5	+			29	136
64X-CC	P					P				P	P									P				P	35

Notes: The relative abundance of benthic foraminiferal species is given as a percentage, where + = <1% and P = present (the relative abundance was not calculated because of small sample size). Absolute abundance (per ~20 cm^3 of sediment) of benthic foraminifers is given as A = abundant (>500 specimens); C = common (250–500 specimens); F = few (100–249 specimens); R = rare (50–99 specimens); T = trace (1–49 specimens); and B = barren (no specimens).

laevigata (Sample175-1085A-5H-CC; 42.17 mbsf), *Uvigerina hispidocostata* (Sample 175-1085A-7H-CC; 61.03 mbsf), *E. exigua* and *Gavelinopsis lobatulus* (Sample 175-1085A-9H-CC; 80.12 mbsf), *Uvigerina peregrina* (Sample 175-1085A-11H-CC; 98.69 mbsf), *Oridorsalis umbonatus* (Sample 175-1085A-13H-CC; 117.82 mbsf), *Hoeglundina elegans* (Sample 175-1085A-15H-CC; 137.07 mbsf), *U. hispidocostata* and *Sphaeroidina bulloides* (Sample 175-1085A-17H-CC; 156.43 mbsf), and *U. hispidocostata* (Sample 175-1085A-19H-CC; 175.29 mbsf; see Table 4 and Fig. 13). Several of these species are more or less restricted to the peaks in relative abundance and are absent elsewhere in the studied sequence (i.e., *B. aculeata*, *C. laevigata*, *G. lobatulus*, *T. angulosa*, and *U. peregrina*).

The early Pliocene (175–280 mbsf) is dominated by *Bolivina subaenarensis*, *Cibicidoides wuellerstorfi*, and *Uvigerina auberiana* (Table 4; Fig. 13). The upper Miocene sequence is dominated by *U. auberiana*, *Globocassidulina subglobosa*, *Cibicidoides pachyderma*

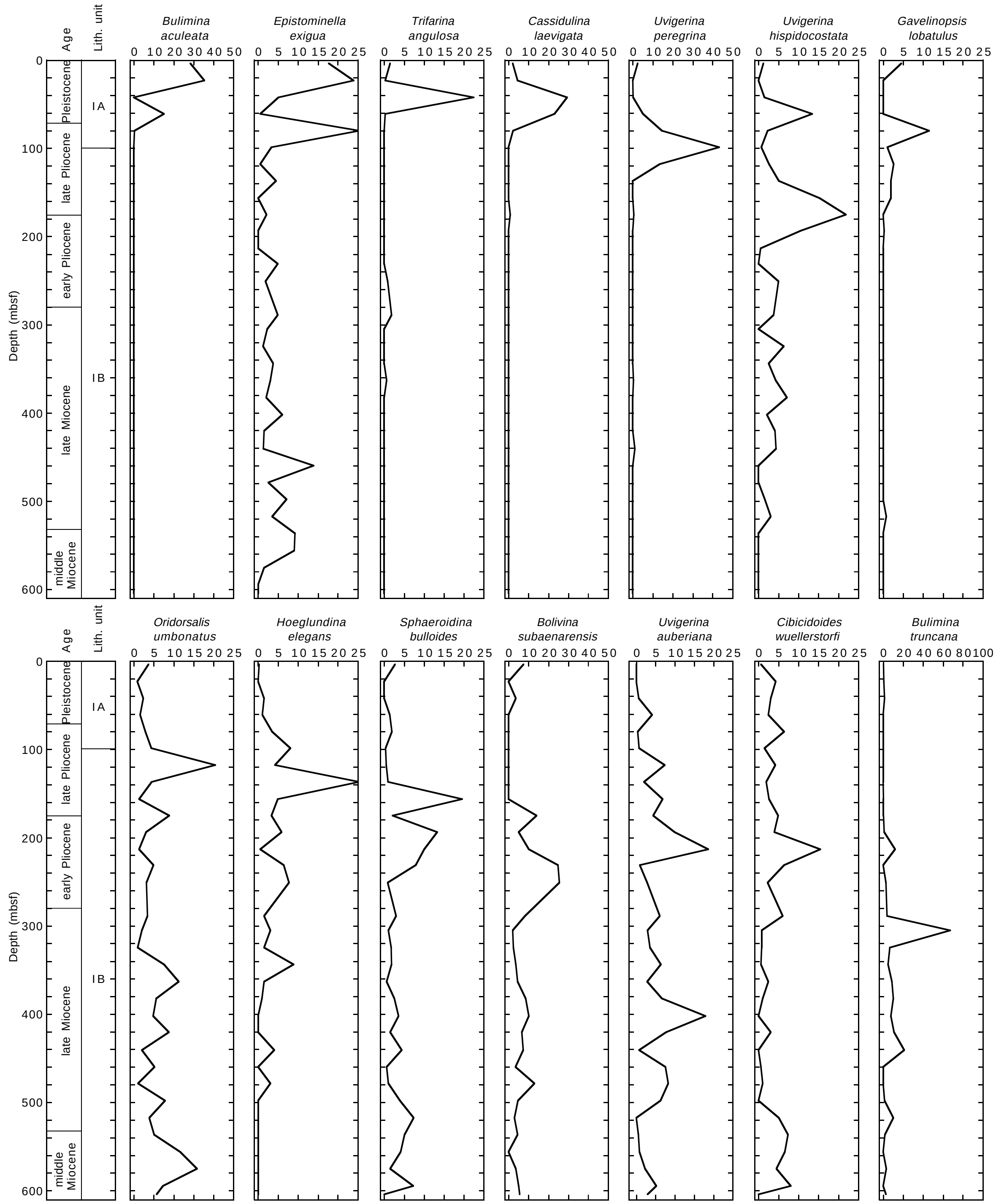

Figure 13. Relative abundances (in percentages) for selected benthic foraminiferal species. See "Lithostratigraphy" section (this chapter) for a description of lithostratigraphic units. (Continued next page.)

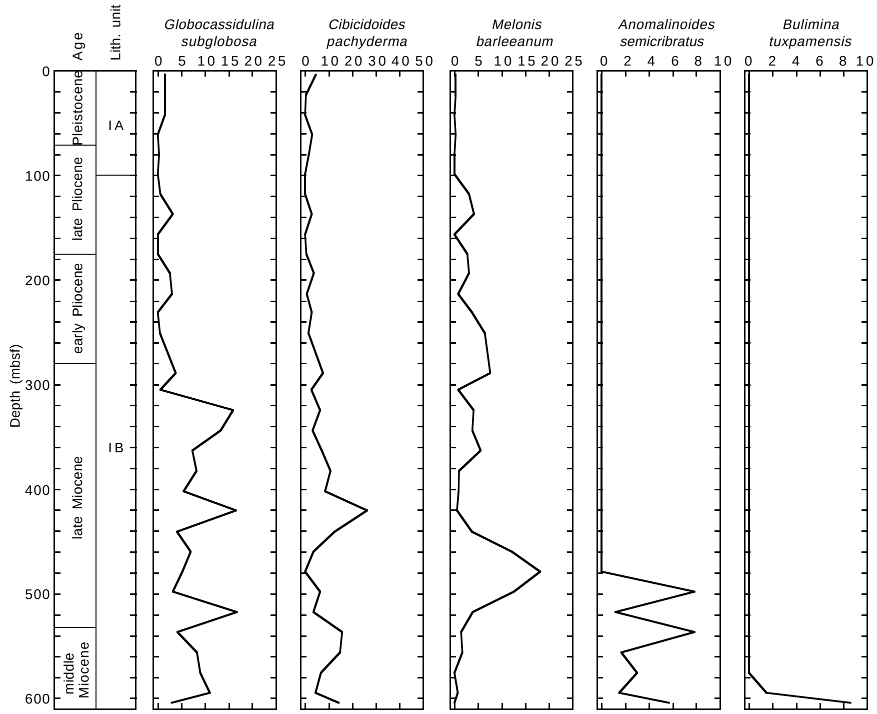

Figure 13 (continued).

and in the lower part *E. exigua* and *Melonis barleeanum* (Table 4; Fig. 13).

The middle Miocene sequence is dominated by *C. pachyderma, C. wuellerstorfi, E. exigua, G. subglobosa,* and *Oridorsalis umbonatus* (Table 4; Fig. 13).

The species *Anomalinoides semicribratus* was found in Samples 175-1085A-53X-CC through 64X-CC (497.97–604.29 mbsf; see Table 4 and Fig. 13). This species has a reported LO in the middle Miocene (N12), but forms transitional from *A. semicribratus* to *Anomalinoides globulosus* occur in Zones N13–N14 (Van Morkhoven, et al., 1986). In Hole 1085A, *Anomalinoides globulosus* has its FO in Sample 175-1085A-49X-CC (459.81 mbsf; see Table 4 and Fig. 13).

The species *Bulimina tuxpamensis* was found in the two lowermost core catchers (Samples 175-1085A-63X-CC [594.60 mbsf] and 64X-CC [604.29 mbsf]). This species has a known range from the late Paleocene through early middle Miocene (N9), but has been recorded in middle Miocene Zones N10–N13 (Van Morkhoven, et al., 1986), which further confirms the middle Miocene age for the base of Hole 1085A.

Radiolarians

Radiolarians are generally rare and show signs of dissolution in almost all samples examined down to Sample 175-1085A-15H-CC, although concentrations by the sample preparation often produces high abundances of radiolarians in the assemblage slides. From Sample 175-1085A-16H-CC to the deepest core catcher, radiolarians are virtually absent (Table 5).

The absence of *Axoprunum angelinum* indicates that the uppermost Samples 175-1085A-1H-CC and 2H-CC belong to Zone NR1 of Caulet (1991). It was not possible to determine a zone for samples below Sample 2H-CC because of the scarcity or absence of age-diagnostic taxa. The FO of *Cycladophora davisiana* indicates an age of 2.70 Ma for Sample 12H-CC.

Axoprunum stauraxonium and the *Ellipsoxiphus attractus* group are common in Samples 175-1085A-1H-CC, 2H-CC, 3H-CC, 7H-CC, 9H-CC, 15H-CC, 16H-CC, 23H-CC, 31H-CC, 34X-CC, and 35X-CC, indicating low productivity under subtropical warm-water conditions. The radiolarian assemblages that are characterized by common *C. davisiana* suggest upwelling conditions for Samples 175-1085A-4H-CC, 6H-CC, 8H-CC, and 10H-CC. Thus, intermittent upwellings seem to have occurred in a warm-water condition through the last ~3 m.y. in the Northern Cape Basin area. The occurrence of an Antarctic species *Cycladophora pliocenica* in Sample 175-1085A-14H-CC indicates an influence of cooler current into the area.

Diatoms

Core-catcher samples from Hole 1085A were analyzed for their diatom content. Samples were prepared as smear slides and were acid-cleaned. The treated samples were washed with distilled water and sieved through a 20-µm sieve. Diatoms are absent in most core-catcher samples. From 304.90 mbsf (just below the Pliocene/Miocene boundary) through the end of the hole (604.29 mbsf; middle Miocene), the sediments are barren of diatoms. Trace amounts are found in Samples 175-1085A-1H-CC (3.59 mbsf) through 9H-CC (80.12 mbsf), 27H-CC (250.87 mbsf), 29H-CC (269.64 mbsf), 31H-CC (288.98 mbsf), 32H-CC (296.87), 35X-CC (324.57 mbsf), 39X-CC (363.27 mbsf), and 48X-CC (450.25 mbsf). It is only the interval between Samples 10H-7, 47 cm (89.17 mbsf), and 14H-CC (127.45 mbsf) that contains rare to few diatoms. It is interesting to note that this interval includes a mixed *Thalassiothrix antarctica*–rich assemblage (composed of Southern Ocean species, *Chaetoceros* spores, warm-oceanic species, and abundant nannofossils) similar to that at Site 1084, although overall abundances are much lower. As was the case for Site 1084, the interval at Hole 1085A occurs in the late Pliocene (~1.8–2.6 Ma).

Sponge spicules are particularly abundant in the Pleistocene and upper Pliocene sediments, from Sample 175-1085A-1H-CC to Sample 15H-CC, 3.59 to 137.07 mbsf, and are absent from Sample 175-1085A-36X-CC (333.90 mbsf) to the end of the hole. One interesting feature at Site 1085 is that dinoflagellate cysts are common in the upper Miocene sequence, between Samples 175-1085A-38X-CC

Table 5. Stratigraphic distribution of radiolarians at Hole 1085A.

Age	Zone	Core, section, interval	Depth (mbsf)	Abundance	Preservation	*Cycladophora davisian*	*Didymocyrtis tetrathalamus*	*Lamprocyclas hannai*	*Axoprunum angelinum*	*Eucyrtidium calvertense*	*Amphirhopalum ypsilon*	*Spongurus pylomaticus*	*Pterocanium trilobum*	*Theocorythium trachelium*	*Eucyrtidium acuminatum*	*Eucyrtidium teuscheri*	*Pterocanium praetextum eucolpum*	*Cycladophora cornutoides*	*Saturnalis circularis*	*Lamprocyrtis heteroporos*	*Cycladophora sakaii*	*Lamprocyrtis neoheteroporos*	*Cycladophora pliocenica*	*Stichocorys delmontensis*	*Stichocorys peregrina*	*Cyrtocapsella tetrapera*
		175-1085A-																								
Quaternary	NR1	1H-CC	3.59	R	M																					
Quaternary	NR1	2H-CC	13.62	F	M	P	P	+																		
Pleistocene–Pliocene	Unzoned	3H-CC	23.19	F	M	+	+	P	+	P																
Pleistocene–Pliocene	Unzoned	4H-CC	31.56	A	M	P	P		P	P																
Pleistocene–Pliocene	Unzoned	5H-CC	42.17	A	M	P	P	+		P	+	+														
Pleistocene–Pliocene	Unzoned	6H-CC	48.96	A	M	P	P	P	P	P	+		+	+												
Pleistocene–Pliocene	Unzoned	7H-CC	61.03	C	M	P	+	P	P	P	+				+											
Pleistocene–Pliocene	Unzoned	8H-CC	68.37	A	M	P	P	P	P	P	+	+	P		+	+	P									
Pleistocene–Pliocene	Unzoned	9H-CC	80.12	A	M	+		+		+																
Pleistocene–Pliocene	Unzoned	10H-CC	89.67	A	M	P	+	P	P	P	P	P	P	+	P	P	P	+	P							
Pleistocene–Pliocene	Unzoned	11H-CC	98.69	A	M	P	P	P	P	P	P		+		P					+						
Pleistocene–Pliocene	Unzoned	12H-CC	108.49	A	M	P	P	P	P	P	P	+	P		P	P	P			P	+					
Pliocene	Unzoned	13H-CC	117.82	A	M		P	P	P	P	+	+				+				P		+				
Pliocene	Unzoned	14H-CC	127.45	A	M		P		P	P					+	+				P			P			
?	Unzoned	15H-CC	137.07	A	M			P	P	P																
		16H-CC	143.61	T	P																					
		17H-CC	156.43	B																						
		18H-CC	165.64	B																						
		19H-CC	175.29	B																						
		20H-CC	183.96	T																						
		21H-CC	193.63	B																						
?	Unzoned	22H-CC	203.59	R	M					+																
Pliocene?	Unzoned	23H-CC	213.22	C	M			P	+	P										P		P		+	P	
		24H-CC	221.90	B																						
		25H-CC	230.99	B																						
		26H-CC	241.53	B																						
		27H-CC	250.87	B																						
		28H-CC	259.37	B																						
		29H-CC	269.64	B																						
		31H-CC	288.98	F	M																					
		32H-CC	296.87	F	M																					
		33H-CC	304.90	B																						
?	Unzoned	34X-CC	314.64	R	P					P																
?	Unzoned	35X-CC	324.57	C	M		+		P										P	+						P
		36X-CC	333.90	B																						
		37X-CC	343.86	B																						
		38X-CC	353.57	B																						
		39X-CC	363.27	B																						
		40X-CC	372.61	B																						
		41X-CC	382.52	B																						
		42X-CC	392.20	B																						
		43X-CC	402.04	B																						
		44X-CC	411.24	B																						
		45X-CC	420.39	B																						
		46X-CC	430.62	B																						
		47X-CC	440.56	B																						
		48X-CC	450.25	B																						
		49X-CC	459.81	B																						
		50X-CC	467.20	B																						
		52X-CC	488.27	B																						
		53X-CC	497.97	B																						
		54X-CC	507.04	B																						
		55X-CC	517.38	B																						
		56X-CC	526.73	B																						
		57X-CC	536.72	B																						
		58X-CC	546.36	B																						
		59X-CC	556.07	B																						
		60X-CC	565.60	B																						
		62X-CC	584.97	T	P																					
		63X-CC	594.60	B																						
		64X-CC	604.29	B																						

Notes: Occurrence is indicated by P = present and + = one specimen per slide. Abundance: R = rare; F = few; A = abundant; C = common; T = trace; and B = barren. Preservation: M = moderate and P = poor.

Table 6. Tensor tool–orientation data for cores from Holes 1085A and 1085B.

Core	MTF (°)	Inclination angle
175-1085A-		
16H	328	0.73
17H	101	1.32
18H	301	0.42
19H	267	0.37
20H	282	0.92
21H	148	0.39
22H	253	0.61
23H	5	0.56
24H	266	0.67
25H	292	0.60
26H	176	0.66
27H	171	0.79
175-1085B-		
3H	132	0.31
4H	302	0.30
5H	170	0.22
6H	25	0.29
7H	298	0.13
8H	281	0.13
9H	160	0.39
10H	198	0.44
11H	60	1.01
12H	304	0.18
13H	292	0.27
14H	97	0.37
15H	70	0.52
16H	322	0.68
17H	291	0.64
18H	127	0.65
19H	70	0.92
20H	230	0.74
21H	164	0.57
22H	324	0.35
23H	115	0.49
24H	34	0.46
25H	329	0.35
26H	177	0.68
31H	77	0.73
32H	161	0.80
33H	161	0.95
34H	21	0.95
35H	339	0.81

Notes: The orientation parameter (MTF) is the angle in degrees between magnetic north and the double line marked on the center of the working half of the core. The local declination anomaly is 19°W.

(353.57 mbsf) and 51X-CC (478.77 mbsf), with an approximate age of 6–10 Ma.

PALEOMAGNETISM

The investigation of magnetic properties at Site 1085 included the measurement of bulk susceptibility of whole-core sections and the natural remanent magnetization (NRM) of archive-half sections and discrete samples. The Tensor tool was used to orient Cores 175-1085A-16H through 27H, 175-1085B-3H through 26H, and 175-1085B-31H through 35H (Table 6). Cores 175-1085A-4H through 15H, 175-1085A-28H through 33H, and 175-1085B-27H through 30H were not oriented because of technical problems with the Tensor tool.

Natural Remanent Magnetization, Magnetic Susceptibility, and Magnetic Overprint

Measurements of NRM were made on all archive-half core sections from Holes 1085A and 1085B. APC core sections from Hole 1085A were demagnetized by AF at 10 and 20 mT. XCB sections from Hole 1085A and all sections from Holes 1084B were demagnetized by AF at 20 mT only. Measurements of discrete samples were performed only when half-core measurements indicated strong enough intensities to be measured on board after AF demagnetization (~10^{-4} A/m in half-core measurements). Discrete samples from APC cores were demagnetized by AF at 10, 15, 20, and 25 mT, and those from Cores 175-1085A-58X through 64X were demagnetized at 0, 10, 20, 25, 30, and 35 mT. Magnetic susceptibility measurements were made on whole cores from all holes as part of the MST analysis (see “Physical Properties” section, this chapter).

The intensity of NRM after 20-mT demagnetization is between ~10^{-3} and 10^{-5} A/m in the upper 537 mbsf (Fig. 14) and abruptly increases to ~10^{-2} A/m below 537 mbsf. The magnetic susceptibility shows a similar sudden increase from ~10 to 40 × 10^{-5} (SI volume units) at ~540 mbsf. Except for this, long-term variations of remanent intensity and magnetic susceptibility do not coincide. For example, magnetic susceptibility increases below ~400 mbsf, but remanent intensity does not.

Except for the uppermost ~40 mbsf, the APC cores show significant coring-induced magnetization (CIM) with a radial-inward direction (see “Paleomagnetism” sections, “Site 1077” and “Site 1081” chapters, this volume). The CIM is evident from the disagreement of the declinations between (archive) half-core measurements and discrete samples from working halves: the former tend to cluster around 0° and the latter around 180° before orientation (Fig. 14A). In contrast, inclinations showed distinct polarity biases after 20-mT demagnetization, from which we could interpret the polarity (Fig. 14A, right panel).

Below ~430 mbsf at Hole 1085A, the declinations of XCB cores cluster at ~–20°, independent of the orientation of the sediments. This direction was pervasively observed in all XCB cores at previous sites (see “Paleomagnetism” sections, “Site 1081,” “Site 1082,” and “Site 1084” chapters, this volume). Below 537 mbsf, where the remanent intensity is strong (~10^{-2} A/m), inclinations of discrete samples clearly separated into positive and negative groupings after AF demagnetization (Fig. 15). We interpret these distinct groupings as the polarity of NRM. Between 430 and 537 mbsf, some structures are visible in the inclination data of half-core measurements, but it is difficult to assign a polarity. The remanent intensity of this depth interval is too weak to measure the discrete samples on board. Between 305 and 430 mbsf, the tendency of the declinations to cluster around –30° is very weak, suggesting a weaker magnetic overprint. However, the inclinations did not show any polarity bias and precluded a magnetostratigraphic interpretation.

Magnetostratigraphy

We identified the polarity of the NRM mainly from the inclinations of APC cores (Fig. 14). The major polarity chrons from the Brunhes to the earliest part of the Gilbert (~5.5 Ma) could be identified, although the quality of the record is not good because of the severe magnetic overprint. The magnetostratigraphic interpretation is summarized in Table 7. The time scale of Berggren et al. (1995) was used. This interpretation agrees well with the biostratigraphic ages (see “Biostratigraphy and Sedimentation Rates” section, this chapter).

The inclinations of discrete samples from XCB cores below 537 mbsf suggest that the sediments recorded more than 10 polarity reversals. Biostratigraphic ages range from ~11 to 15 Ma. Magnetic polarity reversals were frequent during this period of time, which supports our interpretation of the inclinations, although it is difficult to correlate it with the time scale at present.

COMPOSITE SECTION

At Site 1085 two holes were cored with a maximum penetration of 604 meters below seafloor (mbsf). Physical properties and color reflectance data were measured at 2-cm (Hole 1085A, 0–100 mbsf)

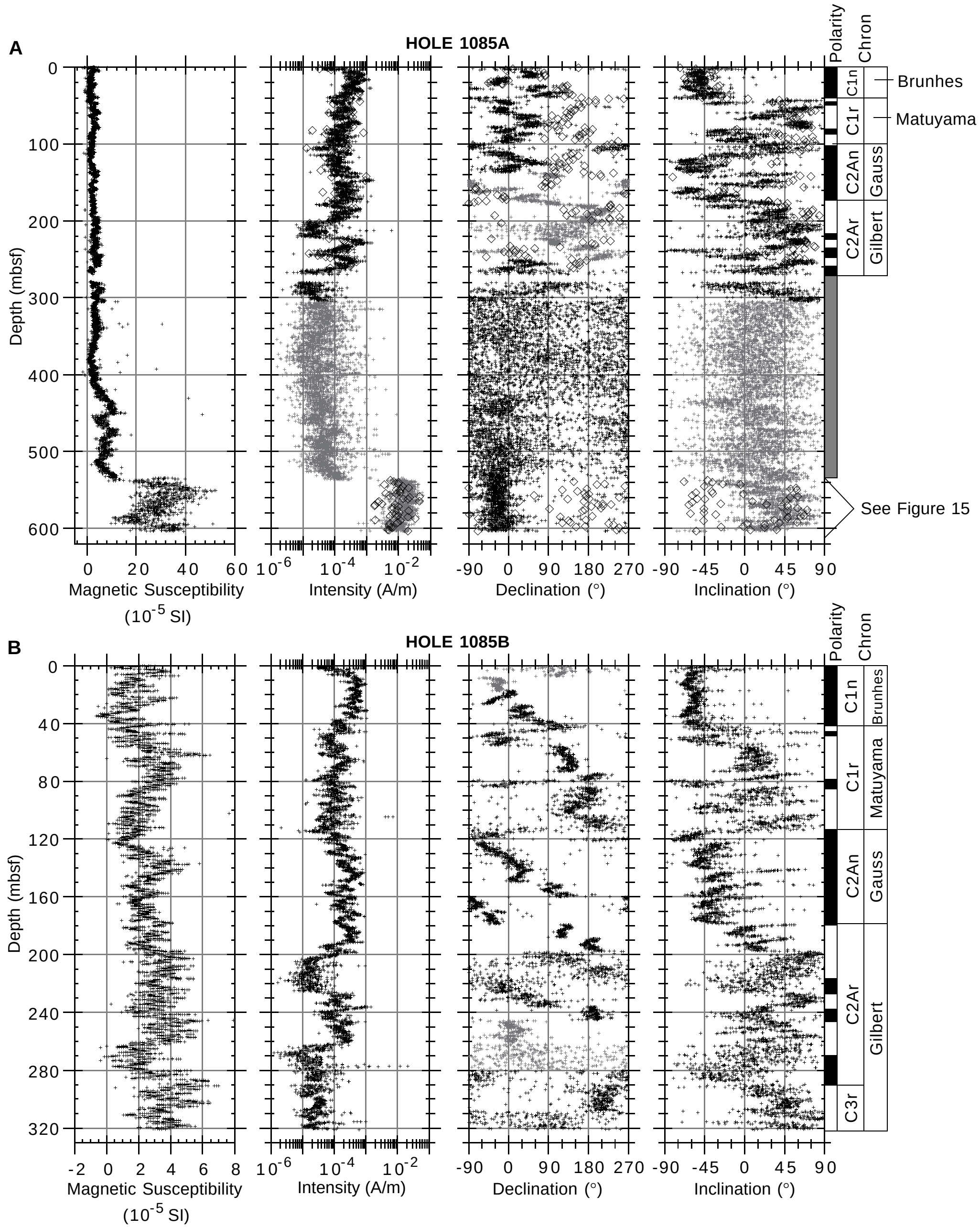

Figure 14. Magnetic susceptibility (SI volume units) and NRM intensity, declination, inclination, and magnetostratigraphic interpretation after 20-mT demagnetization for (**A**) Hole 1085A and (**B**) Hole 1085B. Black symbols = Tensor corrected; gray symbols = uncorrected; open diamonds = discrete samples. Polarity shading: black = normal, white = reversed, and gray = ambiguous.

and 4-cm (Hole 1085A [below 100 mbsf] and Hole 1085B) intervals. The correlation of features present in the physical and visual properties measurements of adjacent holes were used to demonstrate the completeness of the local stratigraphic sequence drilled and to establish a depth scale in terms of meters composite depth (mcd) for Site 1085. The continuity of the stratigraphic sequence could be demonstrated between 0 and 298 mcd (Fig. 16; Table 8).

At Site 1085, magnetic susceptibility and total spectral reflectance were used to establish the mcd scale. The data sets were extensively processed before being used for correlation. Suspect measurements were eliminated by thresholding the data. The resulting data were smoothed using a Gaussian filter with a length of 31 cm. All data shown in Figures 16 and 17 were processed as described above.

A stratigraphic correlation using two holes cannot be completely constrained. Depth intervals for which the correlation is not well constrained are at 60, 78–80, 131–133, and 163 mcd. A gap in the composite section, however, does not appear to exist. With a length of 298 mcd, Site 1085 contains the longest composite record of ODP Leg 175.

The spliced record presented in Figure 17 is continuous to 298 mcd for magnetic susceptibility and total color reflectance (Table 9). The selection of cores to be included in the spliced record and the placement of tie points were carried out mainly using magnetic susceptibility.

The growth of the mcd scale compared with the standard ODP msbf scale is ~10 (Core 175-1085B-31H at 307 mcd and 279 mbsf).

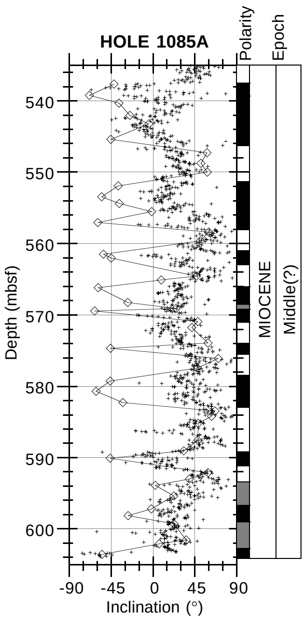

Figure 15. Inclination data and magnetostratigraphic interpretation, after 20-mT demagnetization, from half-core measurements and discrete samples from 535 to 605 mbsf at Hole 1085A. Black symbols = half-core measurements with no Tensor correction; open diamonds = discrete samples. Polarity shading: black = normal, white = reversed, and gray = ambiguous.

In the depth interval from 150 to 180 mbsf (167–193 mcd) the offsets decrease by ~3 m (Fig. 18). This is observed at Holes 1085A and 1085B. In both holes, four successive cores (175-1085A-17H through 20H, and 175-1085B-17H through 20H) overlap by as much as 1 m.

INORGANIC GEOCHEMISTRY

Thirty interstitial water samples were gathered from Hole 1085A between 1.4 and 598.75 mbsf. Whole-round samples were taken at a frequency of one per core to 103.1 mbsf and every third core thereafter to total depth (Table 10). The interstitial water chemistry at this site is dominantly controlled by the high carbonate and low organic carbon concentrations in the sediment, which results in very modest

Table 7. Magnetostratigraphic interpretations for Site 1085.

Polarity chron	Age (Ma)	Depth (mbsf) Hole 1085A	Hole 1085B	Polarity epoch
C1n/C1r.1r	0.78	40	42	Brunhes/Matuyama
C1r.1n	0.99-1.07	~47	48-53	Jaramillo
C2n	1.77-1.95	80-90	78-85	Olduvai
C2An.1n (top)	2.58	113	114	Gauss
C2Ar (top)	3.58	174	178	Gilbert
C3n.1n	4.18-4.29	~220	217-227	Cochiti
C3n.2n	4.48-4.62	235-245	238-247	Nunivak
C3n.3n-4n	4.80-5.23	265-280	270-290	Sidufjall-Thvera

Note: Time scale used is that of Berggren et al. (1995).

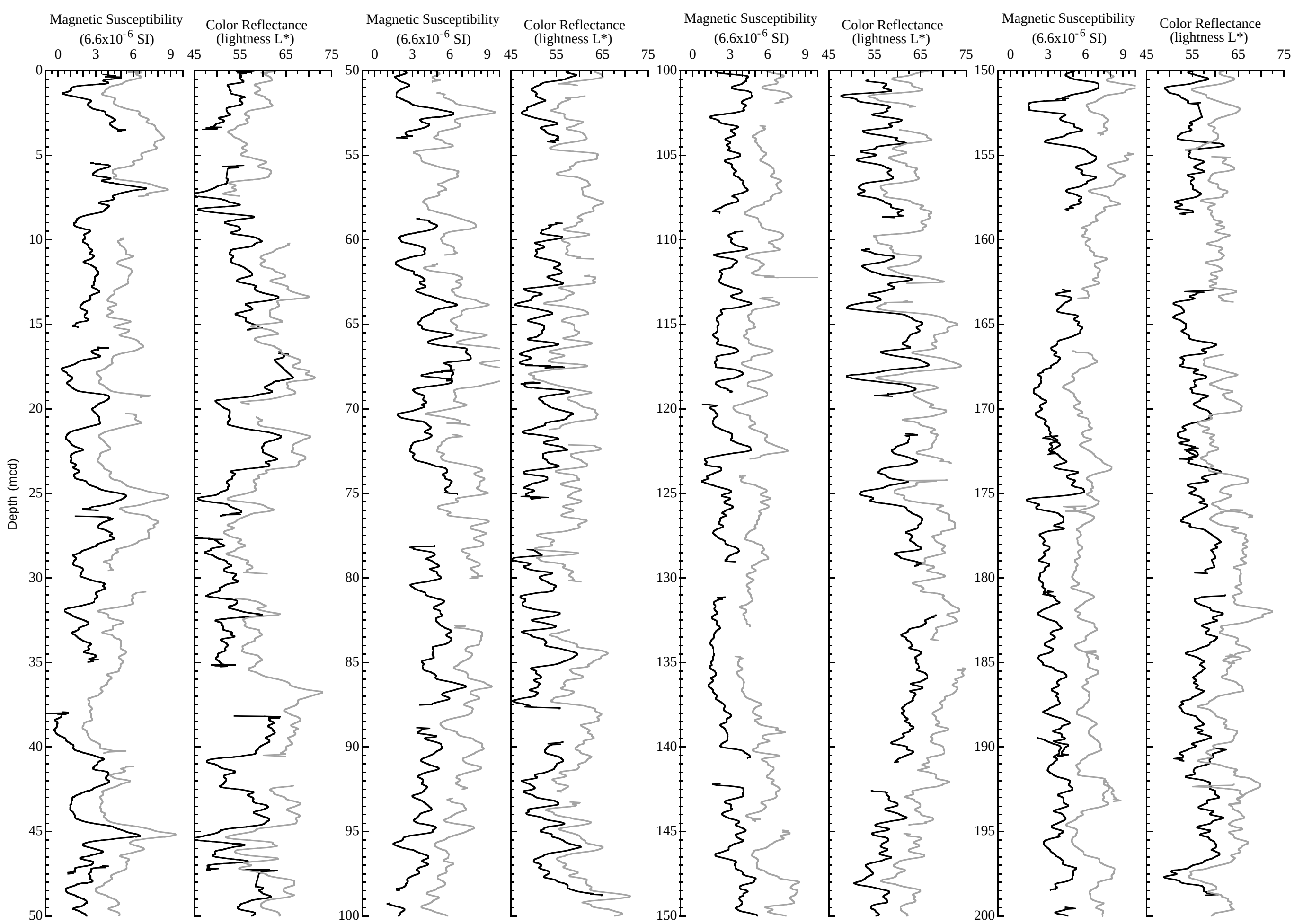

Figure 16. Composite section for Site 1085. Magnetic susceptibility and total color reflectance (lightness L*) are plotted for Holes 1085A (black line) and 1085B (gray line). The downhole logs are shown in meters composite depth (mcd). Offsets have been applied for clarity. (Continued next page.)

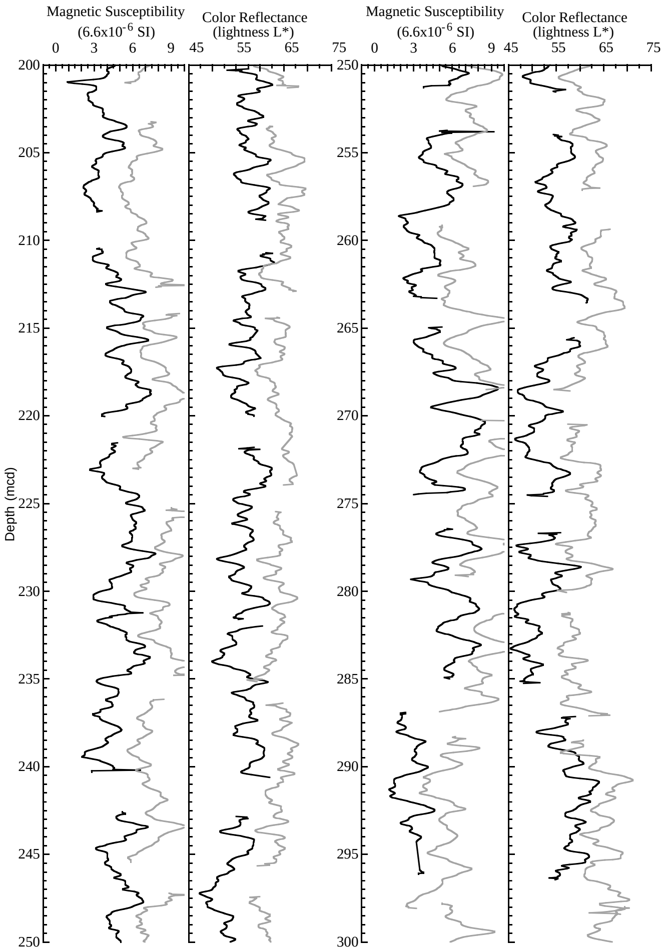

Figure 16 (continued).

variations in chemical gradients of many dissolved species. Also, between 300 and 350 mbsf within lithostratigraphic Subunit IB, several chemical distributions record a marked change in concentration, which corresponds with the transition from APC to XCB coring and, therefore, with a change in the physical nature of the sediment. The species that are most affected by this change appear to be those most involved with clay (re-)mineralization processes.

Alkalinity, Sulfate, and Ammonium

Downcore profiles of alkalinity, sulfate, and ammonium (Fig. 19) through the upper 50 mbsf reflect the degradation of organic matter that is present in low concentrations. Alkalinity reaches a maximum value of only 27 mM at 46 mbsf, remains at similar values to 84 mbsf, and subsequently decreases to the bottom of the hole. The deepest value of 1.752 mM is by far the lowest alkalinity value (except for near-surface data) observed so far during Leg 175 and may largely reflect the consumption of alkalinity during clay mineral formation ("reverse weathering"). Sulfate is completely consumed by 65 mbsf, which is relatively deep in comparison with previous Leg 175 sites. This shallow gradient reflects both the low levels of organic carbon (see "Organic Geochemistry" section, this chapter) as well as the low sedimentation rate (see "Biostratigraphy and Sedimentation Rates" section, this chapter).

Ammonium reaches a maximum of only ~6000 µM at 188.6 mbsf before decreasing to the bottom of the hole. The increase in dissolved ammonium at ~300 mbsf is also observed in other dissolved species, most notably dissolved Mg^{2+}, and is analytically real. It is important to note that above and below this change, the rates of decrease in ammonium concentration are nearly the same.

Calcium, Magnesium, and Strontium

The concentration of dissolved Sr^{2+} increases only slightly within the uppermost 30 mbsf from a value near that of average seawater to 116 µM (Fig. 20). This slight and shallow increase suggests that biogenic calcite dissolution is occurring only to a minor extent in the shallowly buried sediments. Through the remainder of the sequence, dissolved Sr^{2+} increases to a maximum of 876 µM, with an increase in the rate of increase occurring at ~400 mbsf. The overall continued increase records the dissolution of biogenic calcite, which releases Sr^{2+} to the interstitial waters. The values of dissolved Sr^{2+} are the highest observed so far during Leg 175, reflecting the high concentrations of biogenic calcium carbonate in the sediment (see "Organic Geochemistry" section, this chapter).

From the seafloor to 50 mbsf, the concentrations of dissolved Ca^{2+} and Mg^{2+} decrease sharply. The decrease in Ca^{2+} through this depth range (7 mM) is significantly less than the decrease in dissolved Mg^{2+} (11 mM). As at previous Leg 175 sites, we attribute the decrease in Ca^{2+} as recording uptake by dolomite or phosphate phases, with the balance of the Mg^{2+} decrease recording uptake by clay phases.

From 50 mbsf to the bottom of the hole, concentrations of dissolved Ca^{2+} increase smoothly, with the exception of the interval from ~250 to 450 mbsf, where there is a notable positive excursion above the general trend of the increase (see shaded portion of Fig. 20). The position of the maximum at ~350 mbsf corresponds well with the stratigraphic top of an interval of high $CaCO_3$ (see "Organic Geochemistry" section, this chapter; and the color measurements portion of the "Lithostratigraphy" section, this chapter).

Through this same general interval there is a very dramatic increase (13 mM) in dissolved Mg^{2+}, the depth of which differs from the increase in ammonium by only one core. We thus consider them as occurring essentially at the same depth. Below this sharp increase, Mg^{2+} concentrations decrease once again smoothly to the bottom of the hole. We are unsure what causes these changes in the ammonium and Mg^{2+} profiles. There is no large-scale lithostratigraphic variation through this depth (see "Lithostratigraphy" section, this chapter); there is no marked change in porosity recorded in the physical properties data set (see "Physical Properties" section, this chapter), and there is no hiatus in sedimentation or any noticeable change in sedimentation rate (see "Biostratigraphy and Sedimentation Rates" section, this chapter). However, this position is where the coring methodology changed from APC to XCB, thus implying that there is a fundamental change in the character of the lithology that has not yet been observed by the shipboard analytical program. The chemical data are most consistent with a decrease with depth in the porosity, permeability, or formation factor of the sediment; such decreases all act in the direction of slowing down rates of removal of dissolved species, increasing concentration gradients, or both. Given that the alkalinity, dissolved Mg^{2+}, and Na^{+} (see below) are the predominant species affected by this phenomenon, it appears that the chemical processes responsible for these pore-water changes involve clay phases.

Silica and Phosphate

Dissolved silica is present in interstitial waters from Site 1085 at concentrations greater than representative bottom-water values (Fig. 21), indicating the dissolution of biogenic opal. Maximum values of dissolved silica are found at ~100 mbsf, which is the depth range recovered by Cores 175-1085A-10H through 13H, which contain high abundances of diatoms (see "Lithostratigraphy" section, this chapter). From this depth to the bottom of the hole, dissolved silica con-

Table 8. Offsets applied to cores from Holes 1085A and 1085B.

Core	Depth (mbsf)	Offset (m)	Composite depth (mcd)
175-1085A-			
1H	0.0	0.18	0.18
2H	3.7	1.69	5.39
3H	13.2	3.11	16.31
4H	22.7	3.61	26.31
5H	32.2	5.69	37.89
6H	41.7	5.27	46.97
7H	51.2	7.51	58.71
8H	60.7	6.96	67.66
9H	70.2	7.84	78.04
10H	79.7	9.12	88.82
11H	89.2	10.00	99.20
12H	98.7	10.76	109.46
13H	108.2	11.48	119.68
14H	117.7	13.40	131.10
15H	127.2	14.90	142.10
16H	136.7	14.90	151.60
17H	146.2	16.49	162.69
18H	155.7	15.87	171.57
19H	165.2	15.53	180.73
20H	174.7	14.69	189.39
21H	184.2	15.23	199.43
22H	193.7	16.71	210.41
23H	203.2	18.31	221.51
24H	212.7	18.63	231.33
25H	222.2	20.34	242.54
26H	231.7	21.98	253.68
27H	241.2	23.70	264.90
28H	250.7	25.68	276.38
29H	260.2	26.66	286.86
31H	279.2	26.66	305.86
32H	288.7	26.66	315.36
33H	298.2	26.66	324.86
34X	305.0	26.66	331.66
35X	314.7	26.66	341.36
36X	324.4	26.66	351.06
37X	334.0	26.66	360.66
38X	343.7	26.66	370.36
39X	353.4	26.66	380.06
40X	363.0	26.66	389.66
41X	372.7	26.66	399.36
42X	382.4	26.66	409.06
43X	392.1	26.66	418.76
44X	401.8	26.66	428.46
45X	411.5	26.66	438.16
46X	421.1	26.66	447.76
47X	430.7	26.66	457.36
48X	440.4	26.66	467.06
49X	450.0	26.66	476.66
50X	459.7	26.66	486.36
51X	468.9	26.66	495.56
52X	478.5	26.66	505.16
53X	488.2	26.66	514.86
54X	497.9	26.66	524.56
55X	507.6	26.66	534.26
56X	517.2	26.66	543.86
57X	526.9	26.66	553.56
58X	536.6	26.66	563.26
59X	546.2	26.66	572.86
60X	555.8	26.66	582.46
61X	565.5	26.66	592.16
62X	575.1	26.66	601.76
63X	584.7	26.66	611.36
64X	594.4	26.66	621.06
175-1085B-			
1H	0.0	0.00	0.00
2H	7.9	1.95	9.85
3H	17.4	2.83	20.23
4H	26.9	3.87	30.77
5H	36.4	4.71	41.11
6H	45.9	5.35	51.25
7H	55.4	5.98	61.38
8H	64.9	6.58	71.48
9H	74.4	8.38	82.78
10H	83.9	9.10	93.00
11H	93.4	9.82	103.22
12H	102.9	10.46	113.36
13H	112.4	11.52	123.92
14H	121.9	12.70	134.60
15H	131.4	13.48	144.88
16H	140.9	13.94	154.84
17H	150.4	16.13	166.53
18H	159.9	15.81	175.71
19H	169.4	14.87	184.27
20H	178.9	13.07	191.97
21H	188.4	14.79	203.19
22H	197.9	16.23	214.13
23H	207.4	17.81	225.21
24H	216.9	19.22	236.12
25H	226.4	20.76	247.16
26H	235.9	23.20	259.10
27H	245.4	24.82	270.22
28H	254.9	26.06	280.96
29H	260.9	27.34	288.24
30H	270.4	27.34	297.74
31H	279.9	27.11	307.01
32H	289.4	27.11	316.51
33H	298.9	27.11	326.01
34H	308.4	27.11	335.51
35H	315.4	27.11	342.51

Note: The offsets transform ODP standard depth values in meters below seafloor (mbsf) to meters composite depth (mcd).

centrations decrease, with several short depth intervals of local increases and decreases. These short intervals do not correspond with any large variation in diatom abundance (see "Biostratigraphy and Sedimentation Rates" section, this chapter), nor do they correspond with variations in clay content (see "Lithostratigraphy" section, this chapter). However, at Site 1085 sponge spicules are more abundant than at previous Leg 175 locations (see "Biostratigraphy and Sedimentation Rates" section, this chapter). We hypothesize that continued shore-based research on the distributions of these spicules will provide relevant information about these dissolved silica distributions.

Because of remineralization of organic matter, dissolved phosphate concentrations increase with depth through Unit IA and reach a maximum value of ~50 µM at 50 mbsf (Fig. 21). Through the remainder of the sequence, dissolved phosphate decreases to extremely low concentrations (<5 µM) reflecting the uptake into diagenetic phases.

Sodium and Potassium

Concentrations of dissolved K^+ are relatively constant through the uppermost 100 mbsf (Fig. 22). Below this depth, dissolved K^+ decreases linearly to very low minimum values at the bottom of the hole, most likely caused by uptake by clay phases. There is no change through the 300 mbsf depth interval where ammonium and alkalinity show much change. Dissolved Na^+ increases rapidly through lithostratigraphic Subunit IA and reaches a maximum value at 250 mbsf. There is a large decrease across the 300-mbsf-depth interval, and the scale of this decrease (~35 mM) is far greater than the increase observed in the ammonium and Mg^+ profiles. After this sharp decrease, dissolved Na^+ concentrations increase toward the bottom of the hole.

Salinity and Chloride

Salinity decreases relatively slightly through the sequence (Fig. 23), recording the total decreases in the species described above, particularly alkalinity, Mg^{2+}, Na^+, and K^+.

Concentrations of dissolved Cl^- record an initial increase to a maximum of ~560 mM at 30 to 40 mbsf before decreasing to the bottom of the hole. This initial increase in dissolved Cl^- may reflect changes in bottom-water chemistry associated with ice-volume variations through glacial periods.

ORGANIC GEOCHEMISTRY

Calcium carbonate and organic carbon concentrations were measured on sediment samples from Hole 1085A (Table 11). Organic matter atomic carbon/nitrogen (C/N) ratios and Rock-Eval analyses were employed to determine the type of organic matter contained within the sediments. Elevated amounts of gas were encountered, and routine monitoring of the sedimentary gases was done for drilling safety.

Inorganic and Organic Carbon Concentrations

Concentrations of carbonate carbon in Site 1085 sediments range between 10.2 and 3.3 wt%, corresponding to 84.8 and 27.8 wt% $CaCO_3$ (Table 11). The carbonate concentrations vary in two ways: (1) closely spaced changes related to light–dark color fluctuations and (2) more gradual downhole increases and decreases (Fig. 24). Sediments at this site are divided into an upper lithostratigraphic unit, which has two subunits, and a lower unit (see "Lithostratigraphy" section, this chapter). Subunit IA, a Pliocene–Holocene nannofossil-foraminifer ooze, averages 69 wt% $CaCO_3$. Subunit IB is a Miocene–Pliocene nannofossil ooze that averages 65 wt% $CaCO_3$. Unit II, a Miocene clay-rich nannofossil ooze, averages 59 wt% $CaCO_3$. The variations in concentrations reflect varying combinations of changes in delivery of calcareous material, dilution by noncalcareous components, and carbonate dissolution.

TOC determinations were done on selected samples from Hole 1085A sediments to estimate the amounts of organic matter in the different lithostratigraphic units (Table 11). Like $CaCO_3$ concentrations, TOC concentrations change in both short-term and longer term patterns (Fig. 25). TOC concentrations are low, averaging 1.42 wt% in lithostratigraphic Subunit IA and 0.66 wt% in Subunit IB. The single TOC determination from Unit II is 0.37 wt%. These TOC concentrations reflect a history of moderate-to-low productivity in this part of the Benguela Current system, which has delivered only modest amounts of organic matter to the sediments, and the low accumulation rate of sediments (see "Biostratigraphy and Sedimentation Rates" section, this chapter), which has not aided preservation of the organic matter.

Organic Matter Source Characterization

Organic C/N ratios were calculated for sediment samples from the different Site 1085 lithostratigraphic subunits using TOC and total nitrogen concentrations (Table 11). For those samples having nitrogen concentrations below the limit of reliable measurement (0.05 wt%), C/N values have been excluded. The C/N ratios vary from 17.6 to 3.0 (Fig. 26). Most of these C/N ratios are intermediate between unaltered algal organic matter (5–8) and fresh land-plant material (25–35; e.g., Emerson and Hedges, 1988; Meyers, 1994). The low C/N ratios occur in samples that are poor in organic carbon; these values may be biased by the tendency of clay minerals to absorb ammonium ions generated during the degradation of organic matter (Müller, 1977). The means of the C/N ratios are Subunit IA, 11.6; Subunit IB, 9.5; and Unit II, 10.8. Because of their setting offshore from a coastal desert, it is likely that these sediments contain mostly marine-derived organic matter. The C/N ratios that are higher than fresh algal organic

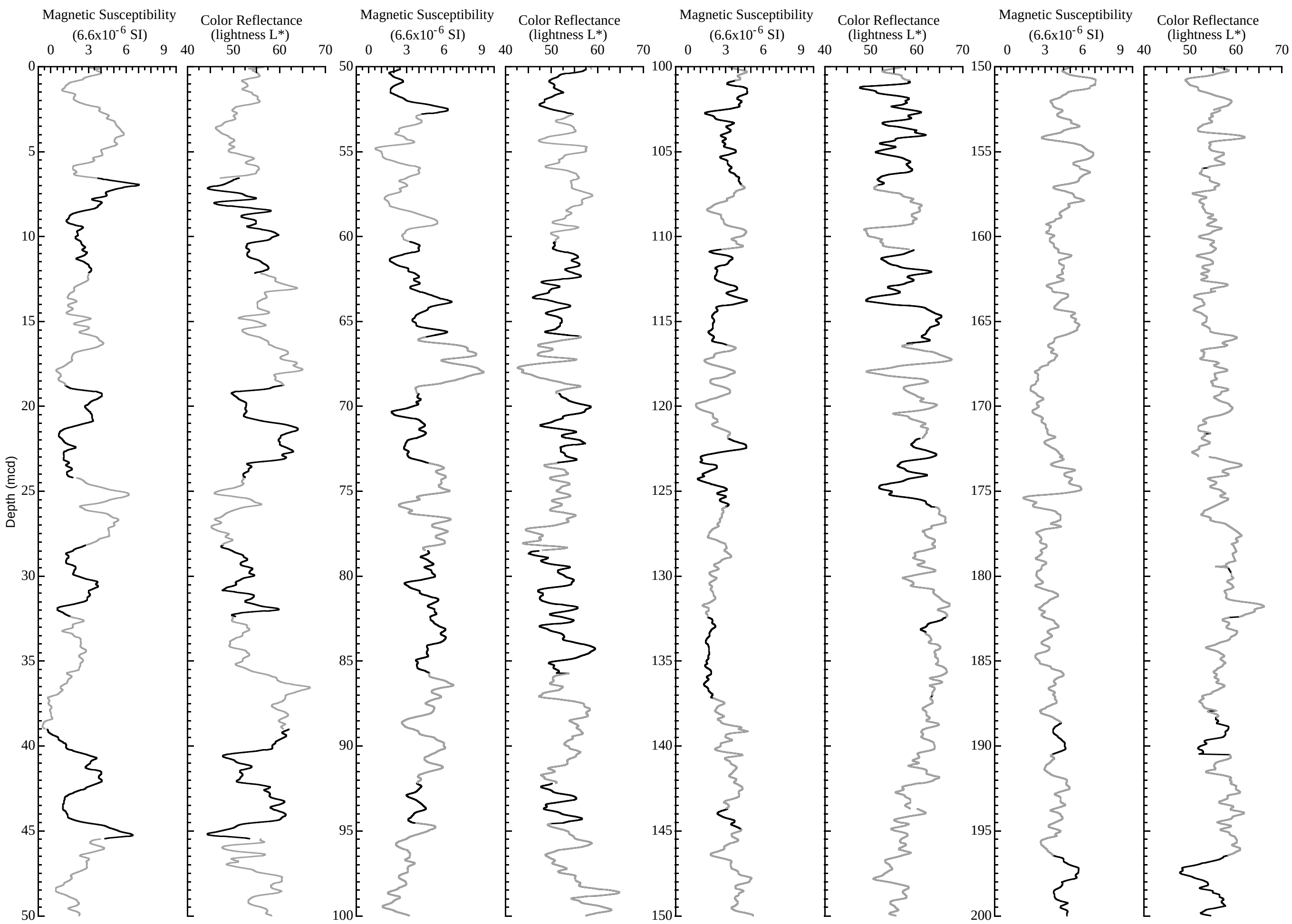

Figure 17. The spliced records for magnetic susceptibility and total color reflectance (lightness L*) are plotted in meters composite depth (mcd). Cores from Holes 1085A and 1085B have been used for the spliced record: black line = Hole 1085A and gray line = Hole 1085B. (Continued next page.)

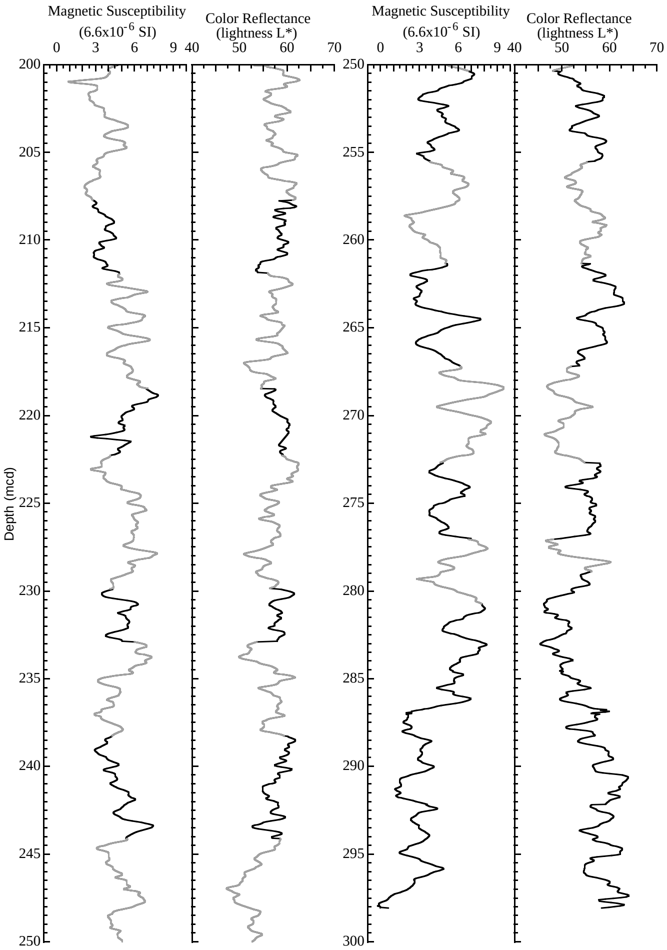

Figure 17 (continued).

matter indicate that preferential loss of nitrogen-rich, proteinaceous matter and consequent elevation of C/N ratios occurred during settling of organic matter to the seafloor.

A Van Krevelen–type plot of the hydrogen index (HI) and oxygen index (OI) values indicates that the sediments contain type II (algal) organic matter (Fig. 27) that has been heavily altered by microbial processing during early diagenesis. Well-preserved type II organic matter has high HI values (Peters, 1986); these values can be lowered by microbial oxidation (Meyers, 1997). In general, Hole 1085A sediments having lower Rock-Eval TOC values also have lower HI values (Fig. 28). This relationship confirms that the marine organic matter has been subject to partial oxidation, which simultaneously lowers TOC and HI values (Meyers, 1997). Further evidence of substantial amounts of in situ organic matter degradation exists in the large decreases in sulfate and increases in alkalinity and ammonia in the interstitial waters of Site 1085 sediments (see "Inorganic Geochemistry" section, this chapter).

The sediment samples have low Rock-Eval T_{max} values (Table 12), showing that their organic matter is thermally immature with respect to petroleum generation (Peters, 1986) and therefore is unlikely to contain much detrital organic matter derived from erosion of thermally mature sedimentary rocks from Africa.

Headspace Gases

Moderately high amounts of methane and CO_2 were found in sediments from Site 1085 (Table 13). The odor of hydrogen sulfide was noted in Cores 175-1085A-2H through 10H (5.2–84 mbsf). Total gas pressures became great enough in sediments below Core 175-1085A-2H (17 mbsf) to require perforating the core liner to relieve the pressure and prevent excessive core expansion.

Methane (C_1) first appears in headspace gas samples of Hole 1085A sediments at 17.7 mbsf. Concentrations become significant in sediments below 46 mbsf (Fig. 29). High C_1/C_2 ratios and the absence of major contributions of higher molecular weight hydrocarbon gases (Table 13) indicate that the gas is biogenic, as opposed to thermogenic, in origin. As at Sites 1081 through 1084, a biogenic origin of the methane is supported by the disappearance of interstitial sulfate at approximately the same sub-bottom depth where methane concentrations begin to rise (see "Inorganic Geochemistry" section, this chapter), inasmuch as Claypool and Kvenvolden (1983) observe that the presence of interstitial sulfate inhibits microbial methanogenesis in marine sediments.

Natural gas analyses determined that the most abundant gas was methane, not CO_2 as at other Leg 175 sites. Headspace concentrations of methane remained high, whereas those of CO_2 gradually diminished with depth in sediments from Hole 1085A (Fig. 30). Cragg et al. (1992) report the existence of viable microbes to depths of ~500 mbsf in the sediments from the Japan Sea. The abundance of biogenic gases deep in sediments from Site 1085 suggests the presence of viable microbial communities to similar sub-bottom depths on the Namibia margin.

PHYSICAL PROPERTIES

Shipboard physical properties measurements were performed on both unsplit and split cores recovered from Site 1085. Measurements with the MST were made of GRAPE density, magnetic susceptibility, and *P*-wave velocity at a high resolution on all recovered whole-round core sections. Natural gamma radiation (NGR) activity was determined on most of all cores at a lower resolution.

Gravimetric wet bulk density, porosity, and moisture content data were collected using samples from one or two points in every section <460 mbsf. Below 539 mbsf, this sampling rate was reduced to one data point for every second section. No samples were collected between 460 and 539 mbsf. Method C was also used at Site 1085 (see "Explanatory Notes" chapter, this volume).

Within all APC sections undrained vane shear strength was determined. No data were collected from the extended core barrel cores at this site.

Compressional (*P*-wave) velocity measurements were made at a resolution of one or two discrete sampling points per section. For discrete *P*-wave velocity measurements, the modified Hamilton Frame was used on split sections of cores to 222 mbsf.

Thermal conductivity was measured on every second unsplit section in every core by inserting a thermal probe into the sediment (see "Explanatory Notes" chapter, this volume).

Multisensor Track

GRAPE density (Fig. 31), *P*-wave velocities (Fig. 32), and magnetic susceptibility (Figs. 33A, 34A) were determined every 2 cm for depths <60 mbsf. MST data are included on CD-ROM (back pocket, this volume). NGR activity was measured every 30 cm. Below Core 175-1085A-8H, the resolution was reduced to 32 cm for the NGR sensor and to 4 cm for all other MST parameters. Compressional velocities were recorded at an amplitude threshold of 50 incremental units. The MST *P*-wave logger recorded signals to depths of 138 mbsf (Fig. 32), which was deeper compared with other Leg 175 sites. This observation may indicate a moderate content of gas in the sediments at Hole 1085A. MST velocity and discrete velocities display a similar trend between 0 and 67 mbsf, but discrete velocities are systematically higher. At 70 mbsf, both data sets merge, but the MST values reveal higher scatter down to 138 mbsf.

Table 9. List of splice tie points used to create the continuous "spliced" stratigraphic sequence for Site 1085.

Hole, core, section, interval (cm)	Depth (mbsf)	Composite depth (mcd)	Whether tied	Hole, core, section, interval (cm)	Depth (mbsf)	Composite depth (mcd)	Offset (m)
1085B-1H-5, 56	6.56	6.56	Tie to	1085A-2H-1, 116.5	4.87	6.56	1.69
1085A-2H-5, 78	10.48	12.17	Tie to	1085B-2H-2, 81	10.22	12.17	1.95
1085B-2H-6, 140	16.80	18.75	Tie to	1085A-3H-2, 94	15.64	18.75	3.11
1085A-3H-6, 38	21.08	24.19	Tie to	1085B-3H-3, 96	21.36	24.19	2.83
1085B-3H-6, 44	25.34	28.17	Tie to	1085A-4H-2, 36	24.56	28.17	3.61
1085A-4H-5, 6	28.76	32.37	Tie to	1085B-4H-2, 9	28.50	32.37	3.87
1085B-4H-6, 72	35.12	38.99	Tie to	1085A-5H-1, 110	33.30	38.99	5.69
1085A-5H-6, 6	39.76	45.45	Tie to	1085B-5H-3, 133	40.74	45.45	4.71
1085B-5H-7, 4	45.44	50.15	Tie to	1085A-6H-3, 18	44.88	50.15	5.27
1085A-6H-4, 134	47.54	52.81	Tie to	1085B-6H-2, 5	47.46	52.81	5.35
1085B-6H-7, 4	54.94	60.29	Tie to	1085A-7H-2, 8	52.78	60.29	7.51
1085A-7H-5, 112	58.32	65.83	Tie to	1085B-7H-3, 145	59.85	65.83	5.98
1085B-7H-6, 36	63.26	69.24	Tie to	1085A-8H-2, 8	62.28	69.24	6.96
1085A-8H-4, 116	66.36	73.32	Tie to	1085B-8H-2, 33	66.74	73.32	6.58
1085B-8H-5, 100	71.90	78.48	Tie to	1085A-9H-1, 44	70.64	78.48	7.84
1085A-9H-6, 16	77.86	85.70	Tie to	1085B-9H-2, 141	77.32	85.70	8.38
1085B-9H-7, 40	83.80	92.18	Tie to	1085A-10H-3, 36	83.06	92.18	9.12
1085A-10H-4, 120	85.40	94.52	Tie to	1085B-10H-2, 1	85.42	94.52	9.10
1085B-10H-6, 32	91.72	100.82	Tie to	1085A-11H-2, 12	90.82	100.82	10.00
1085A-11H-6, 24	96.94	106.94	Tie to	1085B-11H-3, 72	97.12	106.94	9.82
1085B-11H-6, 4	100.94	110.76	Tie to	1085A-12H-1, 129	100.00	110.76	10.76
1085A-12H-5, 84	105.54	116.30	Tie to	1085B-12H-2, 144	105.84	116.30	10.46
1085B-12H-6, 100	111.40	121.86	Tie to	1085A-13H-2, 68	110.38	121.86	11.48
1085A-13H-5, 24	114.44	125.92	Tie to	1085B-13H-2, 49	114.40	125.92	11.52
1085B-13H-6, 96	120.86	132.38	Tie to	1085A-14H-1, 128	118.98	132.38	13.40
1085A-14H-5, 4	123.74	137.14	Tie to	1085B-14H-2, 104	124.44	137.14	12.70
1085B-14H-7, 8	130.98	143.68	Tie to	1085A-15H-2, 5	128.78	143.68	14.90
1085A-15H-6, 144	136.16	151.06	Tie to	1085B-15H-5, 17	137.58	151.06	13.48
1085B-15H-6, 16	139.06	152.54	Tie to	1085A-16H-1, 93	137.64	152.54	14.90
1085A-16H-3, 136	141.06	155.96	Tie to	1085B-16H-1, 112	142.02	155.96	13.94
1085B-16H-7, 76	149.25	163.19	Tie to	1085A-17H-2, 28	146.70	163.19	16.49
1085A-17H-7, 120	155.12	171.61	Tie to	1085B-17H-4, 57	155.48	171.61	16.13
1085B-17H-5, 40	156.80	172.93	Tie to	1085A-18H-1, 136	157.06	172.93	15.87
1085A-18H-6, 76	163.96	179.83	Tie to	1085B-18H-3, 112	164.02	179.83	15.81
1085B-18H-5, 68	166.58	182.39	Tie to	1085A-19H-2, 16	166.86	182.39	15.53
1085A-19H-5, 120	172.40	187.93	Tie to	1085B-19H-3, 65	173.06	187.93	14.87
1085B-19H-5, 20	175.60	190.47	Tie to	1085A-20H-1, 108	175.78	190.47	14.69
1085A-20H-5, 104	181.74	196.43	Tie to	1085B-20H-3, 146	183.36	196.43	13.07
1085B-20H-6, 56	186.96	200.03	Tie to	1085A-21H-1, 60	184.80	200.03	15.23
1085A-21H-6, 80	192.50	207.73	Tie to	1085B-21H-4, 4	192.94	207.73	14.79
1085B-21H-6, 116	197.06	211.85	Tie to	1085A-22H-1, 144	195.14	211.85	16.71
1085A-22H-6, 56	201.76	218.47	Tie to	1085B-22H-3, 133	202.24	218.47	16.23
1085B-22H-6, 60	206.00	222.23	Tie to	1085A-23H-1, 70.1	203.92	222.23	18.31
1085A-23H-6, 88	211.58	229.89	Tie to	1085B-23H-4, 16.9	212.08	229.89	17.81
1085B-23H-6, 16	215.06	232.87	Tie to	1085A-24H-2, 4	214.24	232.87	18.63
1085A-24H-5, 76	219.63	238.26	Tie to	1085B-24H-2, 64	219.04	238.26	19.22
1085B-24H-6, 48	224.88	244.10	Tie to	1085A-25H-2, 5	223.76	244.10	20.34
1085A-25H-6, 32	230.02	250.36	Tie to	1085B-25H-3, 20	229.60	250.36	20.76
1085B-25H-6, 84	234.74	255.50	Tie to	1085A-26H-2, 32	233.52	255.50	21.98
1085A-26H-7, 4	239.34	261.32	Tie to	1085B-26H-2, 72	238.12	261.32	23.2
1085B-26H-6, 56	243.96	267.16	Tie to	1085A-27H-2, 76	243.46	267.16	23.7
1085A-27H-6, 28	248.98	272.68	Tie to	1085B-27H-2, 96	247.86	272.68	24.82
1085B-27H-5, 80	252.22	277.02	Tie to	1085A-28H-1, 64	251.34	277.02	25.68
1085A-28H-6, 68	258.88	284.56	Tie to	1085B-28H-3, 60	258.50	284.56	26.06
1085B-28H-4, 140	260.80	286.86	Tie to	1085A-29H-1, 0	260.20	286.86	26.66
1085A-29H-4, 80	265.50	292.16	Tie to	1085B-29H-3, 92	264.82	292.16	27.34
1085B-29H-7, 84	270.74	298.08					

Note: The tie points are listed in standard ODP meters below seafloor (mbsf) and meters composite depth (mcd).

Magnetic susceptibility (Figs. 33A, 34A) and GRAPE density (Fig. 31) show a good correlation over the depth range of 540 mbsf. Below 540 mbsf, magnetic susceptibility sharply increases by a factor of 2 to 3. This increase in susceptibility is not associated with a change in wet bulk density values. NGR seems to be best correlated with magnetic susceptibility. The sharp increase in magnetic susceptibility below 540 mbsf is probably caused by a higher proportion of magnetic particles.

GRAPE density and discrete wet bulk density display a high degree of similarity, with some exceptions where data might be erroneous.

Velocities

Discrete velocities decrease within the upper 5 m from 1660 m/s to 1560 m/s (Fig. 32). Between 22 and 28 mbsf, a high-velocity zone is observed with maximum velocities of 1700 m/s. A second peak interval can be identified between 37 and 39 mbsf. Density and velocity profiles do not correlate between 0 and 222 mbsf (Figs. 31A, 32). Because of the low gas content observed at Hole 1085A (see "Organic Geochemistry" section, this chapter), velocity data are considered to be more reliable than those at previous Leg 175 sites, where higher gas content compromised the quality of the *P*-wave velocity measurements.

Index Properties

Data from discrete measurements of wet bulk density, porosity, and moisture content are displayed in Figures 35A, 35B, and 35C, respectively (also see Table 14 on CD-ROM, back pocket, this volume). The density values vary between 1500 and 1950 kg/m^3.

The trend of the wet bulk density profile represents an overall increase in values from 0 to 600 mbsf, which is probably related mostly to compaction. The sediments consist mainly of carbonate-rich oozes, which change into a more clay-rich sediment facies, as imaged by the overall variation of wet bulk density and the lithostratigraphic boundaries (see "Lithostratigraphy" section, this chapter). In general, porosity and moisture profiles are inversely correlated with wet bulk

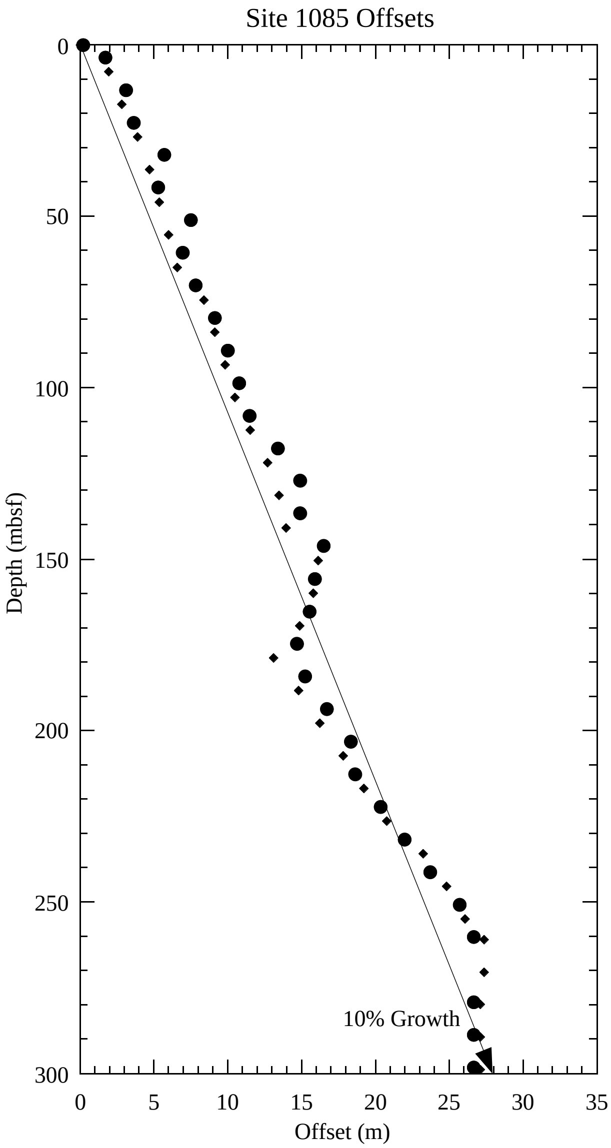

Figure 18. Cores offsets applied to Site 1085 plotted against standard ODP meters below seafloor (mbsf). A linear 10% growth of meters composite depth (mcd) compared with mbsf is indicated by an arrow. Offsets are plotted for Holes 1085A (circles) and 1085B (diamonds).

density. Porosities decrease from 70% in the top section to 40% at 600 mbsf, indicating the high carbonate content of the sediments (Fig. 35B). Moisture content varies between 95% at the top of Hole 1085A and 26% at 600 mbsf (Fig. 35C). Local extreme values correspond to observed and identified lithostratigraphic units (see “Lithostratigraphy” section, this chapter).

Thermal Conductivity and Geothermal Gradient

The thermal conductivity profile (Figs. 33B, 34B) at Hole 1085A was measured in every second core section (see “Explanatory Notes” chapter, this volume). Values range between 0.8 and 1.15 W/(m·K), and thus were higher compared with any data from previous Leg 175 sites, where values typically varied between 0.75 and 0.9 W/(m·K). Below 300 mbsf at Site 1085, it was sometimes difficult to establish direct contact between the thermal probe and the sediments inside the core liners. Thermal conductivity and undrained vane shear reveal some similarity between 0 and 230 mbsf. The thermal conductivity profile is similar to wet bulk and GRAPE density profiles over longer depth intervals at Hole 1085A (Fig. 31).

In Hole 1085A, the Adara tool was deployed to measure formation temperature. A preliminary analysis provided two data points, which were used to estimate a geothermal gradient of 48°C/km, but further analyses will be required to confirm this result.

Vane Shear Strength

Undrained vane-shear measurements were performed in the bottom part of each core section between 0 and 230 mbsf (Fig. 33D, 34D). Below 230 mbsf, the deformation of the original sediment structure into individual drilling biscuits inhibited the measurements of reliable vane-shear data. The profile at Hole 1085A shows an overall increase in vane shear strength between 0 and 215 mbsf, with a maximum value in shear strength measured at 215 mbsf.

DOWNHOLE LOGGING

Hole 1085A was logged with a full suite of sensors to continuously characterize the sedimentary changes, to correlate the lithostratigraphy to other sites, and to provide data for core-log integration.

Logging Operations

Hole 1085A was logged with four different tool strings. The first tool string (seismostratigraphy) included the NGT, LSS, DIT, and TLT sondes. The second tool string (lithoporosity) included the NGT, neutron porosity, gamma density, and TLT sondes. The third tool string (FMS, 1 pass) included the NGT, inclinometry, and FMS sondes. The fourth tool string (GHMT) included the NGT, magnetic susceptibility, and vertical component magnetometer sondes. The logs were run uphole from 606 mbsf (total depth) to pipe at 60 mbsf; the two first runs were logged to the seafloor. The natural gamma-ray intensity is the only parameter measurable through the pipe, but it should be interpreted only qualitatively in this interval. The pipe was set at 90 mbsf and pulled up to ~60 mbsf during logging for the first three runs and before logging for the fourth run (GHMT). The wireline logging heave compensator was started immediately upon entering the hole.

Data Quality and General Results

Hole 1085A is characterized by an irregular hole diameter size of ~9 to 14 in with numerous large enlargements from the bottom to 150 mbsf (see caliper measurements; Fig. 36). Above this interval, the hole conditions are very degraded and show critical washout zones at the top of the logged interval. The downhole measurements are affected by the poor hole conditions, and, thus, only the measurements that are less sensitive to hole conditions yielded reliable data (resistivity, sonic velocity, gamma-ray intensity, and magnetic susceptibility).

The lithologic succession recovered from Hole 1085A is controlled mainly by changes in the nature and intensity of biogenic production vs. the type and amount of detrital input. It is characterized by small changes in sediment composition and compaction, which should be reflected in the log physical properties measurements. Despite the uniform lithology defined from core observation and smear-slide studies (see “Lithostratigraphy” section, this chapter), the high resolution and sensitivity of downhole measurements allows us to identify numerous sedimentary changes in the logged formation.

Lithostratigraphic Unit II at the very bottom of the hole is characterized by decreasing magnetic susceptibility and increasing resistivity; the other parameters were not measured at this depth. The lower part of lithostratigraphic Subunit IB is marked by a large change in magnetic susceptibility at 535 mbsf, which is also weakly reflected in

Table 10. Interstitial water composition for Hole 1085A.

Core, section, interval (cm)	Depth (mbsf)	pH	Alkalinity (mM)	Salinity	Cl^- (titr) (mM)	Cl^- (IC) (mM)	SO_4^{2-} (mM)	Na^+ (mM)	Mg^{2+} (mM)	Ca^{2+} (mM)	K^+ (mM)	H_4SiO_4 (μM)	NH_4^+ (μM)	PO_4^{3-} (μM)	Sr^{2+} (μM)
175-1085A-															
1H-1, 140-150	1.40	7.14	2.889	35.0	555	543	27.18	476	52.47	10.30	11.10	280	225	7	94
2H-1, 140-150	5.10	7.18	4.439	35.0	554	549	26.49	473	52.84	10.62	11.89	470	645	17	100
2H-3, 140-150	8.10	7.59	6.849	35.0	555	553	23.69	477	50.94	9.47	11.41	490	925	24	102
3H-3, 140-150	17.60	6.85	14.591	35.0	557	550	14.84	480	48.56	5.80	12.24	600	2064	40	106
4H-3, 140-150	27.10	7.11	19.602	34.0	559	550	8.17	484	45.66	4.11	11.51	633	2876	47	116
5H-3, 140-150	36.60	7.42	23.156	34.0	559	553	2.60	481	43.94	3.14	11.73	671	2969	44	138
6H-3, 140-150	46.10	7.02	27.466	34.0	557	551	0.22	486	40.95	2.79	11.16	656	2922	52	166
7H-3, 140-150	55.60	7.49	25.587	33.0	556	561	0.67	491	37.79	2.89	11.01	705	3781	38	186
8H-3, 140-150	65.10	7.58	25.094	33.0	554	551	0.00	487	37.51	2.94	11.58	717	4294	39	192
9H-3, 140-150	74.60	7.21	26.953	32.5	552	543	0.00	490	35.33	3.50	11.55	786	4285	31	204
10H-3, 140-150	84.10	6.52	26.982	32.5	552	543	0.00	492	34.60	3.56	11.06	899	4939	26	217
11H-3, 140-150	93.60	7.09	25.807	32.5	550	541	0.00	489	33.76	4.11	11.03	930	4444	23	224
12H-3, 140-150	103.10	7.59	25.659	32.0	549	537	0.00	490	32.55	4.13	11.15	937	4873	18	231
15H-3, 140-150	131.62	7.15	24.833	32.0	549	544	0.00	488	32.22	4.99	11.02	873	5275	21	258
18H-3, 140-150	160.10	7.18	25.037	32.0	549	540	0.00	490	31.31	5.27	10.47	579	5219	17	269
21H-3, 140-150	188.60	7.10	24.333	32.5	548	546	0.00	490	30.80	5.26	9.91	554	5797	12	292
24H-3, 150-160	217.20	7.09	23.920	32.5	548	539	0.00	494	28.62	5.69	9.68	733	5349	10	317
27H-3, 140-150	245.60	7.46	22.466	32.0	548	536	0.19	496	27.29	5.59	8.93	508	5508	6	338
31H-3, 140-150	283.60	7.83	19.110	32.0	548	543	0.00	490	27.67	6.92	8.20	776	5004	5	375
34X-3, 140-150	309.40	7.10	17.619	32.0	546	533	0.00	458	40.63	8.36	7.52	794	4472	5	382
37X-3, 140-150	338.40	6.95	16.649	32.0	545	532	0.00	462	37.51	9.02	6.99	536	5237	4	418
40X-3, 140-150	367.40	7.14	13.741	31.5	545	536	0.23	462	36.27	8.93	6.37	434	4640	4	434
43X-3, 140-150	396.50	7.17	13.154	31.5	543	535	0.00	466	33.33	8.72	5.91	631	4434	4	452
46X-3, 140-150	425.50	7.23	10.359	31.0	543	543	0.00	467	32.12	8.41	5.14	641	3828	4	507
49X-3, 140-150	454.40	7.29	8.262	31.0	542	530	0.00	474	28.72	7.42	4.43	367	3258	3	564
52X-3, 140-150	482.90	7.37	5.360	31.0	539	530	0.08	469	27.93	7.75	3.92	245	2969	3	596
55X-3, 140-150	512.00	7.42	3.737	30.5	540	534	0.00	474	25.37	7.90	3.59	191	2764	3	659
58X-3, 140-150	541.00	7.66	2.317	30.5	539	539	0.00	477	23.15	7.52	2.97	130	2446	3	742
61X-3, 135-150	569.85	7.73	2.058	30.5	539	530	0.00	476	22.75	8.27	2.94	117	2054	3	821
64X-3, 135-150	598.75	7.59	1.752	30.0	538	526	0.00	478	21.27	8.53	2.45	112	1840	3	876

Note: Cl^- (titr) = analyzed by titration and Cl^- (IC) = analyzed by ion chromatography.

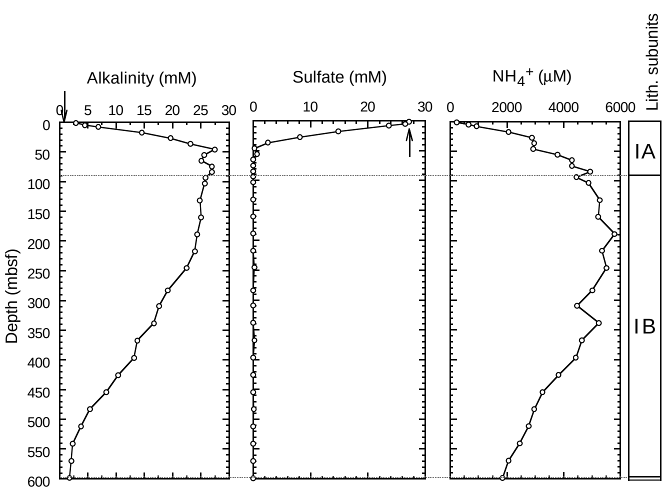

Figure 19. Downcore profiles of dissolved alkalinity, sulfate, and ammonium at Site 1085. Lithostratigraphic subunits shown on right-hand bar, with Unit II too small to indicate. Arrows = mean ocean-bottom-water values taken from Millero and Sohn (1992).

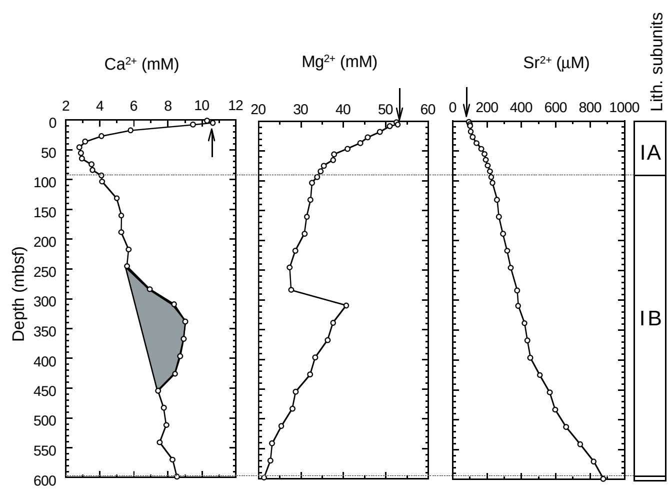

Figure 20. Downcore profiles of Ca^{2+}, Mg^{2+}, and Sr^{2+} at Site 1085. Lithostratigraphic subunits shown on right-hand bar, with Unit II too small to indicate. Shaded region = depth interval of elevated dissolved Ca^{2+} concentrations. Arrows = mean ocean-bottom-water values taken from Millero and Sohn (1992).

the gamma-ray and the resistivity logs. This pronounced magnetic susceptibility feature suggests a possible change in the content of detrital magnetite. An overall regular decrease in gamma-ray intensity, resistivity, and magnetic susceptibility occurs between 430 and 400 mbsf and corresponds to a general increase in carbonate content (see "Organic Geochemistry" section, this chapter). This trend is particularly clear in the 400–360 mbsf interval where the carbonate content reaches a maximum. Exactly the same pattern is observed in the gamma-ray log at 75 mbsf, which approximately corresponds to the boundary between lithostratigraphic Subunits IB and IA.

Besides this general trend, the 480–460, 455–430, and 150–120 mbsf intervals are characterized by high values of gamma-ray intensity, magnetic susceptibility, uranium (U) content, and, occasionally, resistivity. The interval between 455 and 430 mbsf shows an unusual velocity decrease. In contrast, the intervals at 530–510, ~480, ~455, and 280–260 mbsf show a low gamma-ray intensity, magnetic susceptibility, and, occasionally, U content. Uranium correlates with the other parameters when the organic carbon content is high (e. g., between 480 and 420 mbsf; see "Organic Geochemistry" section, this chapter). These intervals probably reflect high-frequency changes in the ratio between clastic and biogenic components.

The temperature tool measures borehole fluid temperature. The results suggest a downhole thermal gradient of 25°C/km, an estimate that is low because of the cooling effect of circulation during drilling.

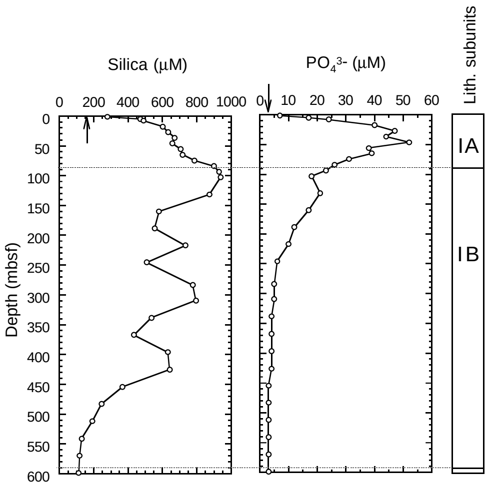

Figure 21. Downcore profiles of dissolved silica and phosphate at Site 1085. Lithostratigraphic subunits shown on right-hand bar, with Unit II too small to indicate. Arrows = mean ocean-bottom-water values taken from Millero and Sohn (1992).

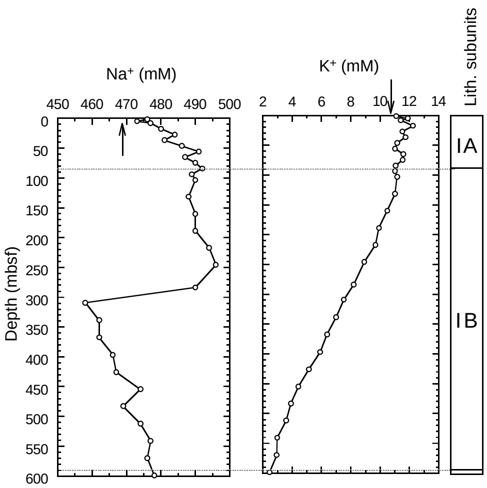

Figure 22. Downcore profiles of dissolved Na^+ and K^+ at Site 1085. Lithostratigraphic subunits shown on right-hand bar, with Unit II too small to indicate. Arrows = mean ocean-bottom-water values taken from Millero and Sohn (1992).

Log-Core Correlations

The core MST and log measurements of natural gamma-ray intensity are very similar. Core data are recorded in counts per second (cps), whereas log data are presented in API (Oil Industry Standard) units. Detailed correlations between the core and log data sets (Fig. 37) appear reliable, with a higher amplitude of the signal in the core. The interval with no recovery between 280 and 265 mbsf corresponds to an interval of low gamma-ray intensity values in the log. Thus, the missing sequence most likely contains carbonate-rich sediments. Log depth is close to core depth at Hole 1085A.

REFERENCES

Berggren, W.A., Kent, D.V., Swisher, C.C., III, and Aubry, M.-P., 1995. A revised Cenozoic geochronology and chronostratigraphy. *In* Berggren, W.A., Kent, D.V., Aubry, M.-P., and Hardenbol, J. (Eds.), *Geochronology, Time Scales and Global Stratigraphic Correlation.* Spec. Publ.—Soc. Econ. Paleontol. Mineral. (Soc. Sediment. Geol.), 54:129–212.

Bleil, U., and Shipboard Scientific Party, 1996. Report and preliminary results of METEOR cruise M34/1, Capetown-Walvis Bay, 3.1.1996–26.1.1996. *Ber. Fachber. Geowiss., Univ. Bremen,* 77.

Bolli, H.M., Ryan, W.B.F., Foresman, J.B., Hottman, W.E., Kagami, H., Longoria, J.F., McKnight, B.K., Melguen, M., Natland, J.H., Proto-Decima, F., and Siesser, W.G., 1978. Cape Basin continental rise: Sites 360 and 361. In Bolli, H.M., Ryan, W.B.F., et al., *Init. Repts. DSDP,* 40: Washington (U.S. Govt. Printing Office), 29–182.

Brown, P.C., Painting, S.J., and Cochrane, K.L., 1991. Estimates of phytoplankton and bacterial biomass and production in the northern and southern Benguela ecosystem. *S. Afr. J. Mar. Sci.,* 11:537–564.

Caulet, J.-P., 1991. Radiolarians from the Kerguelen Plateau, Leg 119. *In* Barron, J., Larsen, B., et al., *Proc. ODP, Sci. Results,* 119: College Station, TX (Ocean Drilling Program), 513–546.

Claypool, G.E., and Kvenvolden, K.A., 1983. Methane and other hydrocarbon gases in marine sediment. *Annu. Rev. Earth Planet. Sci.,* 11:299–327.

Cragg, B.A., Harvey, S.M., Fry, J.C., Herbert, R.A., and Parkes, R.J., 1992. Bacterial biomass and activity in the deep sediment layers of the Japan Sea, Hole 798B. *In* Pisciotto, K.A., Ingle, J.C., Jr., von Breymann, M.T., Barron, J., et al., *Proc. ODP, Sci. Results.,* 127/128 (Pt. 1): College Station, TX (Ocean Drilling Program), 761–776.

Diester-Haass, L., Meyers, P.A., and Rothe, P., 1990. The Benguela Current: glacial/interglacial fluctuations during its Miocene northward migration across the Walvis Ridge. *Paleoceanography,* 5:685-707.

Dingle, R.V., 1995. Continental shelf upwelling and benthic ostracoda in the Benguela System, southeastern Atlantic Ocean. *Mar. Geol.,* 122:207–225.

Dingle, R.V., Birch, G.F., Bremner, J.M., de Decker, R.H., du Plessis, A., Engelbrecht, J.C., Fincham, M.J., Fitton, T., Flemming, B.W., Gentle, R.I., Goodlad, S.W., Martin, A.K., Mills, E.G., Moir, G.J., Parker, R.J., Robson, S.H., Rogers, J., Salmon, D.A., Siesser, W.G., Simpson, E.S.W., Summerhayes, C.P., Westall, C.F., and Winter, A., 1987. Deep-sea sedimentary environments around southern Africa, South-East Atlantic and South-West Indian Oceans. *Ann. S. Afr. Mus.,* 98:1–27.

Emerson, S., and Hedges, J.I., 1988. Processes controlling the organic carbon content of open ocean sediments. *Paleoceanography,* 3:621–634.

Emery, K.O., Uchupi, E., Bowin, C.O., Phillips, J., and Simpson, E.S.W., 1975. Continental margin off western Africa: Cape St. Francis (South Africa to Walvis Ridge (South-West Africa). *AAPG Bull.,* 59:3–59.

Gartner, S., 1977. Calcareous nannofossil biostratigraphy and revised zonation of the Pleistocene. *Mar. Micropaleontol.,* 2:1–25.

Giraudeau, J., 1993. Planktonic foraminiferal assemblages in surface sediments from the southwest African continental margin. *Mar. Geol.,* 110:47–62.

Giraudeau, J., and Rogers, J., 1994. Phytoplankton biomass and sea-surface temperature estimates from sea-bed distribution of nannofossils and planktonic foraminifera in the Benguela Upwelling System. *Micropaleontology,* 40:275–285.

Lutjeharms, J.R.E., 1996. The exchange of water between the South Indian and South Atlantic Ocean. *In* Wefer, G., Berger, W.H., Siedler, G., and Webb, D.J. (Eds.), *The South Atlantic: Present and Past Circulation:* Berlin (Springer-Verlag), 125–162.

Lutjeharms, J.R.E., and Meeuwis, J.M., 1987. The extent and variability of SE Atlantic upwelling. *S. Afr. J. Mar. Sci.,* 5:51–62.

Lutjeharms, J.R.E., and Stockton, P.L., 1987. Kinematics of the upwelling front off southern Africa. *S. Afr. J. Mar. Sci.,* 5:35–49.

Martini, E., 1971. Standard Tertiary and Quaternary calcareous nannoplankton zonation. *In* Farinacci, A. (Ed.), *Proc. 2nd Int. Conf. Planktonic Microfossils Roma:* Rome (Ed. Tecnosci.), 2:739–785.

Melguen, M., 1978. Facies evolution, carbonate dissolution cycles in sediments from the eastern south Atlantic (DSDP Leg 40) since the early Cretaceous. *In* Bolli H.M., Ryan W.B.F., et al., *Init. Repts. DSDP,* 40: Washington (U.S. Govt. Printing Office), 981–1024.

Meyers, P.A., 1994. Preservation of elemental and isotopic source identification of sedimentary organic matter. *Chem. Geol.,* 144:289–302.

————, 1997. Organic geochemical proxies of paleoceanographic, paleolimnologic, and paleoclimatic processes. *Org. Geochem.,* 27:213–250.

Millero, F.J., and Sohn, M.L., 1992. *Chemical Oceanography:* Boca Raton (CRC Press).

Müller, P.J., 1977. C/N ratios in Pacific deep sea sediments: effect of inorganic ammonium and organic nitrogen compounds sorbed by clays. *Geochim. Cosmochim. Acta,* 41:765–776.

Okada, H., and Bukry, D., 1980. Supplementary modification and introduction of code numbers to the low-latitude coccolith biostratigraphic zonation (Bukry, 1973; 1975). *Mar. Micropaleontol.,* 5:321–325.

Peters, K.E., 1986. Guidelines for evaluating petroleum source rock using programmed pyrolysis. *AAPG Bull.,* 70:318–329.

Schulz, H.D., and Shipboard Scientific Party, 1992. Bericht und erste Ergebnisse der METEOR-Fahrt M20/2, Abidjan-Dakar, 27.12.1991–3.2.1992. *Ber. Fachber. Geowiss. Univ. Bremen* 25.

Shannon, L.V., and Nelson, G., 1996. The Benguela: large scale features and processes and system variability. *In* Wefer, G., Berger, W.H., Siedler, G., Webb, D.J. (Eds.), *The South Atlantic: Present and Past Circulation:* Berlin (Springer-Verlag), 163–210.

van Morkhoven, F.P.C.M., Berggren, W.A., and Edwards, A.S., 1986. Cenozoic cosmopolitan deep-water benthic foraminifera. *Bull. Cent. Rech. Explor.—Prod. Elf-Aquitaine,* Mem. 11.

Weaver, P.P.E., 1993. High resolution stratigraphy of marine Quaternary sequences. *In* Hailwood, E.A., and Kidd, R.B. (Eds.), *High Resolution Stratigraphy.* Geol. Soc. Spec. Publ. London, 70:137–153.

Ms 175IR-113

NOTE: Core-description forms (“barrel sheets”) and core photographs can be found in Section 4, beginning on page 581. Forms containing smear-slide data and shore-based log processing data can be found on CD-ROM. See Table of Contents for materials contained on CD-ROM.

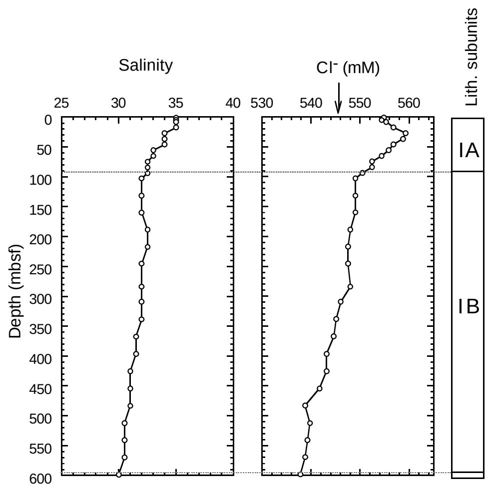

Figure 23. Downcore profiles of salinity and dissolved Cl^- at Site 1085. Lithostratigraphic subunits shown on right-hand bar, with Unit II too small to indicate. Arrow = mean ocean-bottom-water value taken from Millero and Sohn (1992).

Table 11. Percentages of inorganic and total carbon, total nitrogen, and total sulfur in sediment samples from Hole 1085A.

Core, section, interval (cm)	Depth (mbsf)	IC (wt%)	$CaCO_3$ (wt%)	TC (wt%)	TOC (wt%)	TN (wt%)	TS (wt%)	C/N (atomic)
175-1085A-								
Subunit IA - Pliocene-Holocene nannofossil-foramifer ooze								
1H-2, 46-47	1.96	9.25	77.0	10.00	0.77	0.01	0.00	
2H-2, 46-47	5.66	7.71	64.2					
2H-4, 46-47	8.66	8.64	71.9	9.99	1.35	0.12	0.10	13.2
2H-6, 46-47	11.66	9.56	79.7					
3H-2, 46-47	15.16	9.83	81.9					
3H-4, 46-47	18.16	9.78	81.4	10.40	1.77	0.01	0.15	
3H-6, 46-47	21.16	8.77	73.0					
4H-2, 46-47	24.66	8.29	69.1					
4H-4, 46-47	27.66	8.64	72.0	9.90	1.26	0.12	0.22	12.3
4H-6, 46-47	30.66	8.69	72.4					
5H-2, 46-47	34.16	9.70	80.8					
5H-4, 46-47	37.16	9.52	79.3	10.60	0.73	0.01	0.27	
5H-6, 46-47	40.16	8.49	70.7					
6H-2, 46-47	43.66	9.32	77.7					
6H-4, 46-47	46.66	8.34	69.5	10.50	2.14	0.18	0.45	14.3
7H-2, 46-47	53.16	8.42	70.1					
7H-4, 46-47	56.16	6.79	56.6	8.61	1.82	0.16	0.80	12.9
7H-6, 46-47	59.16	6.25	52.1					
8H-2, 46-47	62.66	7.83	65.3					
8H-4, 46-47	65.66	8.30	69.1	9.31	1.01	0.12	0.43	10.3
9H-2, 46-47	72.16	7.47	62.2					
9H-4, 46-47	75.16	6.29	52.4	9.10	2.81	0.22	1.08	14.9
9H-6, 46-47	78.16	7.69	64.1					
10H-2, 46-47	81.66	6.82	56.8					
10H-4, 46-47	84.66	8.09	67.4	8.59	0.50	0.16	0.84	3.7
10H-6, 46-47	87.66	8.38	69.8					
Subunit IB - Miocene-Pliocene nannofossil ooze								
11H-2, 46-47	91.16	8.05	67.1					
11H-4, 46-47	94.16	8.41	70.1	9.16	0.75	0.10	0.26	8.8
11H-6, 46-47	97.16	7.63	63.6					
12H-2, 46-47	100.66	8.27	68.9					
12H-4, 46-47	103.66	9.09	75.7	9.73	0.64	0.01	0.21	
12H-6, 46-47	106.69	9.06	75.5					
13H-2, 46-47	110.16	8.76	73.0					
13H-4, 46-47	113.16	8.98	74.8	10.67	1.69	0.15	0.35	13.2
13H-6, 46-47	116.16	8.56	71.3					
14H-2, 46-47	119.66	9.35	77.9					
14H-4, 46-47	122.66	9.53	79.4	10.17	0.64	0.01	0.41	
14H-6, 46-47	125.66	8.71	72.5					
15H-2, 46-47	129.18	9.05	75.4					
15H-4, 46-47	132.18	8.30	69.1	9.46-1.16	0.11	12.3		0.35
15H-6, 46-47	135.18	7.72	64.3					
16H-2, 46-47	138.66	7.22	60.2					
16H-4, 46-47	141.66	7.45	62.1	8.09	0.64	0.11	1.02	6.8
17H-2, 46-47	146.88	8.78	73.1					
17H-4, 46-47	149.88	8.80	73.3	10.04	1.24	0.12	0.22	12.1
17H-6, 46-47	152.88	9.02	75.1					
18H-2, 46-47	157.66	8.43	70.2					
18H-4, 46-47	160.66	8.23	68.5	9.25	1.02	0.12	0.48	9.9
18H-6, 46-47	163.66	9.00	74.9					
19H-2, 46-47	167.16	8.26	68.8					
19H-4, 46-47	170.16	8.25	68.7	9.47	1.22	0.11	0.67	13.0
19H-6, 46-47	173.16	8.16	67.9					
20H-2, 46-47	176.66	8.62	71.8					
20H-4, 46-47	179.66	8.89	74.1	9.94	1.05	0.01	0.29	
20H-6, 46-47	182.66	7.72	64.3					
21H-2, 46-47	186.16	8.28	68.9					
21H-4, 46-47	189.16	7.67	63.9	8.58	0.91	0.10	1.08	10.6
21H-6, 46-47	192.16	9.37	78.1					
22H-2, 46-47	195.66	8.00	66.7					
22H-4, 46-47	198.66	8.36	69.6	9.01	0.65	0.01	0.63	
22H-6, 46-47	201.66	6.98	58.1					
23H-2, 46-47	205.16	8.79	73.2					
23H-4, 46-47	208.16	7.84	65.3	8.49	0.64	0.01	0.32	
23H-6, 46-47	211.16	8.45	70.4					
24H-2, 46-47	214.66	7.06	58.9					
24H-4, 46-47	217.76	8.34	69.5	8.98	0.64	0.01	0.24	
24H-6, 46-47	220.83	8.24	68.7					
25H-2, 46-47	224.16	9.09	75.7					
25H-4, 46-47	227.16	7.56	62.9	8.82	1.26	0.12	0.64	12.3
25H-6, 46-47	230.16	7.28	60.7					
26H-2, 46-47	233.66	8.65	72.0					
26H-4, 46-47	236.66	9.36	78.0	9.86	0.50	0.01	0.16	
26H-6, 46-47	238.26	8.72	72.6					
27H-2, 46-47	243.16	7.88	65.7					
27H-4, 46-47	246.16	7.92	66.0	8.73	0.81	0.01	0.75	
27H-6, 46-47	249.16	8.62	71.8					
28H-2, 46-47	252.66	8.72	72.6					
28H-4, 46-47	255.66	7.45	62.1	8.83	1.38	0.14	0.72	11.5
28H-6, 46-47	258.66	8.36	69.7					
29H-2, 46-47	262.16	9.11	75.9					
29H-4, 46-47	265.16	9.97	83.1	10.23	0.26	0.01	0.13	
29H-6, 46-47	268.16	9.85	82.1					
31H-2, 46-47	281.16	8.17	68.0					
31H-4, 46-47	284.16	8.88	73.9	9.24	0.36	0.01	0.30	
31H-6, 46-47	287.16	7.39	61.6					
32H-2, 46-47	290.66	8.10	67.5					
32H-4, 46-47	293.66	8.15	67.9	8.85	0.70	0.01	0.16	
32H-6, 46-47	296.31	7.45	62.1					
33H-2, 46-47	300.16	8.97	74.7					
33H-4, 46-47	303.16	6.71	55.9	7.16	0.45	0.01	0.18	
34X-2, 46-47	306.96	8.83	73.5					
34X-4, 46-47	309.96	8.69	72.4	9.48	0.78	0.09	0.00	10.1
34X-6, 46-47	312.96	8.24	68.7					
35X-2, 46-47	315.76	8.59	71.6					
35X-4, 46-47	318.76	7.47	62.2	7.67	0.20	0.01	0.43	
35X-6, 46-47	321.76	7.73	64.4					
36X-2, 46-47	326.36	8.54	71.1					
36X-4, 46-47	329.36	6.73	56.1	7.36	0.63	0.11	0.35	6.7
36X-6, 46-47	332.36	8.48	70.6					
37X-2, 46-47	335.96	8.74	72.8					
37X-4, 46-47	338.96	8.80	73.3	9.40	0.59	0.08	0.08	8.6
37X-6, 46-47	341.96	7.90	65.8					
38X-2, 46-47	345.66	7.75	64.5					
38X-4, 46-47	348.66	7.39	61.6	8.13	0.74	0.09	0.42	9.6
38X-6, 46-47	351.66	8.76	73.0					
39X-2, 46-47	355.36	8.48	70.7					
39X-4, 46-47	358.36	8.12	67.7	8.59	0.47	0.08	0.24	6.9
39X-6, 46-47	361.36	8.70	72.5					
40X-2, 46-47	364.96	8.18	68.1					
40X-4, 46-47	367.96	9.59	79.9	9.51	0.00	0.06	0.14	0.0
40X-6, 46-47	370.96	8.81	73.4					
41X-2, 46-47	374.66	9.40	78.3					
41X-4, 46-47	377.66	10.18	84.8	10.63	0.45	0.07	0.07	7.5
41X-6, 46-47	380.66	10.01	83.4					
42X-2, 46-47	384.36	9.67	80.5					
42X-4, 46-47	387.36	8.77	73.1	9.34	0.57	0.08	0.27	8.3
42X-6, 46-47	390.36	9.29	77.4					
43X-2, 30-32	393.9	10.14	84.5					
43X-4, 31-33	396.91	9.78	81.4	9.99	0.22	0.07	0.15	3.7
43X-6, 32-33	399.92	9.51	79.2					
44X-2, 46-47	403.76	8.46	70.5					
44X-4, 46-47	406.76	7.86	65.5	8.45	0.59	0.08	0.19	8.6
44X-6, 46-47	409.76	9.09	75.7					
45X-2, 46-47	413.46	8.71	72.6					
45X-4, 46-47	416.46	8.22	68.5	9.43	1.20	0.08	0.21	17.5
45X-6, 46-47	419.46	7.94	66.1					
46X-2, 46-47	423.06	7.29	60.7					
46X-4, 46-47	426.06	6.42	53.5	7.08	0.66	0.09	0.48	8.6
46X-6, 46-47	429.06	5.48	45.6					
47X-2, 46-47	432.66	6.32	52.7					
47X-4, 46-47	435.66	3.33	27.8	4.40	1.07	0.12	0.68	10.4
47X-6, 46-47	438.66	4.02	33.5					
48X-2, 46-47	442.29	9.77	81.4					
48X-4, 46-47	445.29	4.42	36.8	5.27	0.85	0.11	0.20	9.0
48X-6, 46-47	448.29	3.87	32.2					
49X-2, 46-47	451.96	6.02	50.2					
49X-4, 46-47	454.96	7.05	58.8	7.52	0.47	0.07	0.12	7.9
49X-6, 46-47	457.96	8.05	67.1					
50X-2, 46-47	461.66	7.98	66.5					
50X-4, 46-47	464.66	6.53	54.4	7.32	0.79	0.09	0.66	10.3
51X-2, 46-47	470.86	6.17	51.4					
51X-4, 46-47	473.86	4.19	34.9	5.10	0.91	0.12	0.11	8.9
51X-6, 46-47	476.86	4.17	34.7					
52X-2, 46-47	480.46	5.18	43.1					
52X-4, 46-47	483.46	7.61	63.4	8.14	0.53	0.07	0.09	8.9
52X-6, 46-47	486.46	6.55	54.5					
53X-2, 46-47	490.07	7.19	59.9					
53X-4, 46-47	493.07	7.20	60.0	7.70	0.50	0.07	0.06	8.4
53X-6, 46-47	496.07	8.26	68.8					
54X-2, 46-47	499.86	5.96	49.6					
54X-4, 46-47	502.86	6.19	51.6	6.73	0.54	0.08	0.29	7.9
54X-6, 46-47	505.86	7.73	64.4					
55X-1, 46-47	508.06	7.72	64.3					
55X-4, 46-47	512.56	8.39	69.9	8.85	0.45	0.05	0.14	10.5
55X-6, 46-47	515.56	7.58	63.2					
56X-2, 46-47	519.16	7.82	65.2					
56X-4, 43-44	522.13	6.29	52.4	6.79	0.50	0.06	0.06	9.8
56X-6, 46-47	525.16	6.96	58.0					
57X-2, 46-47	528.86	6.17	51.4					
57X-4, 46-47	531.86	5.14	42.8	5.66	0.53	0.07	0.09	8.9
57X-6, 46-47	534.86	7.06	58.8					
58X-2, 46-47	538.56	7.39	61.6					
58X-4, 46-47	541.56	5.97	49.7	6.10	0.13	0.05	0.00	3.0
58X-6, 46-47	544.56	7.87	65.5					
59X-2, 46-47	548.08	7.02	58.5					
59X-4, 46-47	551.08	6.28	52.3	6.18	0.00	0.06	0.00	
59X-6, 46-47	554.08	5.70	47.5					
60X-2, 46-47	557.76	6.92	57.6					
60X-4, 46-47	560.76	5.53	46.1	5.93	0.40	0.05	0.00	9.4
60X-6, 46-47	563.76	5.55	46.3					
61X-2, 46-47	567.46	7.36	61.3					
61X-4, 46-47	570.46	7.52	62.6	7.92	0.39	0.04	0.00	11.4
62X-2, 46-47	577.06	6.93	57.7					
62X-4, 46-47	580.06	7.16	59.6	7.59	0.43	0.04	0.00	12.6

Table 11 (continued).

Core, section, interval (cm)	Depth (mbsf)	IC (wt%)	$CaCO_3$ (wt%)	TC (wt%)	TOC (wt%)	TN (wt%)	TS (wt%)	C/N (atomic)
62X-6, 46-47	583.06	7.41	61.8					
63X-2, 46-47	586.66	8.28	69.0					
63X-4, 46-47	589.66	7.44	62.0	7.74	0.30	0.04	0.00	8.8
63X-6, 46-47	592.66	9.21	76.7					
Unit II - Miocene nannofossil ooze and clay-rich nannofossil ooze								
64X-2, 46-47	596.36	7.76	64.6					
64X-4, 46-47	599.36	5.75	47.9	6.12	0.37	0.04	0.00	10.8
64X-6, 46-47	602.36	7.89	65.7					

Notes: IC = inorganic carbon; $CaCO_3$ = calcium carbonate; TC = total carbon; TOC = total organic carbon; TN = total nitrogen; TS = total sulfur; and C/N = carbon/nitrogen ratio. TOC concentrations are calculated from the difference between IC and TC concentrations. C/N ratios are calculated from TOC and TN concentrations and are given as atom/atom ratios.

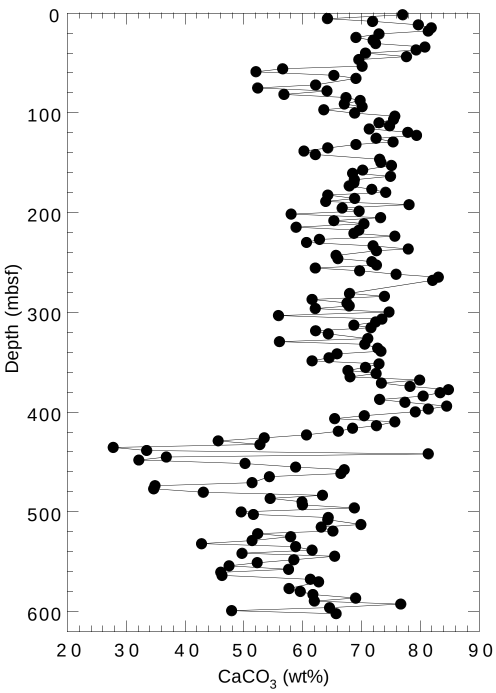

Figure 24. Concentrations of $CaCO_3$ in sediments from Hole 1085A. Variations reflect light–dark color cycles and different lithologic units.

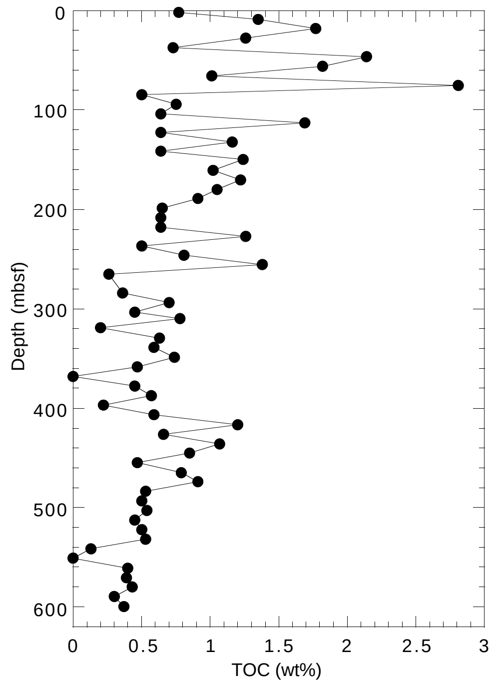

Figure 25. Concentrations of TOC in sediments from Hole 1085A.

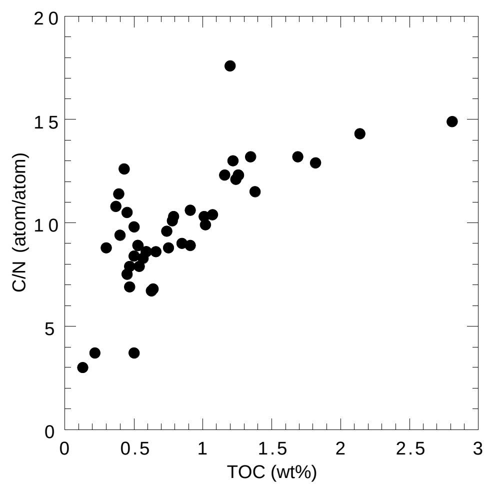

Figure 26. Comparison of organic matter C/N ratios and TOC concentrations of sediments from Hole 1085A. The correspondence between increases in both parameters indicates that preservation of marine organic matter during early diagenesis is important to enhancing the organic carbon richness of sediments on the Walvis Ridge.

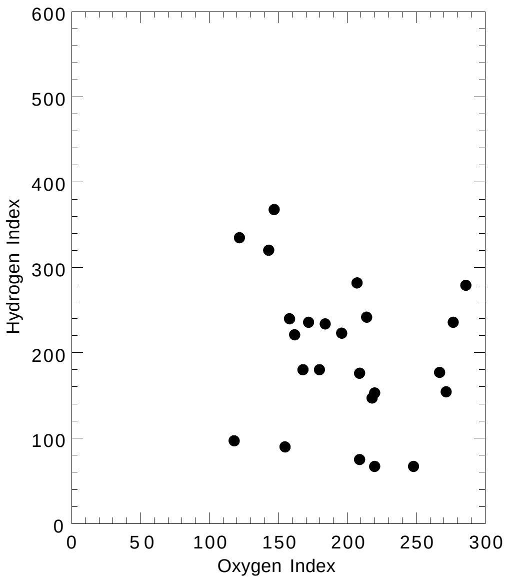

Figure 27. Rock-Eval Van Krevelen–type diagram of sediments from Hole 1085A. Organic matter appears to be type II algal material that has been variably oxidized. HI = milligrams of hydrocarbons per gram of organic carbon; OI = milligrams of CO_2 per gram of organic carbon.

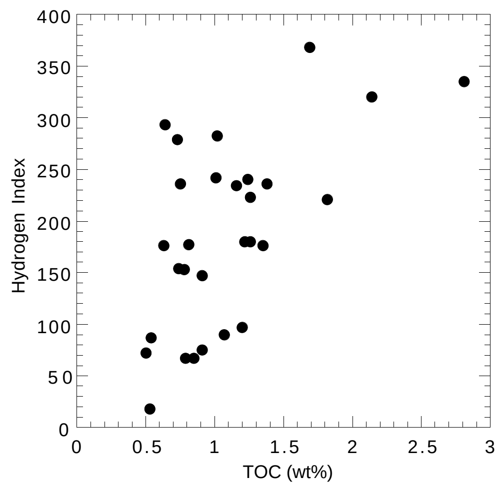

Figure 28. Comparison of Rock-Eval HI values and TOC concentrations of sediments from Hole 1085A. The correspondence between increases in both parameters indicates that preservation of marine organic matter is important to enhancing the organic carbon richness of sediments on the Walvis Ridge.

Table 12. Results of Rock-Eval pyrolysis analyses of sediments from Hole 1085A.

Core, section, interval (cm)	Depth (mbsf)	TOC (wt%)	S_1	S_2	S_3	T_{max} (°C)	HI	OI
175-1085A-								
2H-4, 46-47	8.66	1.35	0.20	2.38	2.83	415	176	209
4H-4, 46-47	27.66	1.26	0.29	2.81	2.47	416	223	196
5H-4, 46-47	37.16	0.73	0.18	2.04	2.09	416	279	286
6H-4, 46-47	46.66	2.14	0.46	6.85	3.08	414	320	143
7H-4, 46-47	56.16	1.82	0.34	4.04	2.96	416	221	162
8H-4, 46-47	65.66	1.01	0.19	2.45	2.17	415	242	214
9H-4, 46-47	75.16	2.81	0.63	9.43	3.45	416	335	122
11H-4, 46-47	94.16	0.75	0.23	1.77	2.08	407	236	277
13H-4, 46-47	113.16	1.69	0.39	6.23	2.50	412	368	147
15H-4, 46-47	132.18	1.16	0.26	2.72	2.14	404	234	184
16H-4, 46-47	141.66	0.64	0.16	1.88	2.30	410	293	359
17H-4, 46-47	149.88	1.24	0.24	2.98	1.96	412	240	158
18H-4, 46-47	160.66	1.02	0.21	2.88	2.12	415	282	207
19H-4, 46-47	170.16	1.22	0.21	2.20	2.05	411	180	168
21H-4, 46-47	189.16	0.91	0.15	1.34	1.99	404	147	218
25H-4, 46-47	227.16	1.26	0.22	2.27	2.27	406	180	180
27H-4, 46-47	246.16	0.81	0.34	1.44	2.17	396	177	267
28H-4, 46-47	255.66	1.38	0.30	3.26	2.38	415	236	172
34X-4, 46-47	309.96	0.78	0.18	1.20	1.72	397	153	220
36X-4, 46-47	329.36	0.63	0.20	1.11	2.15	387	176	341
38X-4, 46-47	348.66	0.74	0.23	1.14	2.02	400	154	272
45X-4, 46-47	416.46	1.20	0.16	1.17	1.42	410	97	118
47X-4, 46-47	435.66	1.07	0.18	0.97	1.66	390	90	155
48X-4, 46-47	445.29	0.85	0.19	0.57	2.11	385	67	248
50X-4, 46-47	464.66	0.79	0.16	0.53	1.74	381	67	220
51X-4, 46-47	473.86	0.91	0.36	0.69	1.91	382	75	209
53X-4, 46-47	493.07	0.50	0.17	0.36	1.52	379	72	304
54X-4, 46-47	502.86	0.54	0.28	0.47	2.09	376	87	387
57X-4, 46-47	531.86	0.53	0.06	0.10	1.62	363	18	305

Notes: TOC = total organic carbon; HI = hydrogen index; and OI = oxygen index. Units of the various Rock-Eval parameters are given in the "Organic Geochemistry" section of the "Explanatory Notes" chapter (this volume).

Table 13. Results of headspace gas analyses of sediments from Hole 1085A.

Core, section, interval (cm)	Depth (mbsf)	C_1 (ppmv)	CO_2 (ppmv)	C_2= (ppmv)	C_2 (ppmv)	C_3= (ppmv)	C_3 (ppmv)	C_1/C_2
175-1085A-								
1H-2, 0-5	1.50	7	2,392					
2H-2, 0-5	5.20	7	4,628					
2H-4, 0-5	8.20	9	6,672					
3H-4, 0-5	17.70	26	17,784					
4H-4, 0-5	27.20	64	20,016		0.6			107
5H-4, 0-5	36.70	117	23,091	0.2	0.7			167
6H-4, 0-5	46.20	2,764	29,048		1.0			2,764
7H-4, 0-5	55.70	8,582	23,189		1.3			6,602
8H-4, 0-5	65.20	17,790	25,881		1.7			10,465
9H-4, 0-5	74.70	26,232	27,683		2.4		1.1	10,930
10H-4, 0-5	84.20	33,380	34,462	0.2	3.0		1.6	11,127
11H-4, 0-5	93.70	38,038	28,479		2.9		1.3	13,117
12H-4, 0-5	103.20	31,004	28,883	0.2	2.9		1.5	10,691
13H-4, 0-5	112.70	35,653	37,844	0.2	3.0		1.2	11,884
14H-4, 0-5	122.20	36,634	27,943		2.7		1.1	13,568
15H-4, 0-5	131.72	30,948	34,945	0.2	3.0		1.6	10,316
16H-3, 0-5	139.70	19,668	28,157	0.2	2.2		1.4	8,940
17H-5, 0-5	150.92	28,008	32,271	0.2	2.8	0.2	1.5	10,003
18H-4, 0-5	160.20	28,507	34,197	0.2	3.0	0.1	1.7	9,502
19H-7, 85-90	175.05	26,403	33,448	0.3	3.2	0.2	1.9	8,251
20H-7, 28-33	183.78	47,987	46,381	0.5	4.6	0.3	2.5	10,432
21H-4, 0-5	188.70	18,051	34,803	0.2	2.0	0.1	1.2	9,026
22H-7, 66-71	203.36	21,839	32,758	0.3	2.3		1.6	9,495
23H-7, 77-82	212.97	23,319	29,861	0.5	2.5	0.2	1.2	9,328
24H-4, 0-5	217.30	29,346	38,544	0.5	3.3	0.2	1.8	8,893
25H-6, 124-129	230.94	25,679	31,684	0.4	3.0	0.2	1.6	8,560
26H-7, 41-46	239.71	30,927	29,179	0.4	3.1	0.1	1.4	9,976
27H-4, 0-5	245.70	25,054	31,358	0.6	3.2	0.3	1.9	7,829
28H-6, 112-117	259.32	21,537	30,722	0.5	3.6	0.3	2.5	5,983
29H-7, 30-35	269.50	40,072	23,575	0.4	4.9	0.2	3.0	8,178
31H-4, 0-5	283.70	43,091	25,762	0.5	4.3		1.7	10,021
32H-6, 0-5	295.85	40,622	28,930	1.0	4.5	0.5	2.2	9,027
33H-5, 0-5	304.20	47,651	28,031	1.0	6.0		3.6	7,942
34X-4, 0-5	309.50	18,497	15,676	0.2	2.1		1.0	8,808
35X-7, 0-5	322.80	6,342	12,281	0.4	1.3		0.9	4,878
36X-6, 0-5	331.90	15,314	11,073	0.4	2.3		1.5	6,658
37X-4, 0-5	338.50	24,245	14,583	0.4	2.8		1.5	8,659
38X-6, 0-5	351.20	34,696	21,055	0.5	4.1		2.2	8,462
39X-6, 0-5	360.90	39,962	16,362	0.4	3.9		1.6	10,247
40X-4, 0-5	367.50	19,590	12,811	0.2	1.9		0.8	10,311
41X-6, 0-5	380.20	29,843	17,753	0.2	2.9		1.1	10,291
42X-6, 0-5	389.90	28,115	12,426	0.4	3.1		1.5	9,069
43X-4, 0-5	396.60	35,492	17,238	0.2	3.5		1.4	10,141
44X-6, 0-5	409.30	17,471	10,626	0.2	2.2		1.0	7,941
45X-6, 0-5	419.00	25,466	8,499	0.4	2.8		1.1	9,095
46X-4, 0-5	425.60	18,870	6,068	0.2	2.1		0.7	8,986
47X-6, 0-5	438.20	17,118	750	0.6	2.1	0.5	1.1	8,151
48X-6, 0-5	447.83	16,471	4,931	0.3	1.9	0.3	0.9	8,669
49X-4, 0-5	454.50	25,768	5,165	0.4	2.5	0.3	0.9	10,307
50X-5, 0-5	465.70	28,038	4,104	0.7	2.8	0.6	1.0	10,014
51X-5, 0-5	474.90	53,132	1,283	0.6	4.6	0.6	1.5	11,550
52X-4, 0-5	483.00	29,376	1,637	0.4	2.5	0.6	0.9	11,750
53X-5, 0-5	494.11	42,589	766	0.4	3.3	0.7	0.9	12,906
54X-5, 0-5	503.90	34,780	2,566	0.8	2.8	0.6	0.9	12,421
55X-4, 0-5	512.10	49,757	3,466	0.2	3.3	0.6	1.0	15,078
56X-4, 0-5	521.70	33,765	2,080	0.3	2.4	0.5	0.6	14,069
57X-4, 0-5	531.40	19,542	945	0.2	1.3	0.2	0.2	15,032
58X-4, 0-5	541.10	46,725	1,258	0.1	2.5		0.3	18,690
59X-6, 0-5	553.62	7,386	1,288	0.2	0.4	0.1		18,465
60X-6, 0-5	563.30	5,128	1,712	0.2	0.3			17,093
61X-4, 0-5	570.00	24,643	1,256	0.1	1.0			24,643
62X-5, 0-5	581.10	28,461	590		0.8			35,576
63X-6, 0-5	592.20	16,998	1,513		0.4			42,495
64X-4, 0-5	598.90	10,831	1,115		0.3			36,103

Notes: C_1 = methane; CO_2 = carbon dioxide; C_2= = ethene; C_2 = ethane; C_3= = propene; and C_3 = propane. Dominance of C_1 over C_2 indicates that the gases originate from in situ microbial degradation of organic matter.

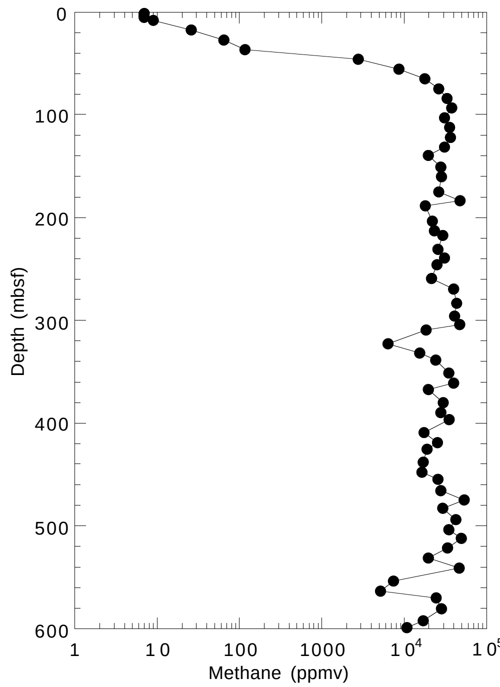

Figure 29. Headspace methane concentrations in sediments from Hole 1085A.

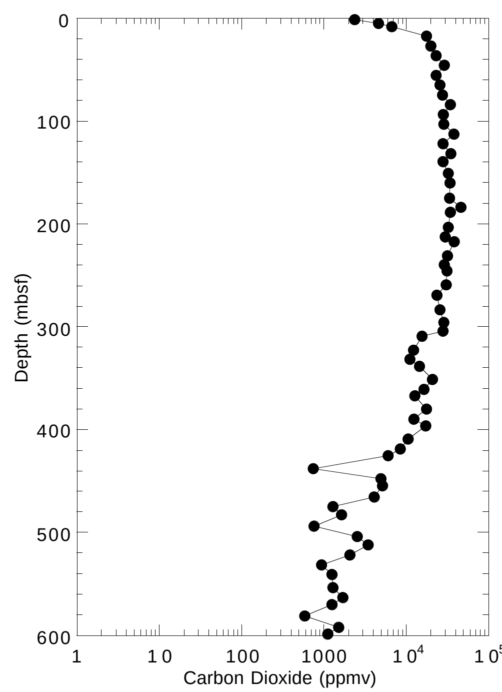

Figure 30. Headspace CO_2 concentrations in sediments from Hole 1085A.

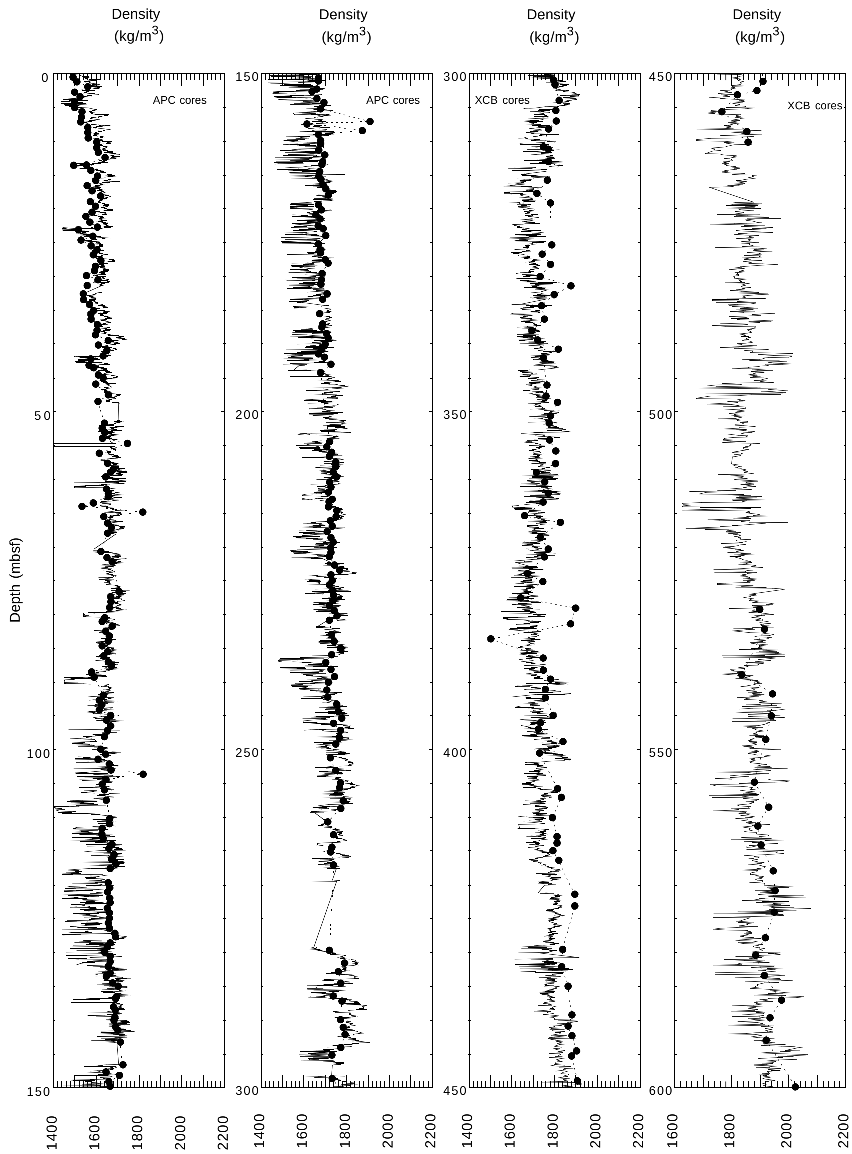

Figure 31. GRAPE wet bulk density data (solid lines) compared with discrete gravimetric wet bulk density values (solid circles) for Hole 1085A.

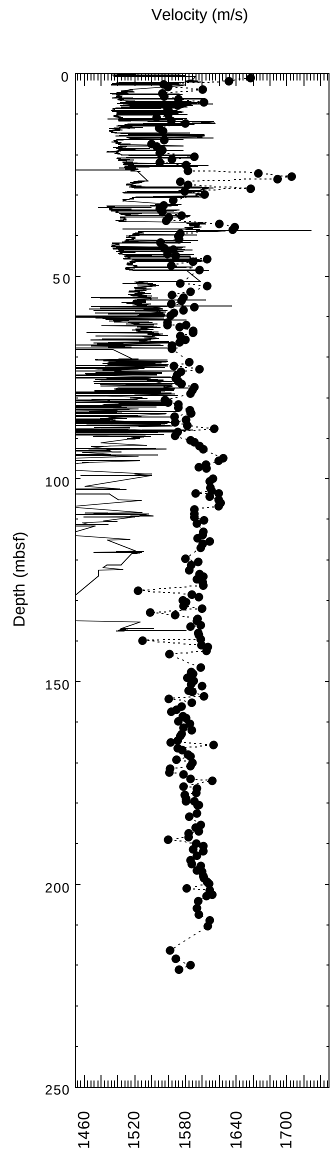

Figure 32. Discrete velocity profile (solid circles) compared with MST velocity data (solid line) measured at Hole 1085A.

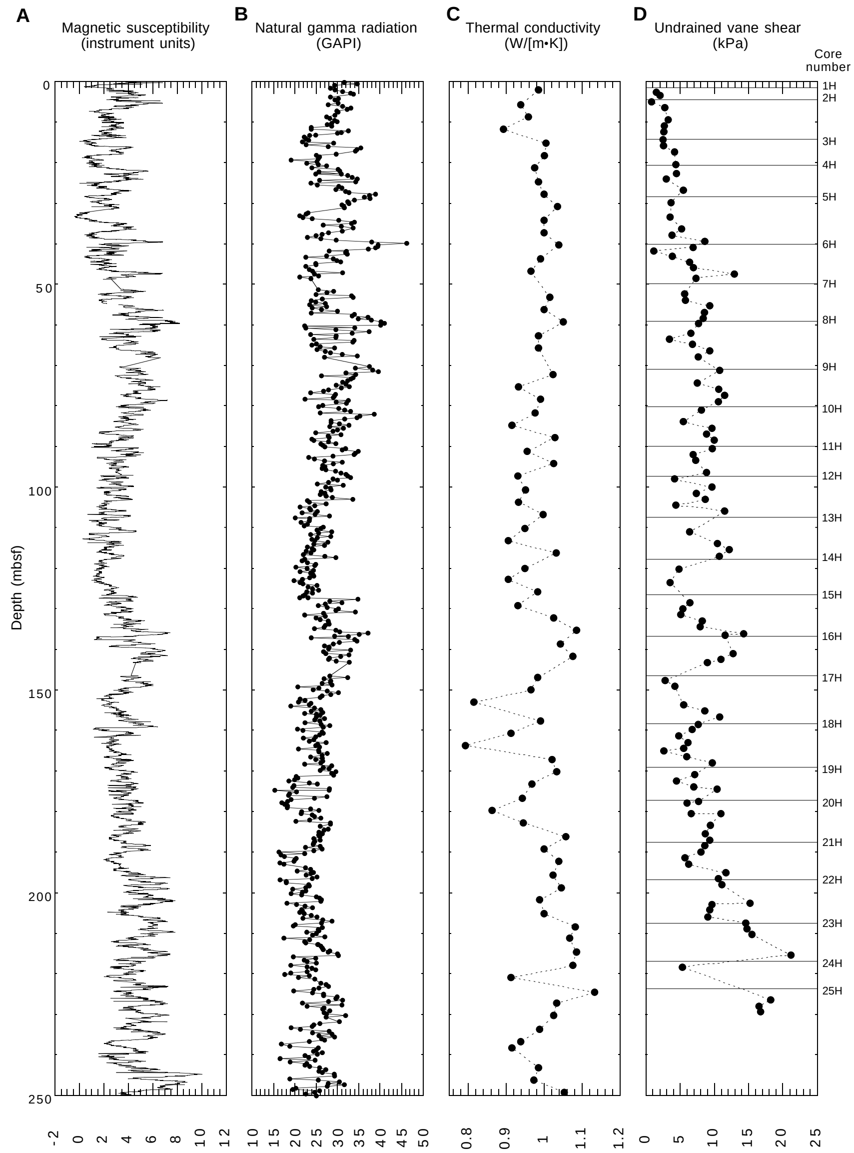

Figure 33. Plots of (**A**) magnetic susceptibility and (**B**) natural gamma radiation from MST measurements compared with discrete values of (**C**) thermal conductivity and (**D**) undrained vane shear strength between 0 and 250 mbsf for Hole 1085A.

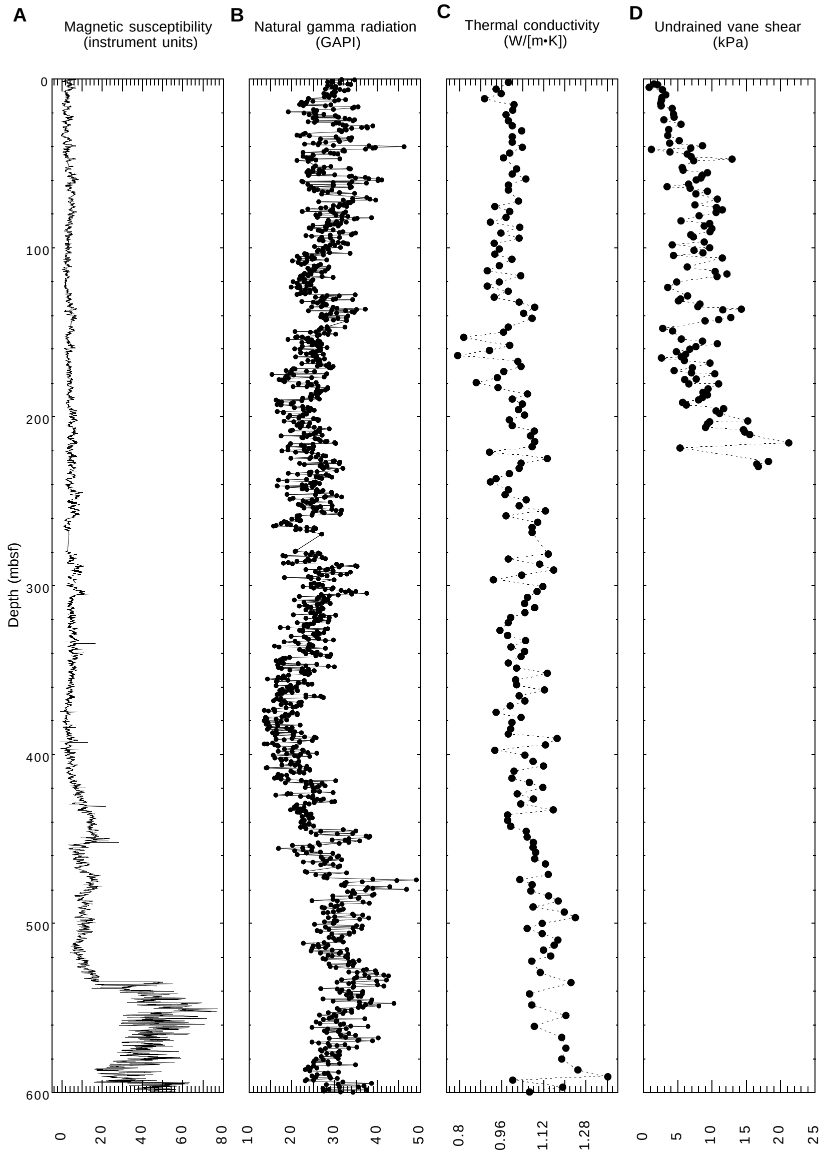

Figure 34. Plots of (**A**) magnetic susceptibility and (**B**) natural gamma radiation from MST measurements compared with discrete values of (**C**) thermal conductivity and (**D**) undrained vane shear strength between 0 and 600 mbsf for Hole 1085A.

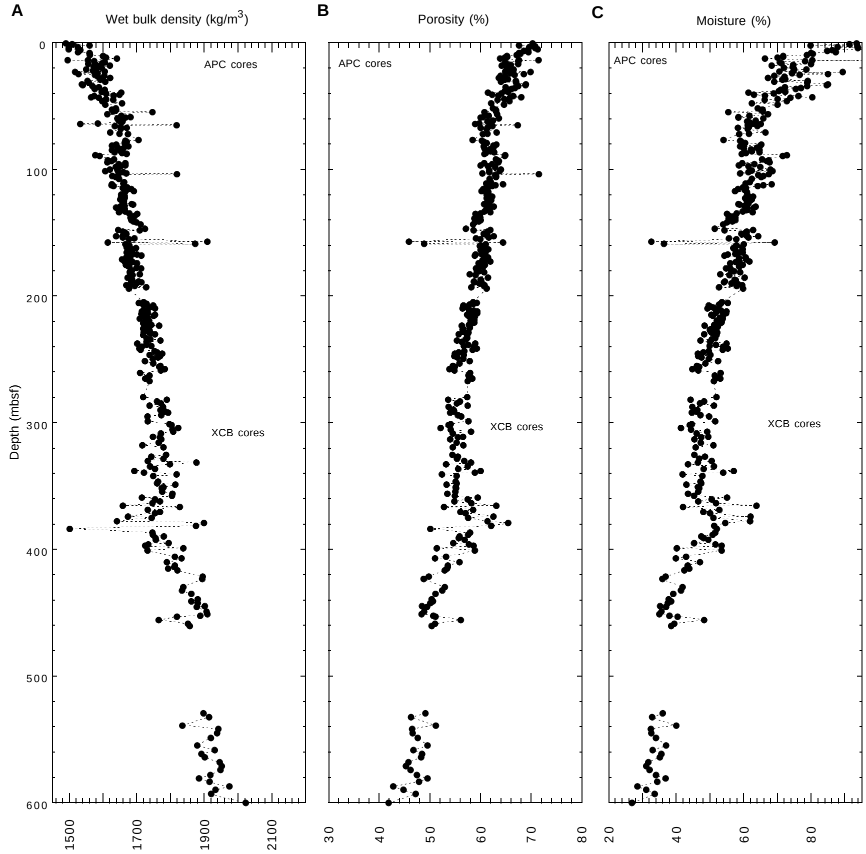

Figure 35. Gravimetric (**A**) wet bulk density, (**B**) porosity, and (**C**) moisture content derived from index properties measurements at Hole 1085A.

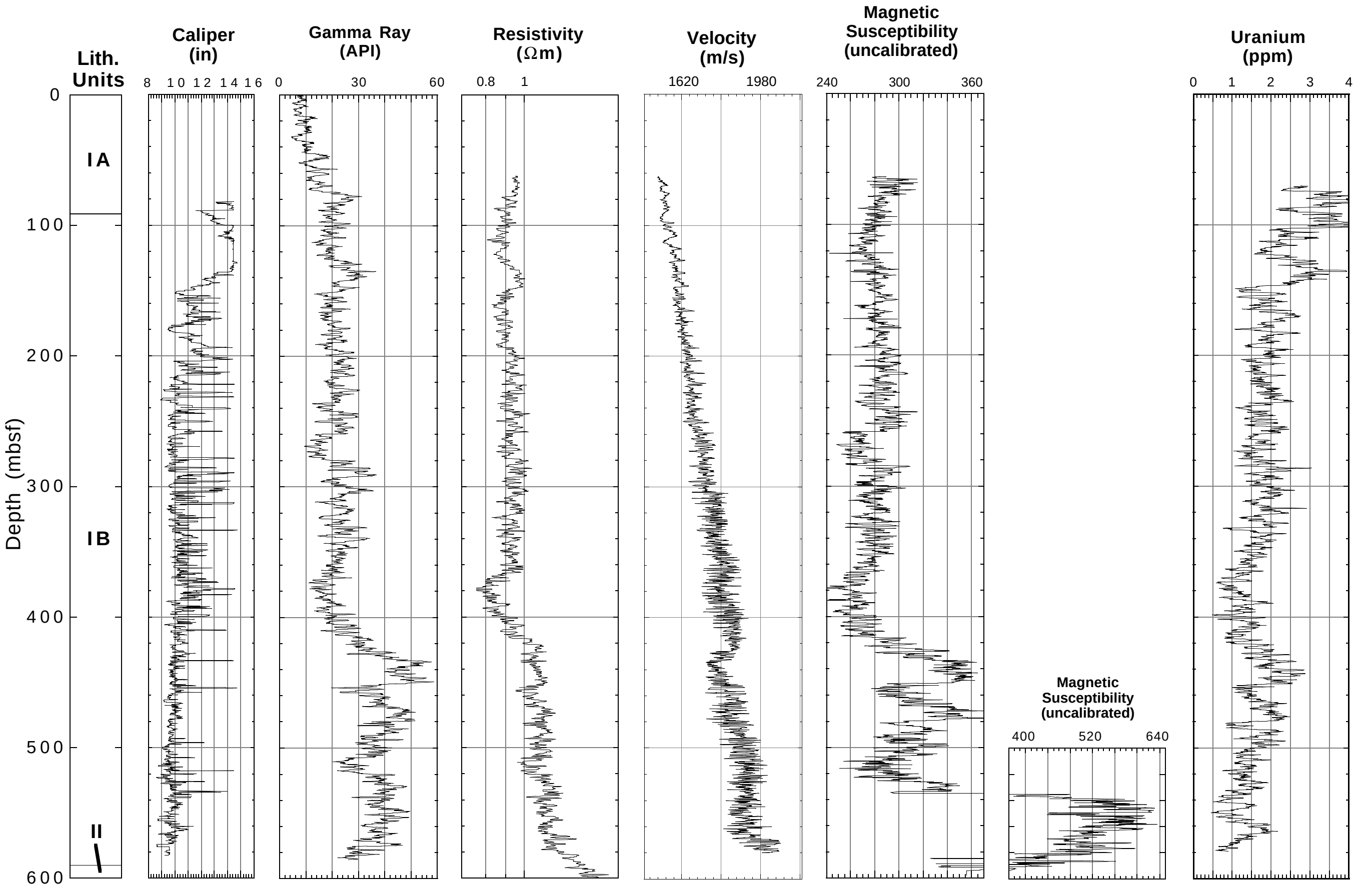

Figure 36. Downhole logs of caliper, natural gamma-ray, resistivity, velocity, magnetic susceptibility, and uranium content for Hole 1085A.

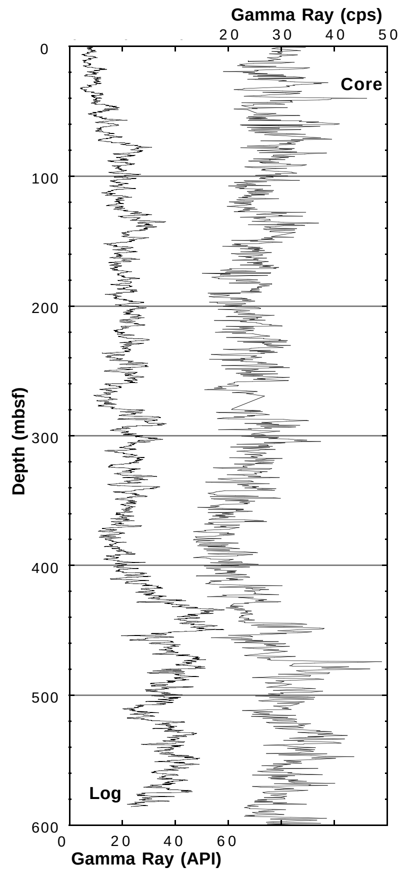

Figure 37. Comparison of core (MST) and log natural gamma-ray data for Hole 1085A.